Electronic Interactions of Iridium(III) Complexes in the Excited Triplet State with Molecular Oxygen

Naoya HASEBE

Gunma University

2016

Acknowledgements

I would like to express my sincere gratitude to **Professor Seiji Tobita** for his insightful direction, valuable suggestions and discussions throughout this study. I wish to thank **Associate Professor Minoru Yamaji** for his experimental guidance and comments. I also wish to thank **Assistant Professor Toshitada Yoshihara** for his valuable advice and discussions.

I greatly appreciate **Professor Takeshi Yamanobe**, **Professor Yosuke Nakamura**, **Professor Masashi Sonoyama**, and **Professor Motoko Asano** for their valuable comments and kind advice on this thesis.

I am grateful to **Associate Professor Hiroaki Horiuchi** for his valuable suggestions and experimental guidance especially for the quantum yield measurements of singlet oxygen formation, **Dr. Kengo Suzuki** of Hamamatsu Photonics K.K. for his valuable discussion and guidance especially for the phosphorescence quantum yield measurements of singlet oxygen, and **Associate Professor Yonekazu Deguchi** of Gunma National College of Technology for his valuable advice and experimental guidance especially for the electrochemical measurements. I would like to express my thanks to **Mr. Motohiko Hidaka** of Nissan Chemical Industries, Ltd. for his kind support in the spectroelectrochemical measurements.

I would like to thank **Dr. Atsushi Kobayashi** for his discussions, encouragements, and valuable assistance. I acknowledge **Mr. Tokio Takeshita** and all laboratory members for their valuable suggestion and assistance to complete this work.

Finally, I would like to express my deep gratitude to my family to respect my will and support me in every respect.

Naoya Hasebe

Contents

Chapter 1

General Introduction

1-1 Electronic States of Iridium(III) Complexes

Iridium(III) complexes have six-coordinated octahedral structure with a central Ir(III) ion which has electron configuration of [Xe]5d^6. Figure 1-1 shows the d-orbitals splitting in the octahedral ligand field. Because the energy gap (Δ) between the t_{2g} and e_g orbitals is significantly large in Ir(III) complexes, the t_{2g} orbitals are filled with 6 electrons, i.e. low spin state is favored (Figure 1-2) [1−3].

Electronic transitions of Ir(III) complexes involve not only ligand-localized $\pi-\pi^*$ transitions but also d−d and metal-to-ligand charge transfer (MLCT) transitions as shown in Figure 1-2. The d−d transition in the central Ir(III) ion is so-called Laporte forbidden, and thus the absorption probability is extremely small and even if there are lower-lying d−d excited states, they usually act as an energy-dissipating dark state [4]. In general, the lowest excited singlet and triplet states of Ir(III) complexes have electronic character which can be represented by mixed $\pi-\pi^*$ and MLCT states. The contribution of each state depends on the ligand. The importance of ^{3}MLCT (^{3}d−π^*) components in the T_1 state can be predicted by the magnitude of zero-field splitting (ZFS) [5]; significant ΔE(ZFS) values are representative of significant ^{3}MLCT components in the T_1 state.

Figure 1-3 shows the Jablonski diagram for generic luminophore. Because of the large spin-orbit coupling constant (ζ = 3,909 cm^{-1} [6]) of the central Ir(III) ion, intersystem crossing of Ir(III) complexes occurs very rapidly (< 100 fs [7,8]). As a result, the quantum yield of intersystem crossing (Φ_{isc}) becomes close to unity [9]. Hence, the emission of Ir(III) complexes arises almost exclusively from the excited triplet state with character of $^3\pi-\pi^*/^3$MLCT* mixed states; Ir(III) complexes exhibit strong phosphorescence even in room-temperature solutions if the solution is deaerated. Figure 1-4 shows the absorption and phosphorescence spectra of bis(2-(2′-benzothenyl)pyridinato-N,C^{3}′)iridium(III) acetylacetonate ($(btp)_2Ir(acac)$, abbreviated as BTP). The assignment of main absorption bands is indicated in Figure 1-4 [10]. The absorption band observed at around 486 nm has been attributed to the transition from the ground state to the first ^{1}MLCT state, while the emission spectrum which has the peak at around 615 nm is assigned to phosphorescence as being largely of ligand (btp)-centered triplet π-π* parentage with significant admixtures of the ^{3}MLCT character (dπ(Ir) →π*(btp)) [10].

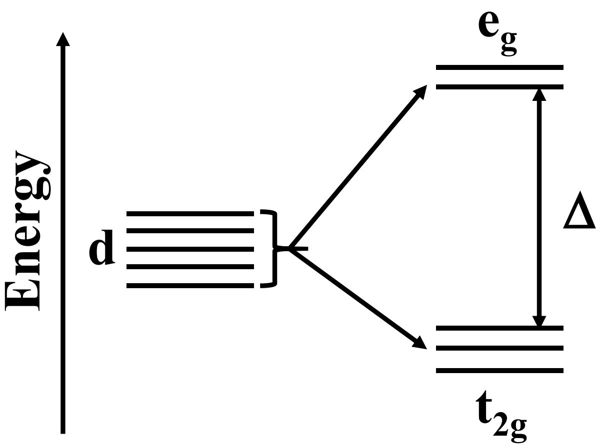

Figure 1-1. Splitting of d-orbital levels in the octahedral ligand field.

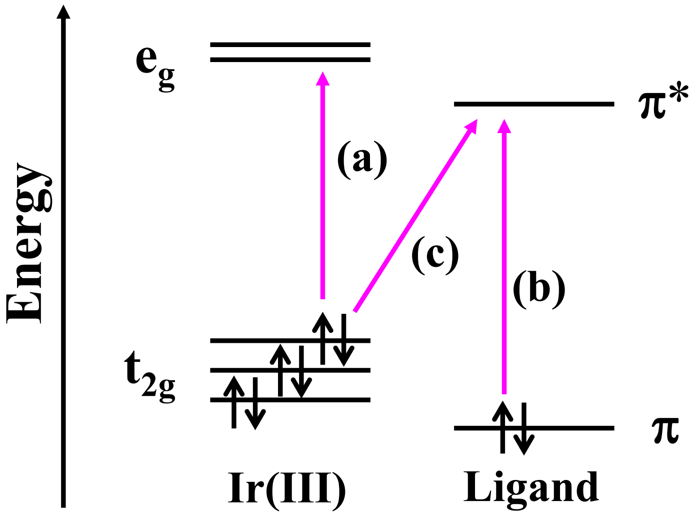

Figure 1-2. Electronic transitions of Ir(III) complexes. (a) d−d transition, (b) π−π* transition, and (c) metal-to-ligand charge transfer (MLCT) transition.

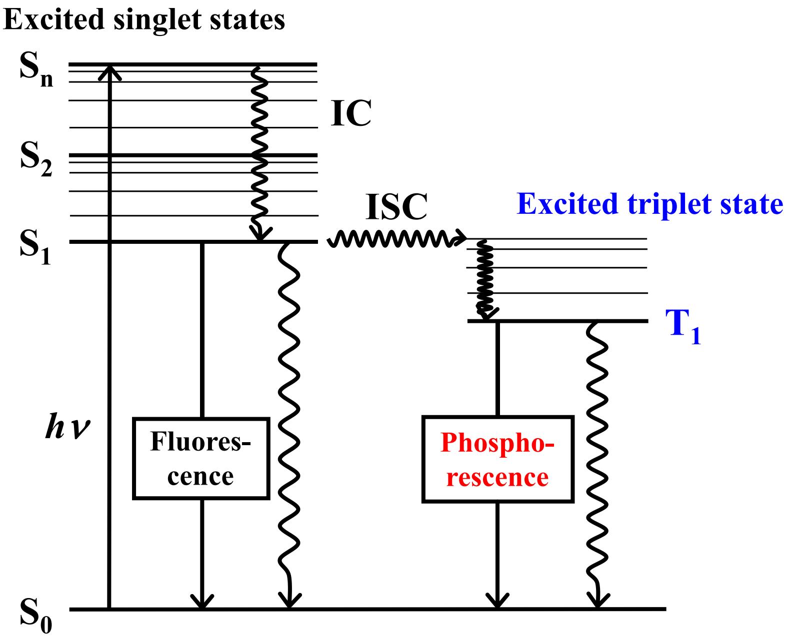

Figure 1-3. Jablonski diagram for generic luminophore. S_1, S_2, and S_n show the excited singlet states, and T_1 indicates the excited triplet state. IC and ISC denote the internal conversion and intersystem crossing, respectively.

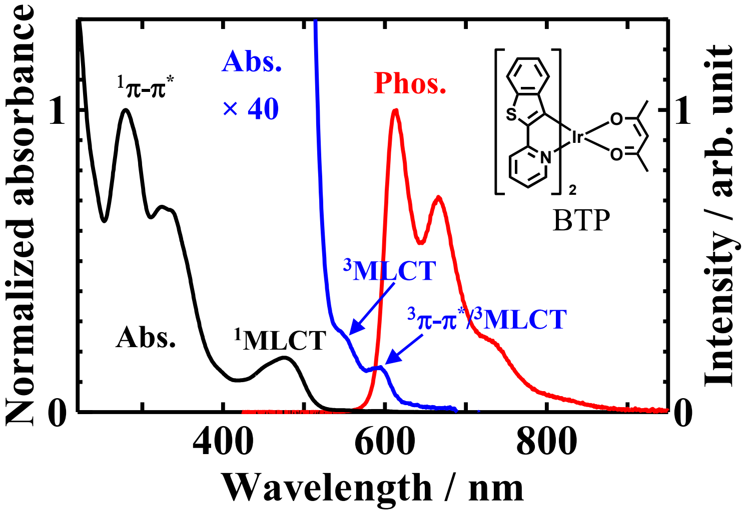

Figure 1-4. Absorption (black and blue lines) and emission (red line) spectra of BTP in CH_3CN at room temperature [10]. Absorption spectra are normalized at the peak wavelength.

1-2 Applications of Iridium(III) Complexes

1-2-1 Organic Light-Emitting Diodes (OLEDs)

Recently, Ir(III) complexes are put into practical use as a new emitting material in organic light-emitting diodes (OLEDs). In the OLED device, the excited singlet and triplet excitons are produced with the statistical ratio of 1:3 by charge recombination of holes and electrons (Figure 1-5). The external quantum efficiency (η_{ext}), i.e. the number of photons emitted from the OLED per charge carriers injected into the device, is given by the following equation:

$$\eta_{\mathrm{ext}} = \eta_{\mathrm{int}}\eta_{\mathrm{ph}} = \gamma\,\eta_{\mathrm{ex}}\phi_{\mathrm{PL}}\eta_{\mathrm{ph}} \qquad (1\text{-}1)$$

where η_{int} and η_{ph} are internal quantum efficiency and light out-coupling efficiency, respectively, γ is the electron-hole charge-balance factor, η_{ex} is the fraction of total excitons formed which result in radiative transition, and ϕ_{PL} is the intrinsic quantum efficiency for radiative decay. Because the excited singlet and triplet excitons are produced with the statistical ratio of 1:3 as described above, the maximum internal quantum efficiency (η_{int}) is 25%, as long as fluorescent materials are used. On the other hand, in the case of phosphorescent materials, intersystem crossing from the excited singlet state can be utilized, and thus nearly 100% internal quantum efficiency is theoretically possible.

In 1998, Baldo et al. have reported the first phosphorescent OLED (PHOLED) using 2,3,7,8,12,13,17,18-octaethyl-21*H*,23*H*-porphine platinum(II) (PtOEP) as an emitting material [11]. At the standard luminance (100 cd/m^2), this PHOLED exhibited the η_{ext} of

1.3%. Then, they improved the devices, and achieved the η_{ext} of 2.2 % at 100 cd/m^2 [12]. In 1999, they have reported a PHOLED using an iridium(III) complex, *fac* tris(2-phenylpyridine)iridium(III) (*fac*-Ir(ppy)$_3$) [13]. The device using *fac*-Ir(ppy)$_3$ gave the η_{ext} of 7.5% at 100 cd/m^2, suggesting that the η_{int} value of *fac*-Ir(ppy)$_3$ is larger than that of PtOEP. In 2001, nearly 100% η_{int} has been achieved by Adachi et al. using bis(2-phenylpyridine) iridium(III) acetylacetonate ((ppy)$_2$Ir(acac)) [14]. Since these pioneering works, a large number of Ir(III) complexes have been synthesized for OLED devices and some of them are already in practical use [15]. To improve the efficiency and durability of OLED devices using Ir(III) complexes, it is important to clarify the photophysical and photochemical properties of Ir(III) complexes. Especially, it is desired to clarify the interactions of Ir(III) complexes in the excited states with molecular oxygen, because the interactions with oxygen result in decrease in emission efficiency and degradation of material.

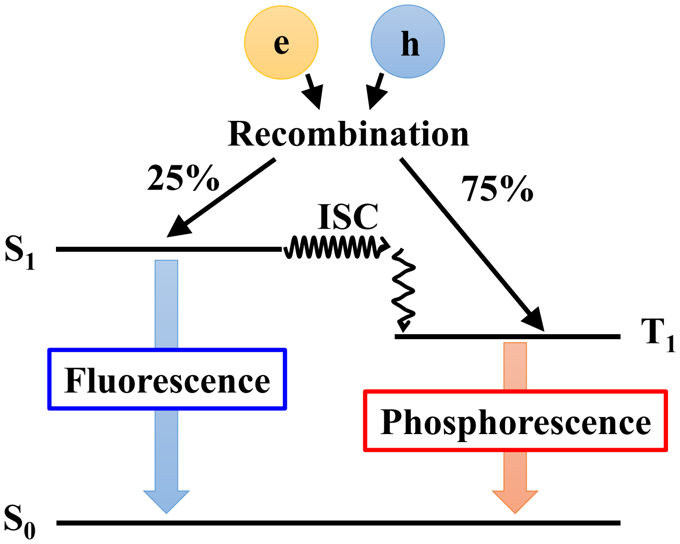

Figure 1-5. Excited singlet and triplet states generated by charge recombination.

1-2-2 Photoredox Catalyst

Organic syntheses utilizing radical reactions have been investigated for a long time. In these reactions, a toxic radical initiator with equivalent or close amount is generally used under UV irradiation, although there are problems in view of safety and energy. Recently, transition metal complexes which have a long lived excited state and absorption in the visible region have attracted much attention as a photoredox catalyst. Especially, Ru(II) and Ir(III) complexes are being revealed to have excellent characteristics as photoredox catalyst [16]. By irradiation of visible light to these complexes, an electron transfer reaction to substrate molecule is induced to produce highly reactive radical species which initiate subsequent reaction sequences. In Scheme 1-1, photoredox α-arylation of amines with 1,4-dicyanobenzene using Ir(ppy)$_3$ as a photoredox catalyst [16] is shown as an example of photoredox reactions using transition metal complexes. Here, Ir(ppy)$_3$ in the excited triplet state acts as a reducing agent to produce 1,4-dicyanobenzene anion radical and Ir(ppy)$_3$ cation radical. Then the resultant Ir(ppy)$_3$ cation radical acts as an oxidizing agent. The initial step of these photoredox reactions is electron transfer reaction from Ir(III) complex in the excited triplet state to substrate molecule. It is, therefore, expected that the yield of separated radical ions following photoinduced electron transfer is key to photoredox catalysis. To develop new photoredox catalysts using Ir(III) complexes, elucidation of the electron transfer reactivities of Ir(III) complexes in the excited triplet state is required.

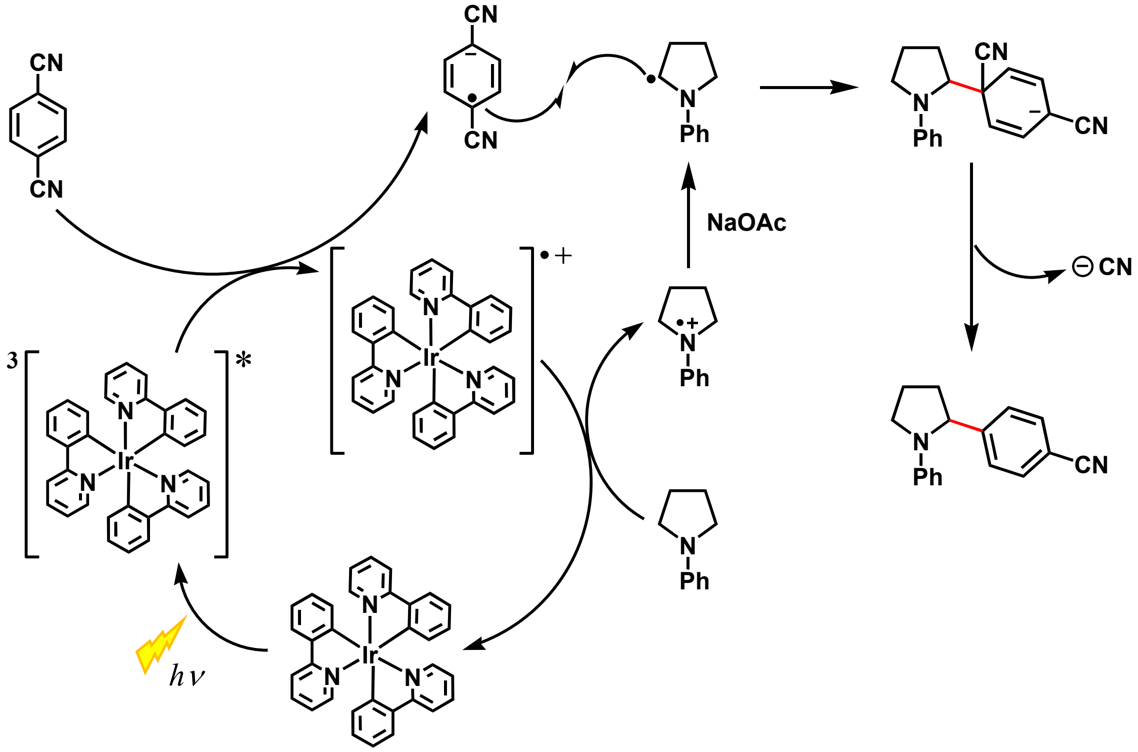

Scheme 1-1. Photoredox α-arylation of amines with 1,4-dicyanobenzene using Ir(ppy)$_3$ as a photoredox catalyst [16].

1-2-3 Biological Oxygen Probe

Iridium(III) complexes exhibit strong phosphorescence under deaerated condition at room temperature as described in Section 1-1. Phosphorescence is spin-forbidden transition, and the emission lifetime is very long (1−20 μs), which results in significant quenching by molecular oxygen. Figure 1-6 shows the Jablonski diagram for generic luminophor involving phosphorescence quenching by molecular oxygen. As shown in Figure 1-6, one can expect two possible quenching mechanisms leading to the formation of reactive oxygen species: singlet oxygen ($^1O_2$) and superoxide anion radical ($O_2^{\bullet-}$).

Recently, Ir(III) complexes have been successfully applied to the luminescence imaging of hypoxic tumor tissues and the quantification of intracellular oxygen concentration by utilizing phosphorescence quenching by molecular oxygen [17−22]. Phosphorescence lifetimes in the absence and presence of molecular oxygen (τ_p^0 and τ_p, respectively) are expressed as

$$\tau_p^0 = \frac{1}{k_p + k_{isc}'} \qquad (1\text{-}2)\text{ and}$$

$$\tau_p = \frac{1}{k_p + k_{isc}' + k_q[O_2]} \qquad (1\text{-}3),$$

where k_p and k_{isc}' are the phosphorescence rate constant and the rate constant of intersystem crossing from the T_1 state, k_q is the bimolecular quenching rate constant by O_2, and $[O_2]$ is the oxygen concentration. Stern−Volmer equation (eq 1-4) is derived from eqs 1-2 and 1-3,

$$\frac{\tau_{\mathrm{p}}^{0}}{\tau_{\mathrm{p}}} = 1 + k_{\mathrm{q}}\tau_{\mathrm{p}}^{0}\ [\mathrm{O}_2] = 1 + K_{\mathrm{SV}}[\mathrm{O}_2] \qquad (1\text{-}4),$$

where K_{SV} (= $k_{\mathrm{q}}\tau_{\mathrm{p}}^{0}$) is the Stern−Volmer constant that is related to the oxygen responsiveness. Eq 1-4 indicates that the phosphorescence lifetime depends on oxygen concentration, and thus $[\mathrm{O}_2]$ can be evaluated from τ_{p} if τ_{p}^{0} and k_{q} are determined in advance. The ideal biological oxygen probe is quenched exclusively by molecular oxygen, i.e. the emission intensity and lifetime are not affected by intrinsic substances other than O_2 in cells and tissues. This prompted the author to investigate the phosphorescence quenching of Ir(III) complexes by molecular oxygen and the possibility of photoinduced electron-transfer reactions with biological substances in living organisms.

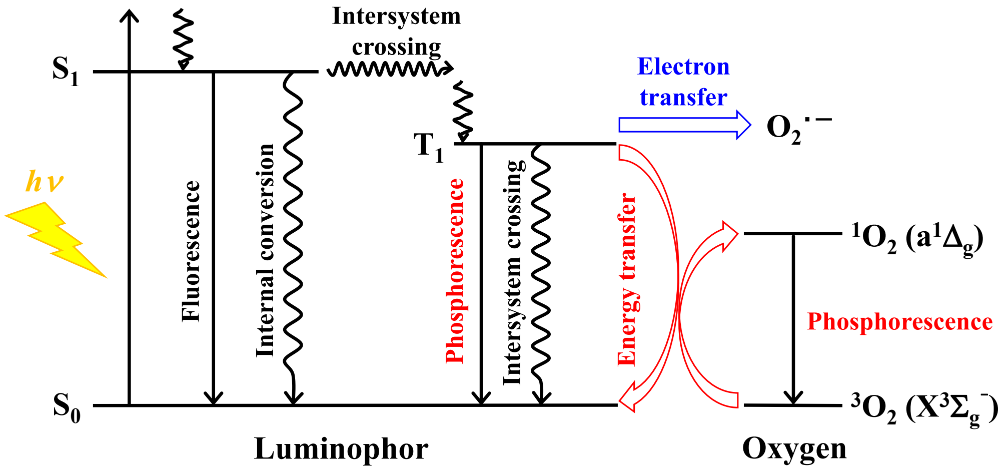

Figure 1-6. Jablonski diagram for generic luminophor involving phosphorescence quenching by molecular oxygen.

1-3 Characteristic of Singlet Oxygen

Figure 1-7a shows the potential energy curves of the ground state ($X^3\Sigma_g^-$) and excited states of molecular oxygen (O_2) [23]. The lowest excited state ($a^1\Delta_g$) of O_2 is singlet, and is generally called singlet oxygen. The molecular oxygen has another low-lying singlet excited state ($b^1\Sigma_g^+$) in addition to the $a^1\Delta_g$ state. Because the electronic ground state of the molecular oxygen is $X^3\Sigma_g^-$ state, direct excitation to the $a^1\Delta_g$ and $b^1\Sigma_g^+$ states is strictly forbidden from spin and symmetry selection rules. Therefore, singlet oxygen is usually produced by energy transfer from an excited triplet molecule (photosensitizer) to the molecular oxygen in the ground state (Figure 1-6). Figure 1-7b illustrates the energy levels of the $a^1\Delta_g$ and $b^1\Sigma_g^+$ states together with their spin configurations. Singlet oxygen exhibits phosphorescence at around 1270 nm arising from the $a^1\Delta_g \rightarrow X^3\Sigma_g^-$ transition. The quantum yield of the $a^1\Delta_g \rightarrow X^3\Sigma_g^-$ emission is known to depend strongly on the kind of solvent, because the rate of competing nonradiative processes is significantly altered by the nature of the solvent [24].

Singlet oxygen is well known as one of the reactive oxygen species, and has been considered as a major cytotoxic species to eukaryotic cells, bacteria and viruses. Extracellularly generated singlet oxygen has been found to be genotoxic to mammalian cells. Ultraviolet A (UV-A) exposure to skin is thought to cause skin aging and skin cancer mainly by singlet oxygen. Optical detection of intracellular and in vivo oxygen usually utilizes phosphorescence quenching of transition metal complexes, which results in production of biologically toxic singlet oxygen. It is, therefore, of essential importance to reveal the quantum efficiency and the fate of singlet oxygen produced by phosphorescence quenching of transition metal complexes.

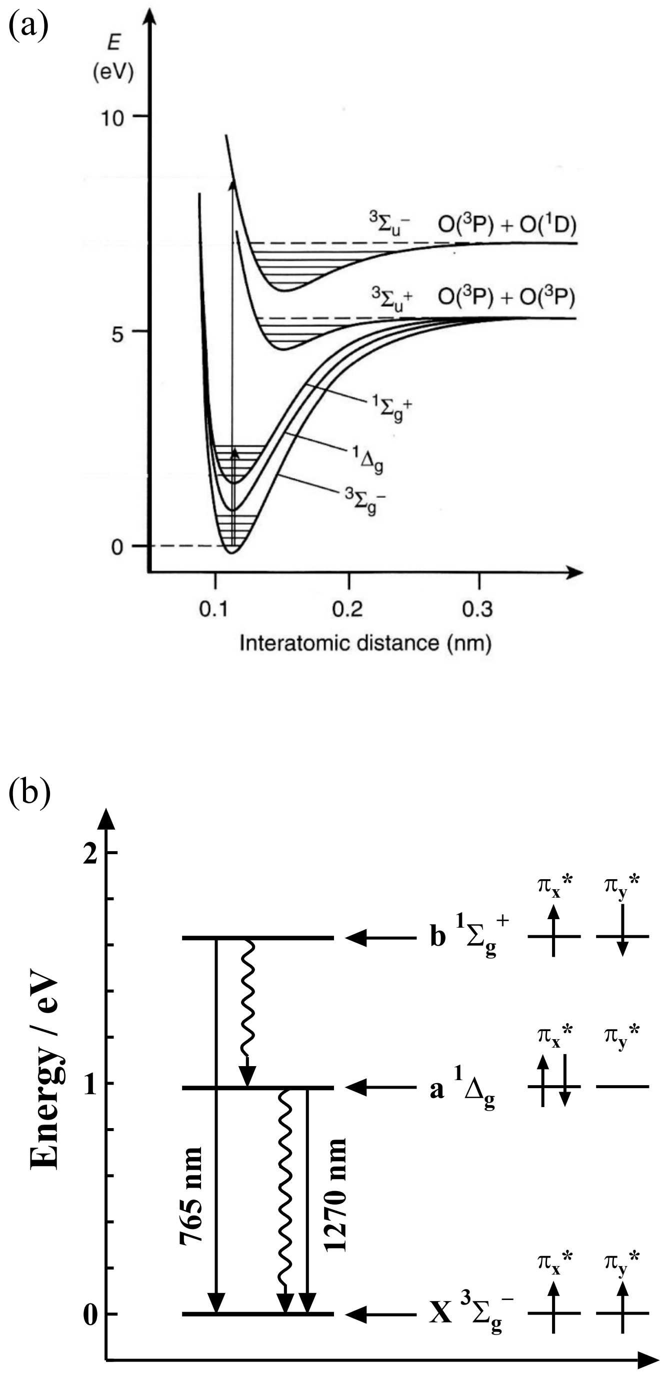

Figure 1-7. (a) Potential energy curves of the ground state ($X^3\Sigma_g^-$) and excited states of molecular oxygen (O_2) [23]. (b) Energy levels of the $a^1\Delta_g$, $b^1\Sigma_g^+$, and $X^3\Sigma_g^-$ states of O_2 together with their spin configurations.

1-4 Purpose of This Study

To rationally develop novel Ir(III) complexes which can be used for various applications such as biological oxygen probe, light-emitting material for OLEDs, and photoredox catalyst, it is of essential importance to clarify the phosphorescence quenching mechanisms by molecular oxygen and electron transfer reactivities of Ir(III) complexes in the excited states. In addition, it is desired to reveal the photophysical properties of singlet oxygen that is produced as a result of phosphorescence quenching of transition metal complexes.

In this study, the phosphorescence quenching of neutral and cationic Ir(III) complexes by aromatic electron acceptors (AEAs: 1,4-dinitrobenzene (DNB), nitrobenzene (NB), and 1,4-dicyanobenzene (DCB)) was investigated to elucidate photoinduced electron-transfer (PET) reactivities of Ir(III) complexes. Furthermore, with reference to the results of PET reactions, the phosphorescence quenching mechanisms of Ir(III) complexes by molecular oxygen were examined.

A new integrating sphere instrument that is applicable to the emission quantum yield measurements in the visible to near-infrared (NIR) region was developed. By using this instrument, the absolute phosphorescence quantum yield of singlet oxygen was determined in various solvents. In addition, the phosphorescence lifetimes of singlet oxygen in different solvents were measured to evaluate the radiative and nonradiative rate constants which are associated with the relaxation properties of singlet oxygen produced in living cells.

References

[1] Flamigni, L.; Barbieri, A.; Sabatini, C.; Ventura, B.; Barigelletti, F. *Top. Curr. Chem.* **2007**, *281*, 143−203.

[2] Divisia, B.; Ford, P. C.; Watts, R. J. *J. Am. Chem. Soc.* **1980**, *102*, 7264−7268.

[3] Mahboob, N.; Miyashita, Y.; Yamada, Y.; Fujisawa, K.; Okamoto, K. *Inorg. Chim. Acta* **2004**, *357*, 75−82.

[4] Takizawa, S.; Shimada, K.; Murata, S. *Inorg. Chem.* **2014**, *53*, 2983−2995.

[5] Yersin, H.; Rausch, A. F.; Czerwieniec, R.; Hofbeck, T.; Fischer, T. *Coord. Chem. Rev.* **2011**, *255*, 2622−2652.

[6] Montalti, M.; Credi, A.; Prodi, L.; Gandolfi, M. T. *Handbook of Photochemistry, 3rd Ed.*; CRC Press: Boca Raton, 2005.

[7] Tang, K.-C.; Liu, K. L.; Chen, I-C. *Chem. Phys. Lett.* **2004**, *386*, 437−441.

[8] Hedley, G. J.; Ruseckas, A.; Samuel, I. D.W. *Chem. Phys. Lett.* **2008**, *450*, 292−296.

[9] Endo, A.; Suzuki, K.; Yoshihara, T.; Tobita, S.; Yahiro, M.; Adachi, C. *Chem. Phys. Lett.* **2008**, *460*, 155−157.

[10] Finkenzeller, W. J.; Hofbeck, T.; Thompson, M. E.; Yersin, H. *Inrog. Chem.* **2007**, *46*, 5076−5083.

[11] Baldo, M. A.; O'Brien, D. F.; You, Y.; Shoustikov, A.; Sibley, S.; Thompson, M. E.; Forrest, S. R. *Nature*, **1998**, *395*, 151−154.

[12] O'Brien, D. F.; Baldo, M. A.; Thompson, M. E.; Forrest, S.R. *Appl. Phys. Lett.* **1999**, *74*, 442−444.

[13] Baldo, M. A.; Lamansky, S.; Burrows, P. E.; Thompson, M. E.; Forrest, S. R. *Appl. Phys. Lett.* **1999**, *75*, 4−6.

[14] Adachi, C.; Baldo, M. A.; Thompson, M. E.; Forrest, S. R. *J. Appl. Phys.* **2001**, *90*, 5048−5051.

[15] Yang, X.; Zhou, G.; Wong, W.-Y. *Chem. Soc. Rev.* **2015**, *44*, 8484−8575.

[16] Prier, C. K.; Rankic, D. A.; MacMillan, D. W. C. *Chem. Rev.* **2013**, *113*, 5322−5363.

[17] Zhang, S.; Hosaka, M.; Yoshihara, T.; Negishi, K.; Iida, Y.; Tobita, S.; Takeuchi, T. *Cancer Res*. **2010**, *70*, 4490−4498.

[18] Yoshihara, T.; Yamaguchi, Y.; Hosaka, M.; Takeuchi, T.; Tobita, S. *Angew. Chem. Int. Ed.* **2012**, *51*, 4148−4151.

[19] Murase, T.; Yoshihara, T.; Tobita, S. *Chem. Lett*. **2012**, *41*, 262−263.

[20] Yoshihara, T.; Hosaka, M.; Terata, M.; Ichikawa, K.; Murayama, S.; Tanaka, A.; Mori, M.; Itabashi, H.; Takeuchi, T.; Tobita, S. *Anal. Chem*. **2015**, *87*, 2710−2717.

[21] Yoshihara, T.; Murayama, S.; Masuda, T.; Kikuchi, T.; Yoshida, K.; Hosaka, M.; Tobita, S. *J. Photochem. Photobiol. A: Chem*. **2015**, *299*, 172−182.

[22] Hirakawa, Y.; Yoshihara, T.; Kamiya, M.; Mimura, I.; Fujikura, D.; Masuda, T.; Kikuchi, R.; Takahashi, I.; Urano, Y.; Tobita, S.; Nangaku, M. *Sci. Rep.* **2015**, *5*, 1−10.

[23] Balzani, V.; Ceroni, P.; Juris, A. *Photochemistry and Photophysics*; Wiley-VCH: Weinheim, 2014.

[24] Schweizer, C.; Schmidt, R. *Chem. Rev.* **2003**, *103*, 1685−1757.

Chapter 2

Phosphorescence Quenching of Neutral and Cationic Iridium(III) Complexes by Molecular Oxygen and Aromatic Electron Acceptors

2-1 Introduction

As described in Chapter 1, because iridium(III) complexes have excellent properties (high emission quantum yield [1], absorption of visible light, tunable emission color (blue to near-infrared) [2,3], and the high oxygen sensitivity), these complexes have received extensive attention as light-emitting material for organic light-emitting diodes (OLEDs) [4,5], photoredox catalyst [6−8], and biological oxygen probe [2,9−13]. Although the importance of Ir(III) complexes has increased in various fields, their photophysical and photochemical properties, including their electron-transfer reactivity and interactions with molecular oxygen, have not been fully clarified.

Electronic interactions between excited triplet molecules and molecular oxygen have been extensively investigated for various aromatic compounds, as exemplified by biphenyl, naphthalene, anthracene derivatives, and aromatic ketones [14−23]. By taking the spin-conservation rule into consideration, Gijzeman et al. [22] have proposed a quenching mechanism of the excited triplet molecules by O_2; Garner and Wilkinson [23] later extended this mechanism to charge-transfer complexes (Scheme 2-1). Because the spin multiplicity of O_2 in the ground state is the triplet state, singlet, triplet, and quintet encounter complexes $^{1,3,5}(T_1{}^3\Sigma)$ can be generated by diffusional collisions with rate constants of $(1/9)k_d$, $(3/9)k_d$, and $(5/9)k_d$, respectively, in accordance with the spin-conservation rule. Here, the quintet complex $^5(T_1{}^3\Sigma)$ has no direct product channel. The singlet complex $^1(T_1{}^3\Sigma)$ deactivates through internal conversion (IC) with rate constant $k_{ic}^{1\Sigma} + k_{ic}^{1\Delta}$ to produce singlet oxygen ($^1\Sigma_g{}^+$ or $^1\Delta_g$). The triplet pair $^3(T_1{}^3\Sigma)$ can also deactivate to the ground-state pair $^3(S_0{}^3\Sigma)$ via IC, although the rate constant $k_{ic}^{3\Sigma}$ is expected to be much smaller than $k_{ic}^{1\Sigma} + k_{ic}^{1\Delta}$ owing to the larger energy gap. Here, the compounds with a relatively-low oxidation potential and high triplet energy are known to exhibit increased triplet quenching because charge-transfer (CT) channels with the rate constants ${}^1k_{\mathrm{CT}}$ and ${}^3k_{\mathrm{CT}}$ participate in the deactivation processes. Notably, the relative importance of noncharge-transfer (nCT) and CT channels depends on the oxidation potential and triplet energy of the sensitizer in a given solvent. The involvement of intersystem crossing in the nCT and CT complexes has been hypothesized to affect the quenching rate and singlet-oxygen yield [14].

The phosphorescence quenching of the electronically excited state of Ir(III) complexes by molecular oxygen has been studied mainly paying attention to singlet-oxygen (${}^1O_2$) production, i.e., photosensitizers [24−30]. Takizawa et al. have reported that the quantum yields (Φ_Δ) of ${}^1O_2$ formation of cationic Ir(III) complexes [$Ir(ppy)_2(phen)^+$ and $Ir(ppy)_2(bpy)^+$, where ppy = 2-phenylpyridine, phen = 1,10-phenanthroline, bpy = 2,2′-bipyridyl] were very high (0.93 and 0.97 in CH_2Cl_2–MeOH (9:1)) [29], whereas neutral complexes with lower oxidation potentials gave smaller Φ_Δ values because of a contribution of CT interaction with O_2. For $(ppy)_2Ir(acac)$, *fac*-$Ir(ppy)_3$, and its derivatives, very high quenching rate constants (greater than 1.0×10^{10} $M^{-1}s^{-1}$) have been reported [28]. In addition, triplet quenching because of the electron transfer to O_2 has been suggested on the basis of their low oxidation potentials and high triplet energies. Velders and coworkers [31] have investigated the structure-oxygen quenching relationship using hemicaged (i.e., with a capping unit) and open (i.e., without a capping unit) ligand structures.

In this chapter, the phosphorescence quenching of neutral and cationic Ir(III) complexes (Figure 2-1), which have different oxidation potentials and different triplet energies, by molecular oxygen and aromatic electron acceptors (AEAs) was investigated. The relationship between the bimolecular quenching rate constant and the Gibbs energy change of electron-transfer reactions is revealed for both systems to clarify the electron-transfer reactivity of Ir(III) complexes with AEAs and the phosphorescence quenching mechanism of Ir(III) complexes in the excited triplet state by molecular oxygen. Elucidation of these processes is critically important for the development of novel Ir(III) complexes.

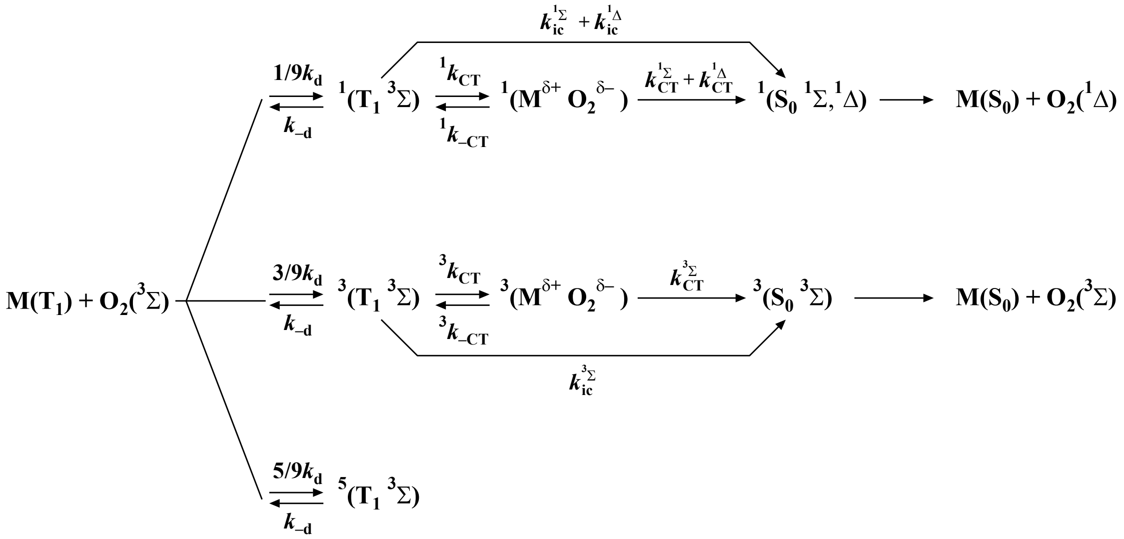

Scheme 2-1. Proposed mechanism for quenching of the excited triplet molecules by molecular oxygen.

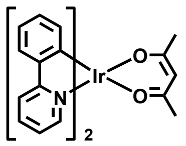

(ppy)$_2$Ir(acac)

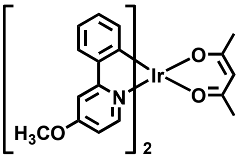

(ppy-4-OCH$_3$)$_2$Ir(acac)

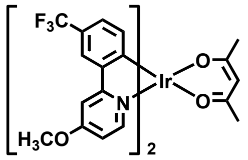

(ppy-5′-CF$_3$-4-OCH$_3$)$_2$Ir(acac)

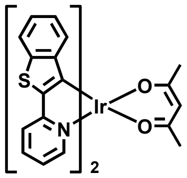

(btp)$_2$Ir(acac)

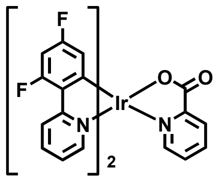

FIrpic

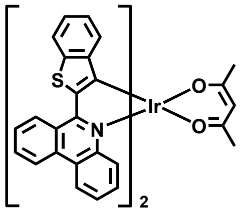

(btph)$_2$Ir(acac)

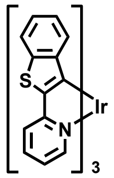

Ir(btp)$_3$

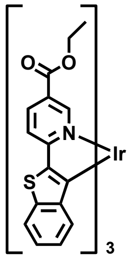

Ir(btp-5-COOEt)$_3$

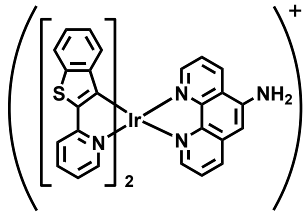

(btp)$_2$Ir(phen-NH$_2$)$^+$

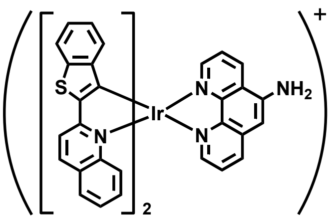

(btq)$_2$Ir(phen-NH$_2$)$^+$

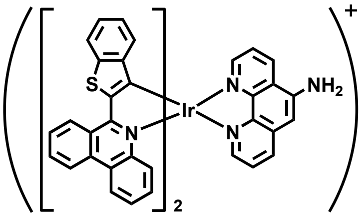

(btph)$_2$Ir(phen-NH$_2$)$^+$

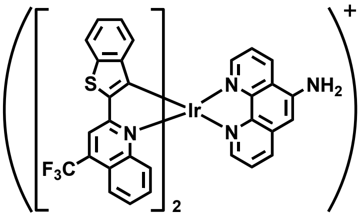

(btq-4-CF$_3$)$_2$Ir(phen-NH$_2$)$^+$

Figure 2-1. Chemical structures of neutral and cationic Ir(III) complexes used in this study.

2-2 Experimental Section

2-2-1 Materials

The Ir(III) complexes, $(btph)_2Ir(acac)$, $(btp)_2Ir(phen\text{-}NH_2)^+$, $(btq)_2Ir(phen\text{-}NH_2)^+$, and $(btph)_2Ir(phen\text{-}NH_2)^+$ were synthesized according to the literature [12,32] and characterized by means of NMR and Mass spectrometry. The other aromatic ligands and Ir(III) complexes were synthesized and characterized according to the methods described below. All reagents and solvents used in syntheses were purchased from Kanto Chemical, Wako Pure Chemical, Tokyo Chemical Industries, or Sigma-Aldrich, and were used as received from suppliers. ^1H-NMR spectra were measured with a JNM-AL300 (JEOL) at 300 MHz or a JNM-ECS400 (JEOL) at 400 MHz. Chemical shifts of ^1H-NMR were referenced to tetramethylsilane. The apparent resonance multiplicities s, d, t, q, and m indicate singlet, doublet, triplet, quartet, and multiplet, respectively. ESI-MS spectra were recorded using an API 2000 (Applied Biosystem). Elemental analysis was carried out on a MICRO CORDER JM10 (J-SCIENCE).

Synthetic procedure of aromatic ligands

ppy-4-OCH_3

A mixture of phenylboronic acid (467 mg, 3.83 mmol), 2-chloro-4-methoxypyridine (500 mg, 3.48 mmol), tetrakis(triphenylphosphine)palladium(0) (126 mg, 0.11 mmol), toluene (15 ml), ethanol (7 ml), and aqueous solution of sodium carbonate (2 mol dm^{-3}, 20 ml) was heated at reflux under nitrogen atmosphere for 6 h. After cooling, the reaction mixture was diluted with an additional 100 ml of water and was extracted with chloroform (100 ml × 3). The extracted organic layer was dried with anhydrous magnesium sulfate, and then the solvent was evaporated under vacuum. The crude product was purified by silica-gel column chromatography using chloroform : ethyl acetate (9:1 v/v) as eluent. Yield: 440 mg (68%). ^{1}H NMR (300 MHz, $CDCl_3$) δ : 8.527−8.494 (d, 1H), 7.970−7.929 (m, 2H), 7.466−7.461 (m, 1H), 7.447−7.405 (m, 2H), 7.233−7.225 (d, 1H), 6.789−6.762 (m, 1H), 3.909 (s, 3H).

ppy-5′-CF_3-4-OCH_3

A mixture of 3-trifluoromethylphenylboronic acid (727 mg, 3.83 mmol), 2-chloro-4-methoxypyridine (500 mg, 3.48 mmol), tetrakis(triphenylphosphine)palladium(0) (250 mg, 0.22 mmol), toluene (15 ml), ethanol (7 ml), and aqueous solution of sodium carbonate (2 mol dm^{-3}, 20 ml) was heated at reflux under nitrogen atmosphere for 6 h. After cooling, the reaction mixture was diluted with an additional 100 ml of water and was extracted with chloroform (100 ml × 3). The extracted organic layer was dried with anhydrous magnesium sulfate, and then the solvent was evaporated under vacuum. The crude product was purified by silica-gel column chromatography using chloroform : ethyl acetate (19:1 v/v) as eluent. Yield: 590 mg (67%). ^{1}H NMR (300 MHz, $CDCl_3$) δ : 8.552−8.532 (d, 1H), 8.232 (s, 1H), 8.147−8.122 (d, 1H), 7.680−7.678 (d, 1H), 7.654−7.606 (t, 1H), 7.256 (s, 1H), 6.844−6.816 (d, 1H), 3.933 (s, 3H).

btp-5-COOEt

btp-5-COOEt was synthesized according to the literature [33]. A mixture of 6-bromonicotinic acid (4.30 g, 21 mmol), benzo[*b*]thiophen-2-ylboronic acid (3.59 g, 20 mmol), tetrakis(triphenylphosphine)palladium(0) (1.06 g, 0.92 mmol), toluene (30 ml), ethanol (30 ml), and aqueous solution of sodium carbonate (2 mol dm^{-3}, 60 ml) was heated at reflux under nitrogen atmosphere for overnight. After cooling, the reaction mixture was acidified by adding 12 M HCl, and a white crystal was obtained by suction filtration. The white solid (3.0 g) was dissolved in ethanol (250 ml), and then concentrated sulfuric acid (5 ml) was added to the solution. The solution was refluxed at 5h. The reaction mixture was diluted with an additional 100 ml of water and was extracted with chloroform (300 ml × 3). The crude product was purified by silica-gel column chromatography using chloroform as eluent. Yield: 2.5 g (75%). ^{1}H NMR (400 MHz, $CDCl_3$) δ : 9.22−9.21 (q, 1H), 8.33−8.31 (dd, 1H), 7.94 (s, 1H), 7.90−7.81 (m, 3H), 7.40−7.35 (m, 2H), 4.45−4.40 (dd, 2H), 1.44−1.40 (t, 3H).

btq-4-CF_3

A mixture of benzo[*b*]thiophen-2-ylboronic acid (810 mg, 4.55 mmol), 2-chloro-4-trifluoromethylquinoline (1.0 g, 4.32 mmol), tetrakis(triphenylphosphine)palladium(0) (150 mg, 0.13 mmol), tetrahydrofuran (30 ml), and aqueous solution of sodium carbonate (2 mol dm^{-3}, 20 ml) was heated at reflux under nitrogen atmosphere for 5 h. After cooling, the reaction mixture was diluted with an additional 100 ml of water and was extracted with chloroform (100 ml × 3). The extracted organic layer was dried with anhydrous magnesium sulfate, and then the solvent was evaporated under vacuum. The crude product was purified by silica-gel column chromatography using chloroform as eluent. Yield: 765 mg (54%). ^{1}H NMR (300 MHz, $CDCl_3$) δ : 8.24 (d, 1H), 8.20 (s, 1H), 8.12−8.09 (d, 1H), 8.04 (s, 1H), 7.92−7.79 (m, 3H), 7.67−7.62 (t, 1H), 7.41−7.37 (m, 2H).

General synthetic procedure of bis-cyclometalated iridium(III) complex with an acetylacetonate ligand

Iridium(III) complexes with an acetylacetonate ligand were synthesized according to the literature [32].

(ppy)$_2$Ir(acac)

^{1}H NMR (400 MHz, CDCl$_3$) δ : 8.52−8.51 (d, 2H), 7.86−7.84 (d, 2H), 7.75−7.71 (t, 2H), 7.55−7.53 (d, 2H), 7.15−7.12 (t, 2H), 6.82−6.78 (t, 2H), 6.70−6.66 (t, 2H), 6.27−6.25 (d, 2H), 5.21 (s, 1H), 1.78 (s, 6H). ESI-MS calcd for $C_{27}H_{23}IrN_2O_2$ (M)$^+$, 600.14 ; found, 599.8.

(ppy-4-OCH$_3$)$_2$Ir(acac)

^{1}H NMR (400 MHz, CDCl$_3$) δ : 8.29−8.27 (d, 2H), 7.49−7.47 (d, 2H), 7.33−7.32 (d, 2H), 6.80−6.76 (t, 2H), 6.75−6.72 (m, 2H), 6.70−6.66 (t, 2H), 6.32−6.30 (d, 2H), 5.18 (s, 1H), 4.01 (s, 6H), 1.77 (s, 6H). ESI-MS calcd for $C_{29}H_{27}IrN_2O_4$ (M)$^+$, 660.16 ; found, 660.2.

(ppy-5′-CF$_3$-4-OCH$_3$)$_2$Ir(acac)

^{1}H NMR (400 MHz, CDCl$_3$) δ : 8.27−8.25 (d, 2H), 7.68 (s, 2H), 7.39−7.38 (d, 2H), 6.89 (d, 2H), 6.84−6.82 (m, 2H), 6.41−6.39 (d, 2H), 5.22 (s, 1H), 4.06 (s, 6H), 1.79 (s, 6H). ESI-MS calcd for $C_{31}H_{25}F_6IrN_2O_4$ (M)$^+$, 796.13 ; found, 795.5.

(btp)$_2$Ir(acac)

^{1}H NMR (400 MHz, CDCl$_3$) δ : 8.44−8.43 (d, 2H), 7.79−7.75 (t, 2H), 7.64−7.62 (d, 4H), 7.07−7.00 (m, 4H), 6.82−6.78 (t, 2H), 6.21−6.19 (d, 2H), 5.26 (s, 1H), 1.78 (s, 6H). ESI-MS calcd for $C_{31}H_{23}IrN_2O_2S_2$ $(M)^+$, 712.08; found, 711.7.

Synthetic procedure of FIrpic

Aromatic ligand (dfppy; 2-(2,4-difluorophenyl)pyridine, 2.2 mmol) and $IrCl_3 \cdot 3H_2O$ (1.0 mmol) were dissolved in 2-ethoxyethanol (30 ml) and distilled water (10 ml), and then the solution was heated at reflux for 15 hours. After cooling, the precipitate formed was filtered to give a chloro-bridged dimer and washed thoroughly with methanol and *n*-hexane. The chloro-bridged dimer (0.1 mmol) was dissolved in 2-methoxyethanol (25 ml), then picolinic acid (74 mg, 0.6 mmol) and triethylamine (1 ml) were added. The solution was refluxed for 3 hours and evaporated to dryness under reduced pressure. The crude product was purified by silica-gel column chromatography using chloroform as an eluent. ^{1}H NMR (400 MHz, CDCl$_3$) δ : 8.75 (m, 1H), 8.34 (m, 1H), 8.27 (d, 2H), 7.95 (t, 1H), 7.78 (m, 3H), 7.42 (m, 2H), 7.19 (t, 1H), 6.97 (t, 1H), 6.48 (t, 1H), 6.40 (t, 1H), 5.83 (d, 1H), 5.57 (d, 1H). ESI-MS calcd for $C_{28}H_{16}F_4IrN_3O_2$ $(M)^+$, 695.08; found, 695.5.

Synthetic procedure of Ir(btp)$_3$

A mixture of a chloro-bridged dimer of btp (260 mg, 0.20 mmol), btp (130 mg, 0.62 mmol), silver trifluoromethanesulfonate (110 mg, 0.42 mmol), and propanediol (10 ml) was heated at 180 °C under nitrogen atmosphere for 15 h. After cooling, the reaction mixture was diluted with an additional 100 ml of water and was extracted with chloroform

(100 ml × 3). The extracted organic layer was dried with anhydrous magnesium sulfate, and then the solvent was evaporated under vacuum. The crude product was purified by silica-gel column chromatography using chloroform as eluent. Yield: 30 mg (9%). ^{1}H NMR (400 MHz, $CDCl_3$) δ : 7.75−7.73 (d, 3H), 7.55−7.50 (m, 6H), 7.32−7.31 (d, 3H), 7.10−7.07 (t, 3H), 6.75−6.64 (m, 9H). ESI-MS calcd for $C_{39}H_{24}IrN_3S_3$ $(M)^+$, 823.08; found, 822.5.

Synthetic procedure of Ir(btp-5-COOEt)$_3$

Aromatic ligand (btp-5-COOEt, 2.42 g, 8.5 mmol) and $IrCl_3•3H_2O$ (1.57 g, 4.0 mmol) were dissolved in 2-ethoxyethanol (130 ml) and distilled water (40 ml), and then the solution was heated at 140°C and refluxed for overnight. A mixture of a chloro-bridged dimer of btp-5-COOEt (796 mg, 0.50 mmol), btp-5-COOEt (427.3 mg, 1.5 mmol), silver trifluoroacetate (354 mg, 1.60 mmol), and 2-ethoxyethanol (35 ml) was heated at 110°C under nitrogen atmosphere for 24 h. The crude product was purified by silica-gel column chromatography using chloroform as eluent and recycling preparative HPLC (JAI, LC-9225 NEXT). Yield: 560 mg (54%). ^{1}H NMR (400 MHz, DMSO-d_6) δ : 8.44 (s, 1H), 8.28 (d, 1H), 8.23 (d, 1H), 8.12 (t, 3H), 7.98 (m, 3H), 7.94 (d, 1H), 7.89 (d, 1H), 7.82 (d, 1H), 7.26 (m, 2H), 7.18 (m, 1H), 6.94 (t, 2H), 6.74 (t, 1H), 6.51 (d, 1H), 6.16 (m, 2H), 4.12−3.99 (m, 6H), 1.09 (t, 3H), 0.99 (t, 3H), 0.88 (t, 3H). ESI-MS calcd for $C_{48}H_{36}IrN_3O_6S_3$ $(M)^+$, 1039.14; found, 1038.5.

General synthetic procedure of cationic iridium(III) complexes with 5-amino-1,10-phenanthroline ligand

Iridium(III) complexes with an 5-amino-1,10-phenanthroline ligand were synthesized according to the literature [12].

(btq-4-CF$_3$)$_2$Ir(phen-NH$_2$)$^+$

^{1}H NMR (400 MHz, DMSO-d_6) δ : 8.88 (d, 1H), 8.60 (d, 1H), 8.46 (s, 2H), 8.25 (d, 1H), 8.12 (m, 3H), 8.03 (m, 1H), 7.95 (s, 1H), 7.78 (m, 3H), 7.36 (m, 2H), 7.26 (m, 2H), 7.17 (d, 1H), 7.06 (d, 1H), 6.93−6.85 (m, 2H), 6.82−6.76 (m, 4H), 6.42 (m, 2H). ESI-MS calcd for $C_{48}H_{27}F_6IrN_5S_2$ (M-PF$_6$)$^+$, 1044.12; found, 1043.5.

1,4-Dinitrobenzene (DNB, Tokyo Chemical Industries) and 1,4-dicyanobenzene (DCB, Tokyo Chemical Industries) were purified by vacuum sublimation; nitrobenzene (NB, Wako Pure Chemical) was purified by distillation under reduced-pressure. Benzophenone (BP, >99.0%, Tokyo Chemical Industries) was recrystallized from ethanol/water. Perinaphthenone (PN, 97%, Sigma-Aldrich), which was used as a standard singlet-oxygen sensitizer, was purified by column chromatography using chloroform/ethyl acetate (99:1, v/v) as an eluent. Acetonitrile (CH_3CN, spectrophotometric grade, >99.7%, Kanto Chemical) and dehydrated CH_3CN (>99.0%, Wako Pure Chemical) were used in spectral and electrochemical measurements, respectively. These solvents were used without further purification. 2-Methyltetrahydrofuran (2-MeTHF, >98.0%, Tokyo Chemical Industries) used for spectral measurements at 77 K was purified by distillation.

2-2-2 Absorption and Emission Spectra

Absorption spectra were measured by using a UV/vis spectrophotometer (JASCO, Ubest-V550). Emission spectra were recorded on a spectrofluorimeter (Hitachi, F-7000) or a photonic multichannel analyzer PMA-11 (Hamamatsu, C7473-46) equipped with a monochromatized Xe arc lamp. The obtained emission spectrum was corrected for spectral sensitivity.

2-2-3 Electrochemical Measurements

Cyclic voltammetry measurements were carried out on a HZ-5000 (Hokuto Denko). A glassy carbon electrode (geometric area 7.06 mm^2), a coiled platinum wire, and an Ag wire were used as the working, counter, and reference electrodes, respectively, and were purchased from BAS, Inc. A glassy carbon electrode was cleaned using alumina solution prior to the measurements. Tetrabutylammonium hexafluorophosphate ($TBAPF_6$, >98.0%, Tokyo Chemical Industries) without further purification was used as a supporting electrolyte. The concentrations of the $TBAPF_6$ and the samples were adjusted to be 0.1 M and ca.1 mM, respectively. The sample solution was bubbled using Ar gas for ca. 20 min prior to the measurement. The obtained redox potentials were analyzed with analysis software (Hokuto Denko, HZ5000-ANA), and were corrected using a ferrocene/ferrocenium (>98.0, Wako Pure Chemical) standard solution.

Spectroelectrochemical measurements were performed with a spectrometer (Ocean Optics, USB4000). A tungsten-halogen light source (Ocean Optics, LS-1) was used as a monitoring light. Figure 2-2 shows the schematic diagram of the optical cell used in this measurement. The optical cell consisted of two indium tin oxide (ITO) sheets and an Ag wire which were used as working, counter, and reference electrodes, respectively. The optical path length of the optical cell was adjusted to be 1-mm using two Teflon sheets. The concentrations of Ir(III) complexes and DCB were adjusted to be 1 and 5 mM, respectively.

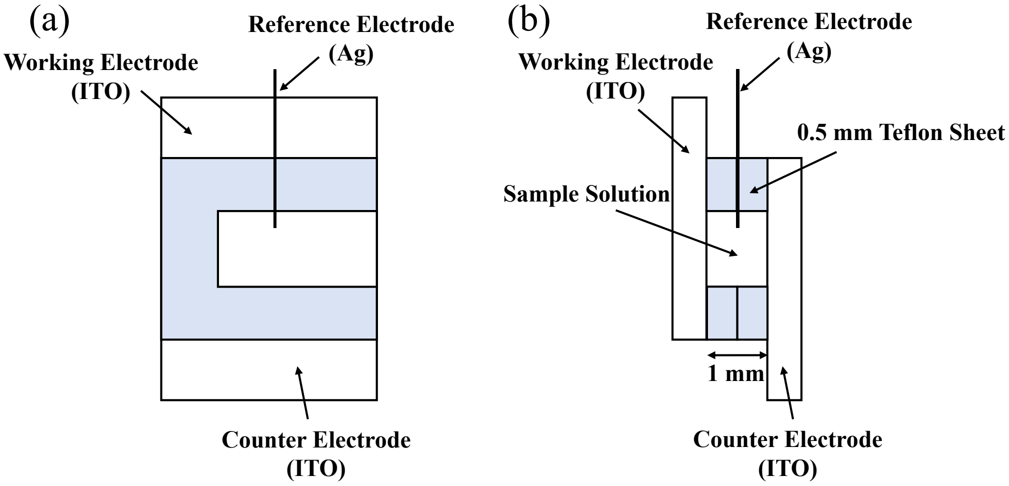

Figure 2-2. The optical cell used for spectroelectrochemical measurements. (a) front view and (b) side view.

2-2-4 Emission Lifetime

Emission lifetime measurements of Ir(III) complexes in the absence (τ_p^0) and presence (τ_p) of aromatic electron acceptors and molecular oxygen in solutions were carried out using a time-correlated single-photon counting fluorimeter (Edinburgh Analytical Instruments, FL900CDT or Hamamatsu, Quantaurus-Tau C11367, see Figure 2-3). A hydrogen-filled nanosecond flash lamp (pulse width 1.0 ns, frequency: 40 kHz), a light-emitting diode (365 nm, instrumental response function (IRF): ca. 1.0 ns (FWHM), frequency: 10 kHz to 1 MHz), or a laser diode (405 nm, pulse width: ca. 60 ns, IRF: 0.71 ns (FWHM), frequency: 10 kHz to 1 MHz) was used as the excitation light source for the FL900CDT and C11367. The excitation light pulse and the emission from the sample solution as start and stop pulses, respectively, were detected on a photomultiplier tube (Hamamatsu, R955 for FL900CDT and R928 for C11367, respectively). In the phosphorescence quenching experiments, deconvolution analyses were carried out when the lifetimes were less than 50 ns.

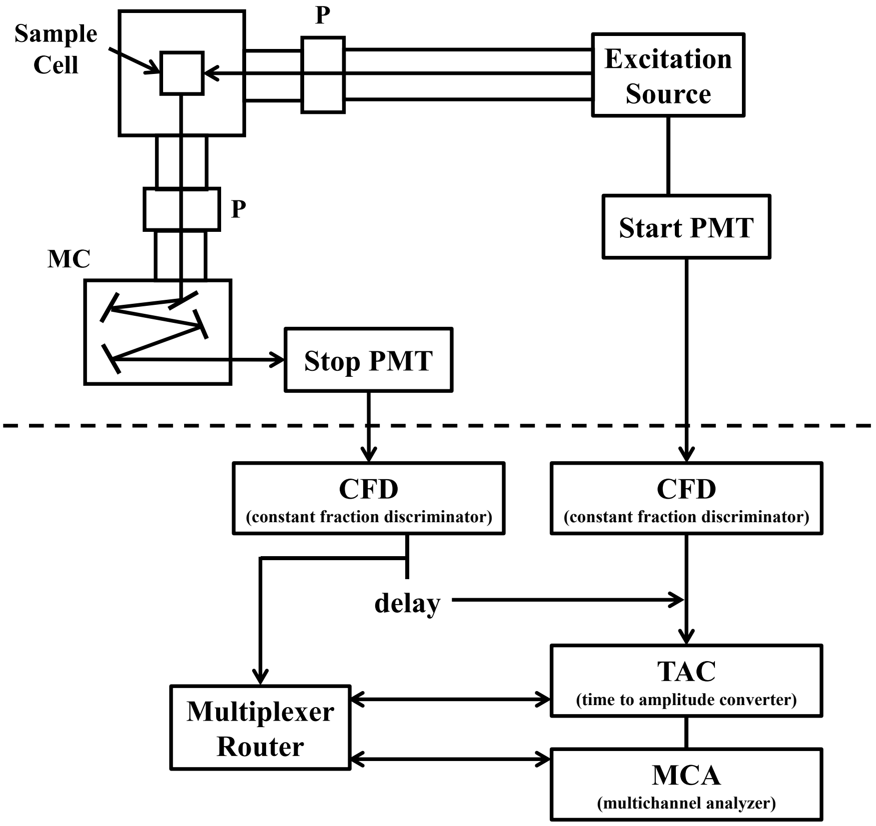

Figure 2-3. Schematic of time-correlated single photon counting instrument used for phosphorescence lifetime measurements. MC: monochromator, P: polarizer, PMT: photomultiplier tube.

2-2-5 Transient Absorption Measurements

Transient absorption measurements were carried out using a nanosecond laser photolysis system. The block diagram of this system is shown in Figure 2-4. The third harmonic of a Nd^{3+}:YAG laser (355 nm, Spectra Physics, GCR-130, pulse width 5 ns) and a 150-W Xe flash lamp (Ushio, UXL151D) were used as an excitation light source and a monitoring light, respectively. The timings between excitation and monitoring lights were controlled using a digital pulse generator (Stanford Research Systems, model DG535). After dispersed using a monochromator (Ritu, MC-20N), the transient signals were recorded on a digitizing oscilloscope (Tektronix, TDS-744, bandwidth 500 MHz, sample rate 2GS/s) and were fed into a personal computer (NEC, PC9801RA21). Because the sample solution was excited from the perpendicular direction to the monitoring light, the optical density of sample solutions was adjusted to be ca. 2.0 at 355 nm.

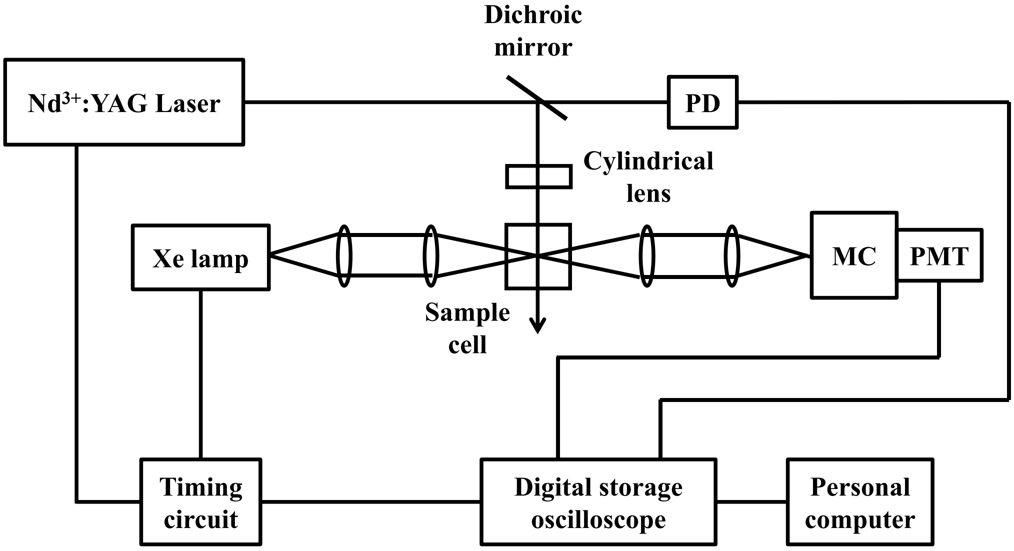

Figure 2-4. Nanosecond laser photolysis system. PD: Photodiode, MC: monochromator, and PMT: Photomultiplier tube.

2-2-6 Control of Oxygen Concentration

The oxygen/nitrogen mixed gas was used for the oxygen quenching experiments in CH_3CN. The oxygen partial pressure (pO_2) in the mixed gas was controlled using a mass-flow meter consisting of a controller (HORIBA STEC, SEC-V110DM) and a control unit (HORIBA STEC, PAC-D2). Prior to each measurement, the sample solutions were bubbled with the mixed gas for ca. 40 min.

2-2-7 Quantum Yield Measurements of Singlet Oxygen Formation and Emission Lifetime of Singlet Oxygen

In the quantum yield measurements of singlet-oxygen formation (Φ_Δ), the third harmonic of a Nd^{3+}:YAG laser (355 nm, Tokyo Instruments, LOTIS TII, pulse width 8 ns, 10 Hz) was used as an excitation light source [34]. The emission of singlet oxygen at 1270 nm was detected with an NIR photomultiplier tube (Hamamatsu, R5509-42) cooled at −80°C. After dispersed using a monochromator (Ritu, MC-10N), the signals from the photomultiplier tube were recorded on a digitizing oscilloscope (Tektronix, TDS380P, 400 MHz, 2GS/s). The block diagram of this instrument is shown in Figure 2-5. The $a^1\Delta_g \rightarrow X^3\Sigma_g^-$ emission intensity (I_Δ(Ir)) of singlet oxygen sensitized by Ir(III) complexes was extrapolated to the laser pulse peak and compared to that (I_Δ(PN)) sensitized by perinaphthenone (PN) in air-saturated CH_3CN as a reference sensitizer. Here, the Φ_Δ(PN) value in CH_3CN has been reported to be 0.98 [35]. The Φ_Δ(Ir) value of each Ir(III) complex was determined according to the following equation

$$\Phi_\Delta = \Phi_\Delta(\mathrm{PN}) \times \frac{I_\Delta(\mathrm{Ir})}{I_\Delta(\mathrm{PN})} \frac{A(\mathrm{PN})}{A(\mathrm{Ir})} \qquad (2\text{-}1),$$

where A(Ir) and A(PN) are the absorbance of the Ir(III) complex and PN solutions at 355 nm, respectively.

In the measurements of emission spectra of singlet oxygen ($a^1\Delta_g$), the signals from NIR photomultiplier tube were amplified by five times using a DC-300 MHz amplifier (Stanford Research Systems, SR445) and processed with a gated photon counter (Stanford Research Systems, SR400). The signals were averaged over three hundred laser shots to improve the signal-to-noise ratio and fed to a personal computer. The gate width and delay time of the gated photon counter were set at 10 μs and 1 or 5 μs, respectively.

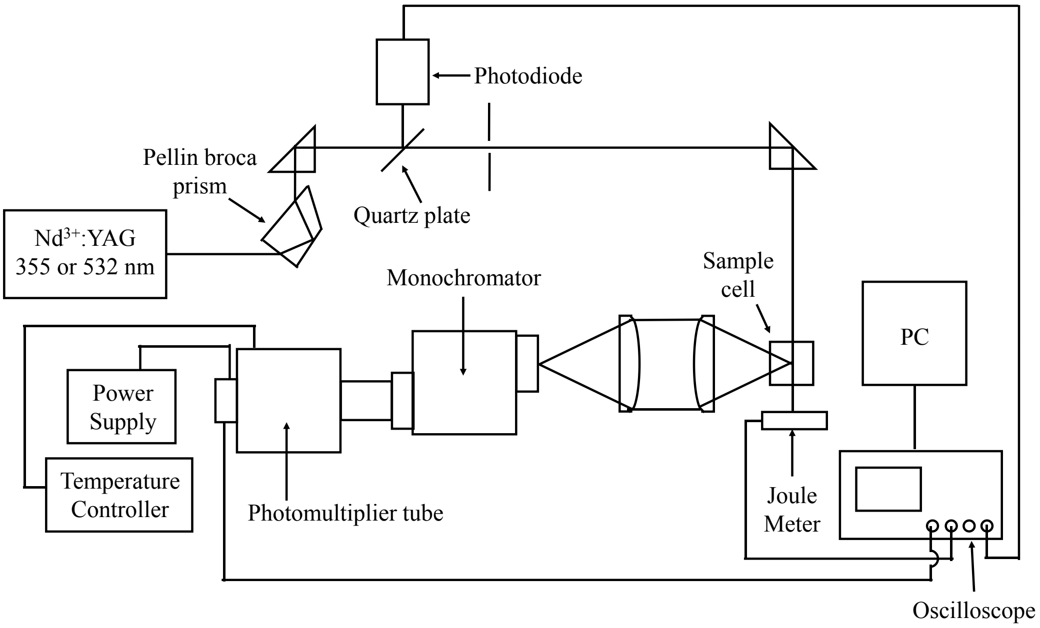

Figure 2-5. The block diagram of experimental setup for time-resolved emission measurements of $O_2(a^1\Delta_g)$.

2-3 Results and Discussion

2-3-1 Spectral and Electrochemical Properties

Prior to discussing the electron-transfer reactivities and the phosphorescence quenching mechanisms by molecular oxygen, the excited triplet energies (E_T) and the oxidation potentials (E_{ox}) of the Ir(III) complexes used in this study were measured. Figure 2-6 shows the absorption and emission spectra of all the complexes in nitrogen-saturated CH_3CN at room temperature and in 2-MeTHF at 77K. As described below (Section 2-3-3), all the complexes exhibited emission lifetimes longer than 1.0 μs under nitrogen-saturated condition, demonstrating that the emission can be attributed to the phosphorescence from the lowest excited triplet (T_1) state. The phosphorescent state of $(ppy)_2Ir(acac)$ has been assigned to the triplet metal-to-ligand charge-transfer (^{3}MLCT) state, whereas the emission of $(btp)_2Ir(acac)$ has been attributed to $^3\pi–\pi^*/^3$MLCT mixed state as described in Chapter 1 [36]. As shown in Figure 2-6, with the extension of the π-conjugated systems of the ligands (ppy < btp < btq < btph), the phosphorescence peak shifts substantially to the red, indicating stabilization of the excited triplet state. The triplet energies of these complexes were estimated from the first emission peak in the phosphorescence spectra measured in 2-MeTHF at 77K. The obtained E_T values ranged from 1.76 to 2.69 eV (Table 2-1).

In order to calculate the Gibbs energy change (ΔG_{el}) of electron-transfer reaction (see Section 2-3-2), the cyclic voltammograms of these complexes and aromatic electron acceptors (AEAs; DNB, NB, and DCB) were measured. As can be seen from Figure 2-7, the cyclic voltammograms of all the complexes in Ar-saturated CH_3CN solution showed reversible oxidation waves in the range from 0 to 1.2 V vs $Ag/AgNO_3$. The half-wave oxidation potentials ($E_{\mathrm{red}}^{1/2}$) were obtained from Figure 2-7 and are summarized in Table 2-1; the $E_{\mathrm{red}}^{1/2}$ values vary from 0.76 to 1.30 V vs SCE. As expected on the basis of the structures, cationic complexes and FIrpic, which possesses ligands with strong electron-withdrawing fluorine atoms, give higher oxidation potentials. These results indicate that the HOMO levels of cationic complexes and FIrpic were decreased. Figure 2-8 shows the cyclic voltammograms of AEAs. The reversible reduction waves were obtained, and the half-wave reduction potentials ($E_{\mathrm{red}}^{1/2}$) of DNB, NB, and DCB were determined to be −0.68, −1.14 and −1.61 V vs SCE, respectively.

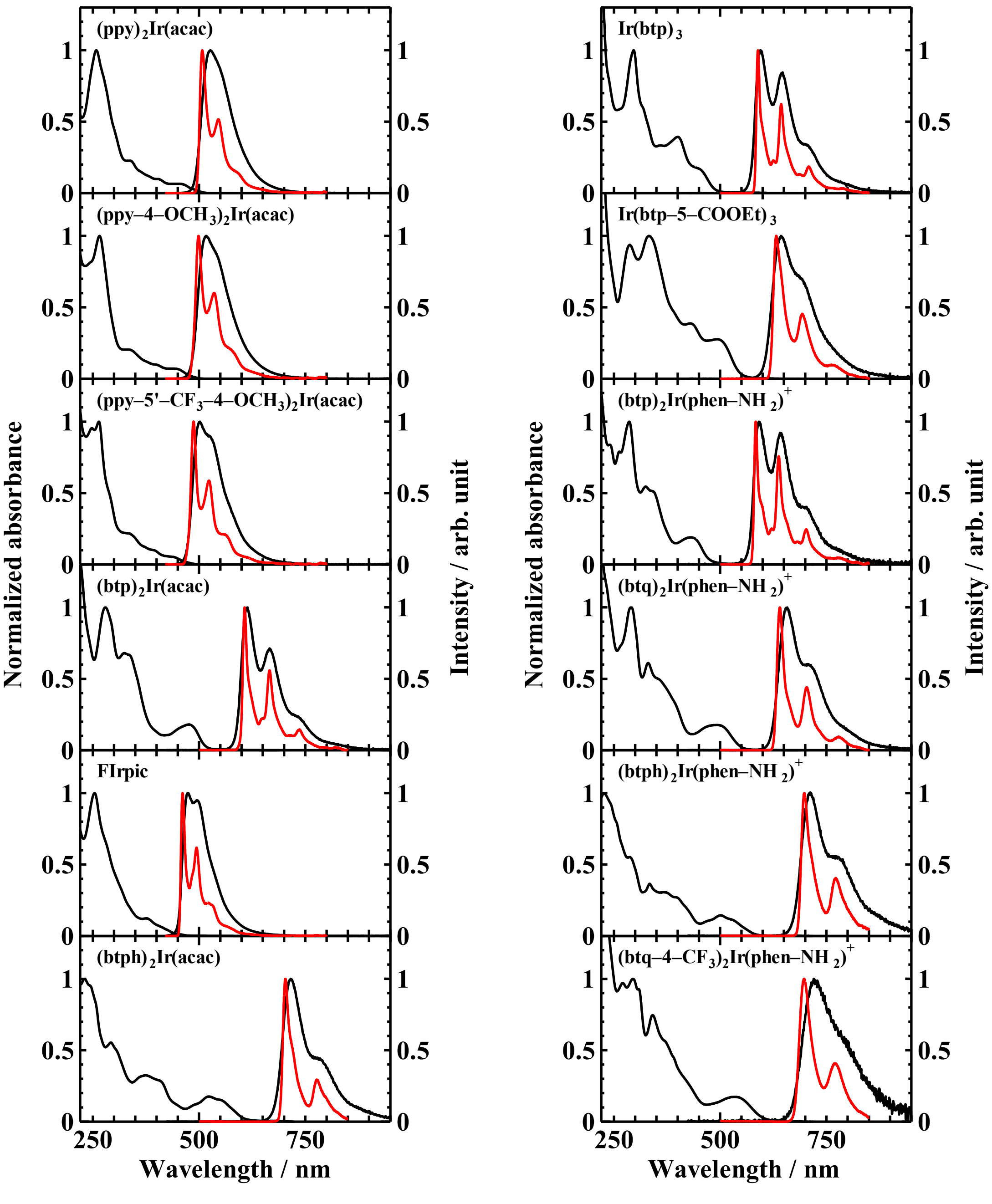

Figure 2-6. Absorption and phosphorescence spectra of Ir(III) complexes used in this study in nitrogen-saturated CH_3CN at room-temperature (black line) and in 2-MeTHF at 77 K (red line) (λ_{exc} = 405 nm). Absorption spectra are normalized at the peak wavelength.

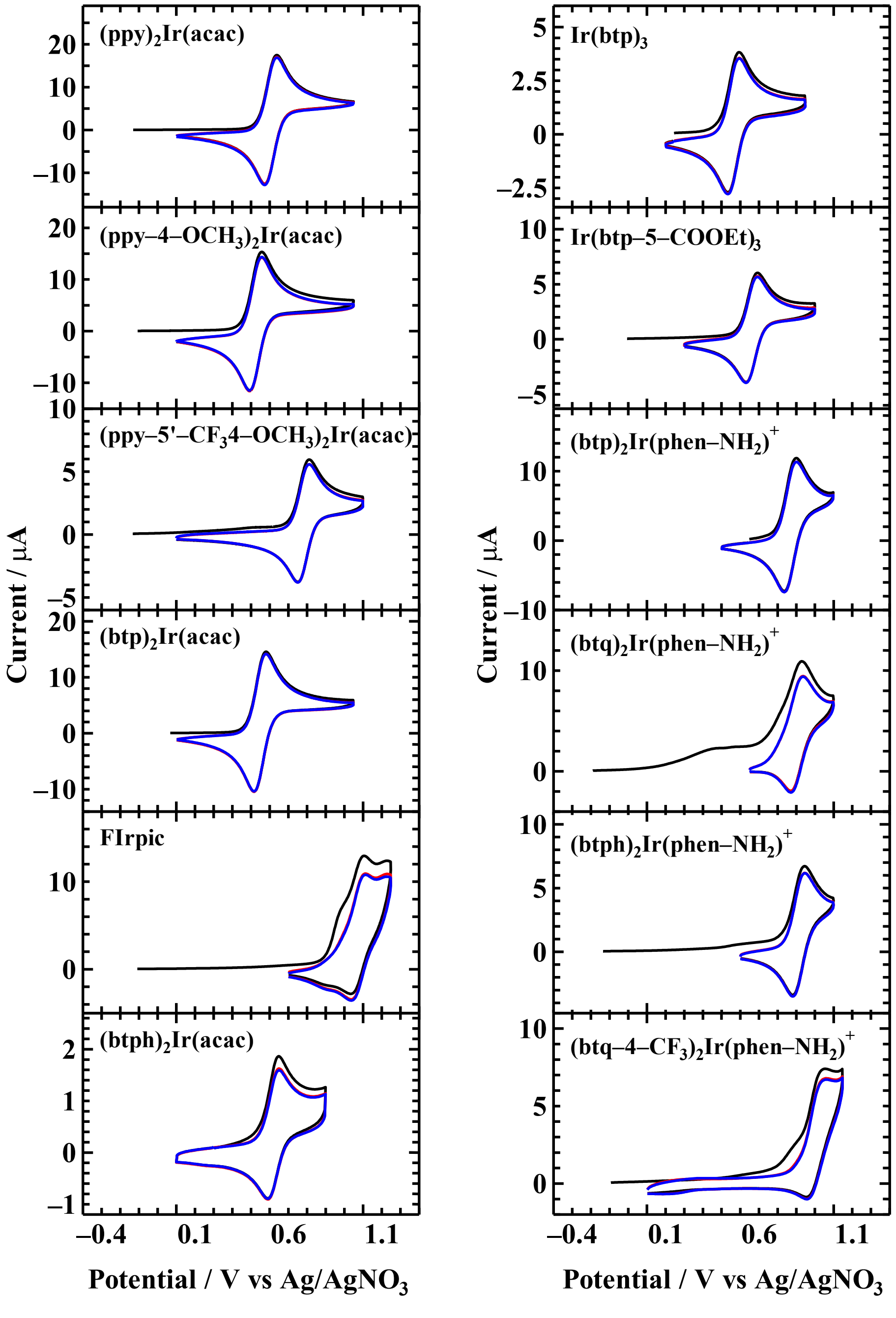

Figure 2-7. Cyclic voltammograms of Ir(III) complexes used in this study in Ar-saturated CH_3CN in the presence of 0.1-M $TBAPF_6$.

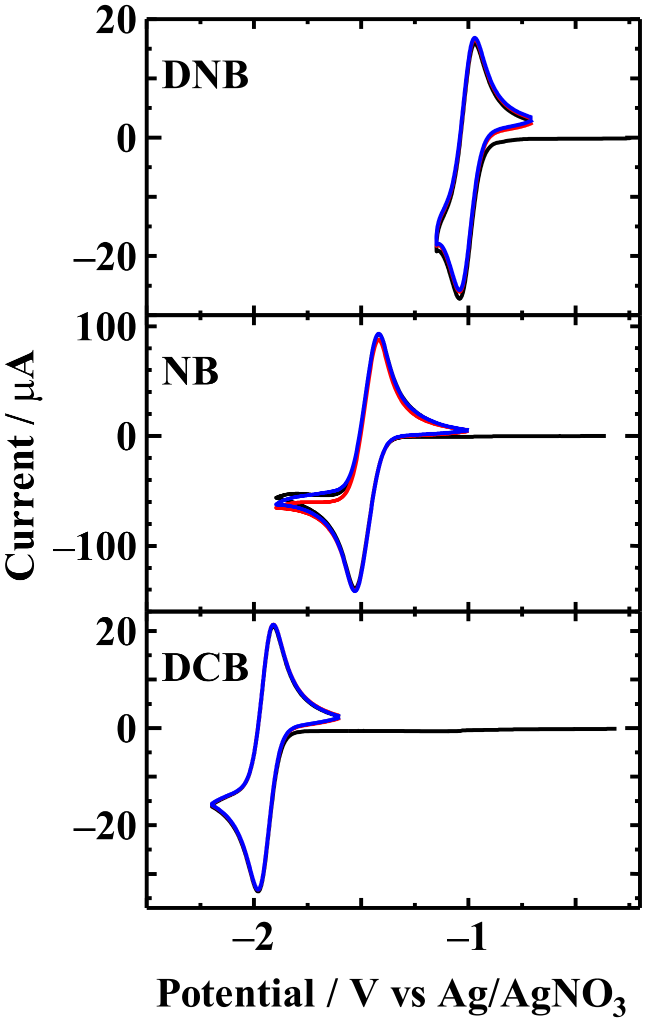

Figure 2-8. Cyclic voltammograms of DNB, NB, and DCB in Ar-saturated CH_3CN in the presence of 0.1-M $TBAPF_6$.

Table 2-1. Phosphorescence maximum wavelength ($\lambda_{\mathrm{phos}}^{\mathrm{max}}$), triplet energy (E_{T}), and half-wave oxidation potentials ($E_{\mathrm{ox}}^{1/2}$) of each Ir(III) complex.

Ir(III) complex	$\lambda_{\mathrm{phos}}^{\mathrm{max}}$/nm[a]	E_{T}/eV[a]	$E_{\mathrm{ox}}^{1/2}$ /V vs SCE
$(ppy)_2Ir(acac)$	507	+2.45	+0.83
$(ppy\text{-}4\text{-}OCH_3)_2Ir(acac)$	499	+2.48	+0.76
$(ppy\text{-}5'\text{-}CF_3\text{-}4\text{-}OCH_3)_2Ir(acac)$	487	+2.55	+1.02
$(btp)_2Ir(acac)$	607	+2.04	+0.77
FIrpic	461	+2.69	+1.30
$(btph)_2Ir(acac)$	703	+1.76	+0.85
$Ir(btp)_3$	589	+2.11	+0.80
$Ir(btp\text{-}5\text{-}COOEt)_3$	632	+1.96	+0.89
$(btp)_2Ir(phen\text{-}NH_2)^+$	584	+2.12	+1.09
$(btq)_2Ir(phen\text{-}NH_2)^+$	640	+1.94	+1.12
$(btph)_2Ir(phen\text{-}NH_2)^+$	698	+1.78	+1.14
$(btq\text{-}4\text{-}CF_3)_2Ir(phen\text{-}NH_2)^+$	697	+1.78	+1.24

[a] Recorded in 2-MeTHF at 77 K.

2-3-2 Electron Transfer Reactivities of Excited Triplet Ir(III) Complexes with Aromatic Electron Acceptors

In this section, the electron-transfer reactivities of the Ir(III) complexes in CH_3CN was investigated using AEAs. The absorption spectra of Ir(III) complexes were not changed in the presence of AEAs, suggesting that the possibility of the interaction between their ground states can be neglected. Typical phosphorescence decay curves and the Stern–Volmer plots of $\tau_p{}^0/\tau_p$ vs AEA concentrations are shown in Figure 2-9 and Figure 2-10, respectively. The phosphorescence of these complexes were significantly quenched in the presence of AEAs, suggesting that the Ir(III) complexes in the excited triplet state were oxidized. The phosphorescence quenching rate constants (k_q) obtained from the Stern–Volmer analyses are listed in Table 2-2. Because the lowest triplet state energies of AEAs are nearly equal to or greater than those of the complexes used in this study [37], electronic energy transfer is energetically unfavorable for all of the systems examined. Therefore, it is considered that the quenching is due to photoinduced electron transfer (PET) reactions from the Ir(III) complexes in the excited triplet state (${}^3D^*$) to the electron acceptors (A), as shown in eq 2-2

$$ {}^3\mathbf{D}^* + \mathbf{A} \underset{k_{-\mathrm{d}}}{\overset{k_{\mathrm{d}}}{\rightleftarrows}} ({}^3\mathbf{D}^*\cdots\mathbf{A}) \underset{k_{-\mathrm{el}}}{\overset{k_{\mathrm{el}}}{\rightleftarrows}} (\mathbf{D}^{\cdot +}\cdots\mathbf{A}^{\cdot -}) \xrightarrow{k_{\mathrm{s}}} \mathbf{D}^{\cdot +} + \mathbf{A}^{\cdot -} \qquad (2\text{-}2), $$

where k_d and k_{-d} are the diffusion and the dissociation rate constants, k_{el} and k_{-el} are the electron transfer and back electron-transfer rate constants, and k_s is the separation rate constant, respectively. The overall quenching rate constant (k_q) shown in eq 2-3 was derived by applying the steady-state approximation to eq 2-2:

$$k_{\mathrm{q}} = \frac{k_{\mathrm{d}}}{1 + \frac{k_{-\mathrm{d}}}{k_{\mathrm{el}}}\left(1 + \frac{k_{-\mathrm{el}}}{k_{\mathrm{s}}}\right)} \qquad (2\text{-}3).$$

According to the classical model of the absolute rate theory, k_{el} and $k_{-\mathrm{el}}/k_{\mathrm{el}}$ can be written as the following equations

$$k_{\mathrm{el}} = k_{\mathrm{el}}^{0} e^{-\Delta G_{\mathrm{el}}^{\neq}/RT} \qquad (2\text{-}4) \text{ and}$$

$$k_{-\mathrm{el}} / k_{\mathrm{el}} = e^{\Delta G_{\mathrm{el}}/RT} \qquad (2\text{-}5),$$

where k_{el}^{0}, $\Delta G_{\mathrm{el}}^{\neq}$, ΔG_{el}, R, and T are the preexponential factor, the activation Gibbs energy of electron transfer, the Gibbs energy change for electron transfer, the gas constant, and temperature, respectively. From eqs 2-4 and 2-5, eq 2-3 can be described as eq 2-6:

$$k_{\mathrm{q}} = \frac{k_{\mathrm{d}}}{1 + \frac{k_{-\mathrm{d}}}{k_{\mathrm{s}}} e^{\Delta G_{\mathrm{el}}/RT} + \frac{k_{-\mathrm{d}}}{k_{\mathrm{el}}^{0}} e^{\Delta G_{\mathrm{el}}^{\neq}/RT}} \qquad (2\text{-}6).$$

The $\Delta G_{\mathrm{el}}^{\neq}$ value can be related to the ΔG_{el} value by the Agmon–Levine equation [38,39].

$$\Delta G_{\mathrm{el}}^{\neq} = \Delta G_{\mathrm{el}} + \frac{\Delta G_{\mathrm{el}}^{\neq}(0)}{\ln 2} \ln\left(1 + e^{-\Delta G_{\mathrm{el}} \ln 2 / \Delta G_{\mathrm{el}}^{\neq}(0)}\right) \qquad (2\text{-}7),$$

where $\Delta G_{\mathrm{el}}^{\neq}(0)$ is the reorganizational intrinsic barrier (the Gibbs energy of activation for $\Delta G_{\mathrm{el}} = 0$).

The Gibbs energy change (ΔG_{el}) for the electron-transfer reactions from Ir(III) complexes in the T_1 state to AEAs can be estimated from the standard Rehm–Weller treatment [40] as

$$\Delta G_{el} = E_{ox}(D) - E_{red}(A) - E_T + C \qquad (2\text{-}8),$$

where $E_{ox}(D)$, $E_{red}(A)$, and C are the oxidation potential of the Ir(III) complexes, the reduction potential of the AEAs, and the electrostatic interaction energy (−0.06 and −0.12 eV for neutral and cationic Ir(III) complexes, respectively). Table 2-2 shows the calculated ΔG_{el} values, along with the k_q values.

The Rehm–Weller plots of $\log k_q$ against ΔG_{el} for the Ir(III) complex/AEA systems are shown in Figure 2-11. The fitting curve in Figure 2-11 was calculated using eqs 2-6 and 2-7, where $k_{-d}/k_s = 0.16$, $k_{-d}/k_{el}^{0} = 0.16$, T=298 K and $\Delta G_{el}^{\neq}(0) = 0.18$ eV. As can be seen from Figure 2-11, the k_q values increase with the decrease of ΔG_{el} and reach a limiting value when the ΔG_{el} values are less than approximately −0.8 eV. From the fitting equation, the limiting k_q value (k_d) for the Ir(III) complex/AEA systems was evaluated to be 2.0×10^{10} $M^{-1}s^{-1}$ in CH_3CN at 298 K. For the Ir(III) complex/AEA systems with $\Delta G_{el} \lesssim -0.8$ eV, the phosphorescence quenching of Ir(III) complexes takes place at the diffusion-controlled rate in CH_3CN [37]. The similar results for the phosphorescence quenching of *fac*-Ir(ppy)$_3$ using different quenchers have been reported by Watts et al. [41]

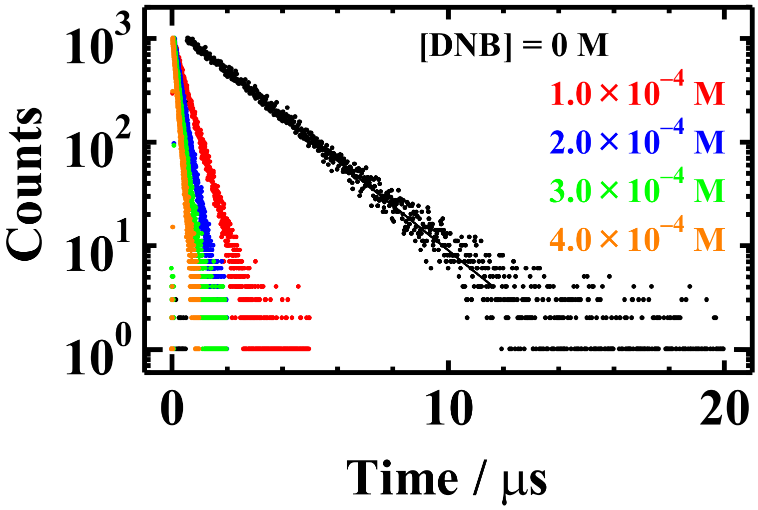

Figure 2-9. Phosphorescence decay curves of $(ppy)_2Ir(acac)$ in the presence of DNB in degassed CH_3CN.

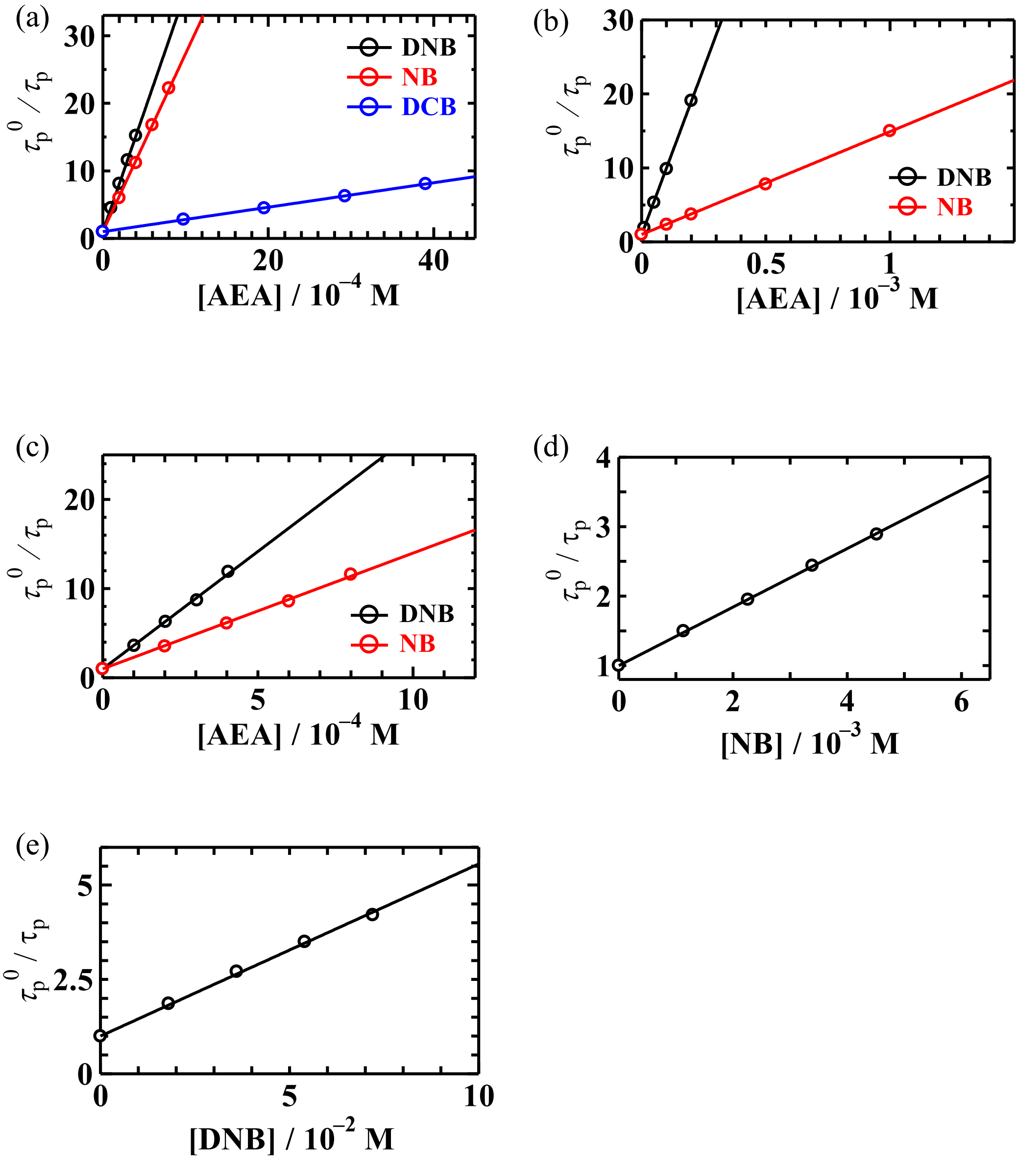

Figure 2-10. Stern–Volmer plots τ_p^0/τ_p vs AEA concentration for (a) (ppy)$_2$Ir(acac), (b) (btp)$_2$Ir(acac), (c) FIrpic, (d) (btp)$_2$Ir(phen-NH$_2$)$^+$, and (e) (btq-4-CF$_3$)$_2$Ir(phen-NH$_2$)$^+$.

Table 2-2. Quenching rate constant (k_q) and Gibbs energy change (ΔG_{el}) of electron-transfer reaction for the Ir(III) complex/AEA systems.

Ir(III) complex	Quencher	k_q/M^{-1} s^{-1}	ΔG_{el}/eV
$(ppy)_2Ir(acac)$	DNB	1.8×10^{10}	−1.0
FIrpic	DNB	1.5×10^{10}	−0.77
$(btp)_2Ir(acac)$	DNB	1.5×10^{10}	−0.65
$(ppy)_2Ir(acac)$	NB	1.3×10^{10}	−0.54
FIrpic	NB	6.6×10^{9}	−0.31
$(btp)_2Ir(acac)$	NB	2.3×10^{9}	−0.19
$(ppy)_2Ir(acac)$	DCB	9.3×10^{8}	−0.070
$(btp)_2Ir(phen\text{-}NH_2)^+$	NB	5.9×10^{7}	−0.010
$(btq\text{-}4\text{-}CF_3)_2Ir(phen\text{-}NH_2)^+$	DNB	3.7×10^{7}	+0.020

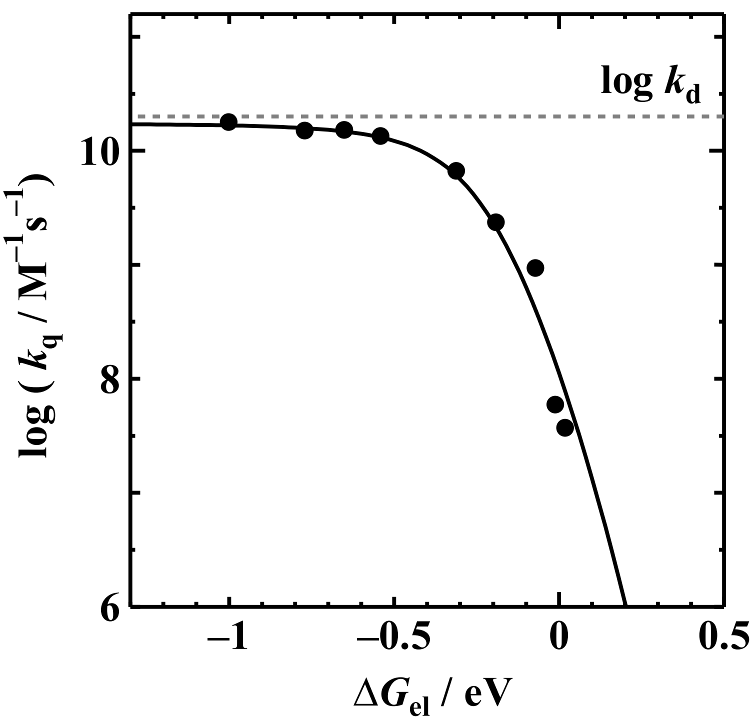

Figure 2-11. Rehm-Weller plots of logk_q vs ΔG_{el} for the phosphorescence quenching of Ir(III) complexes by AEAs.

Transient absorption measurements were performed to confirm the occurrence of electron-transfer reactions from Ir(III) complexes to AEAs. If the electron transfer reactions from the excited triplet Ir(III) complexes to AEAs are involved, the cation radicals of Ir(III) complexes and the anion radicals of AEAs will be observed. Figure 2-12a and 2-12b show the transient absorption spectra of $(ppy)_2Ir(acac)$ in the absence and presence of DCB ([DCB] = 3.2×10^{-3} M) in degassed CH_3CN, respectively. The decay rate of the entire absorption spectrum in Figure 2-12a was accelerated by molecular oxygen in air-saturated CH_3CN; thus, the observed absorption spectrum can be assigned to the triplet-triplet absorption (TTA) of $(ppy)_2Ir(acac)$ in the excited triplet state. Also, in Figure 2-12b, the spectrum taken at 0.1 μs after laser pulsing is attributable to the TTA of $(ppy)_2Ir(acac)$ because this spectrum has a similar shape with Figure 2-12a. With the decay of the triplet absorption bands, long-lived absorption bands derived from the $(ppy)_2Ir(acac)$ cation radical and the DCB anion radical appear in the wavelength regions longer than 470 nm and shorter than 500 nm, respectively. Here, the absorption bands were assigned by comparing the observed transient absorption spectra with the absorption spectra of the $(ppy)_2Ir(acac)$ cation radical and the DCB anion radical, which were obtained via spectroelectrochemical measurements (see Figures 2-12c and 2-12d). Because the transient absorption spectrum taken at 1.5 μs after laser pulsing (green spectrum in Figure 2-12b) consists of the absorption spectrum of the $(ppy)_2Ir(acac)$ cation radical (Figures 2-12c) and that of the DCB anion radical (Figure 2-12d), it can be confirmed that the $(ppy)_2Ir(acac)$ cation radical and the DCB anion radical were produced. The time profile of each transient absorption band is traced in Figure 2-13. As evident in Figure 2-13, with the decay of the TTA due to $(ppy)_2Ir(acac)$ in the excited triplet state at

490 nm, the time profile of the band at 430 nm shows an increase in ΔOD, indicating production of the DCB anion radical. As shown at 650 nm, the absorption due to the $(ppy)_2Ir(acac)$ cation radical remains after the disappearance of the triplet absorption. The transient absorption spectra of $(ppy)_2Ir(acac)$, $(btp)_2Ir(acac)$, and FIrpic in the presence of DNB or NB in degassed CH_3CN are shown in Figure 2-14. Here, it is known that DNB anion radical exhibits the absorption in the wavelength regions of 380–530 and 640–930 nm and NB anion radical gives an absorption band at around 465 nm [42]. In the presence of DNB, the transient absorption bands arising from each Ir(III) complex cation radical and DNB anion radical were observed. In the presence of NB, the transient absorption spectrum of cation radical of each Ir(III) complex appeared, while that of NB anion radical was not observed in $(ppy)_2Ir(acac)$ and $(btp)_2Ir(acac)$ solutions because the molar absorption coefficient of NB anion radical might be comparable with or smaller than that of these complexes in the ground state. In contrast, the transient absorption due to the NB anion radical was detected at around 465 nm in FIrpic solution. These results indicate the occurrence of photoinduced electron-transfer (PET) reactions in these systems. The possible reaction sequence for the electron-transfer reaction between the excited triplet Ir(III) complexes and AEAs can be expressed as shown in Scheme 2-2.

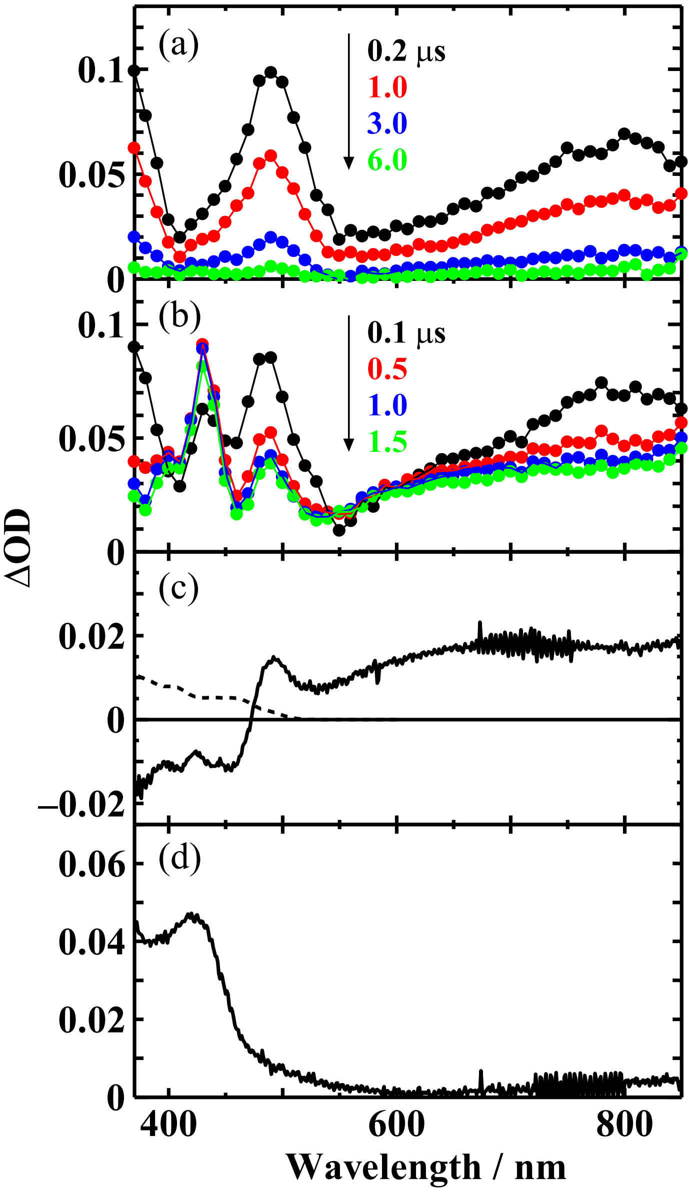

Figure 2-12. Transient absorption spectra of $(ppy)_2Ir(acac)$ in the absence and presence of DCB (3.2×10^{-3} M) in degassed CH_3CN ((a) and (b), respectively), and the absorption spectra of (c) the $(ppy)_2Ir(acac)$ cation (broken line shows the absorption spectrum of $(ppy)_2Ir(acac)$ in the ground state) and (d) the DCB anion radicals in CH_3CN at room temperature.

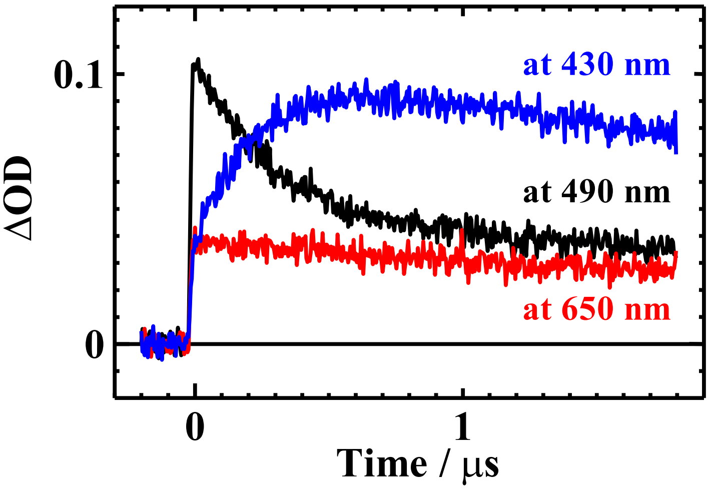

Figure 2-13. Time profiles of $(ppy)_2Ir(acac)$ in the presence of DCB (black line: λ_{mon} = 490 nm; red line: λ_{mon} = 650 nm; blue line: λ_{mon} = 430 nm) in degassed CH_3CN.

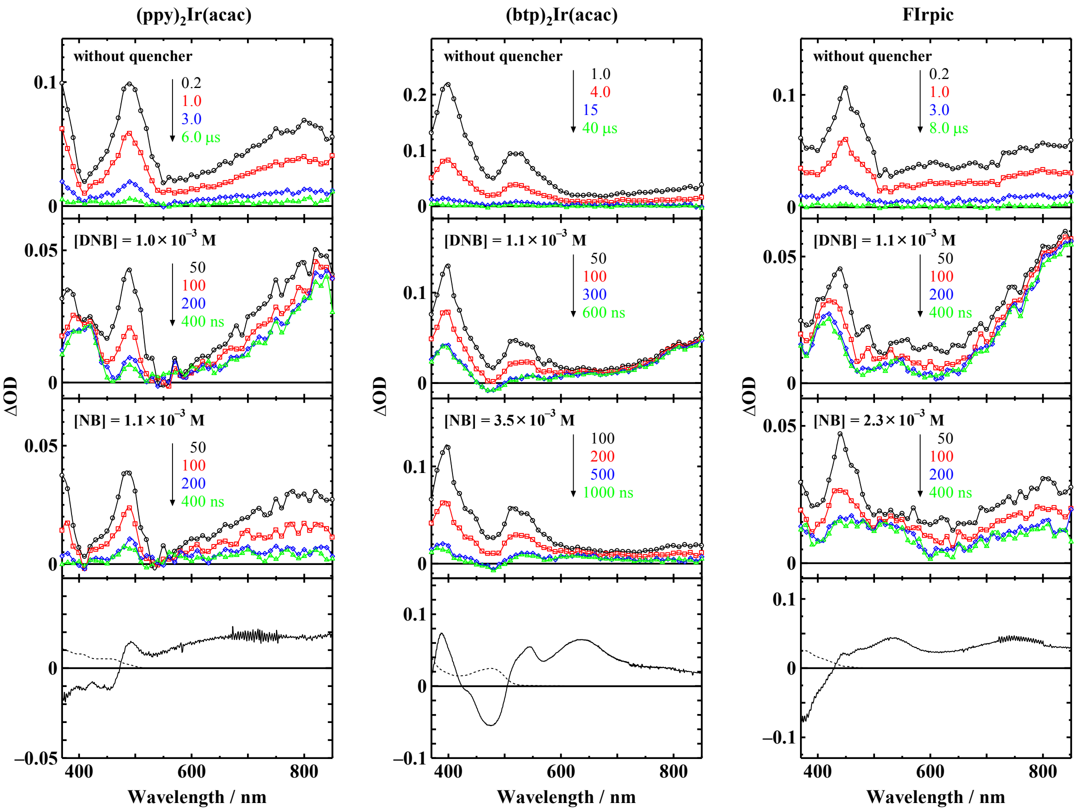

Figure 2-14. Transient absorption spectra of (ppy)$_2$Ir(acac), (btp)$_2$Ir(acac), and FIrpic in the absence and presence of AEAs in degassed CH_3CN, and the absorption spectra of cation radical of each Ir(III) complex (broken line shows the absorption spectra of each Ir(III) complex in the ground state).

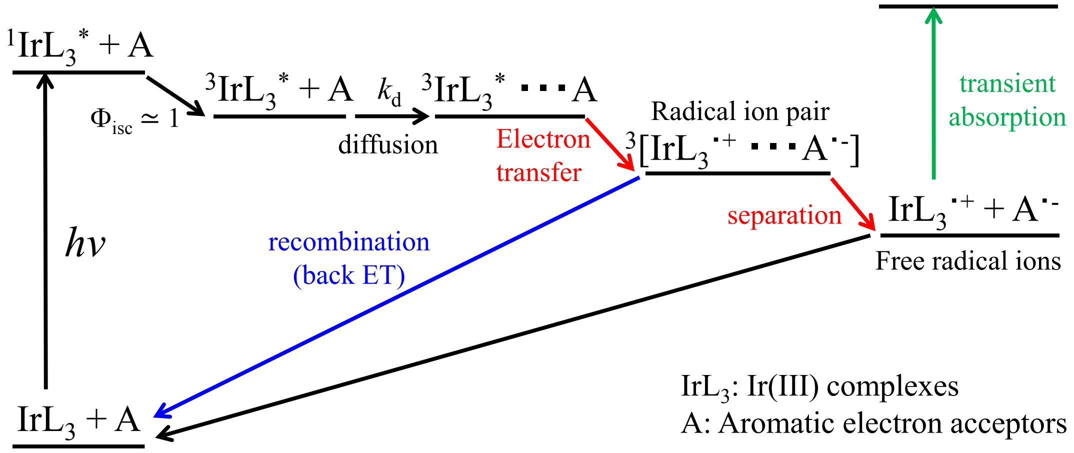

Scheme 2-2. Reaction sequence involving electron transfer between the excited triplet Ir(III) complex and aromatic electron acceptor.

To reveal the separation yield (ϕ_{sep}) of the radical ion pairs produced by electron transfer to free radical ions, the quantum yield (Φ_{rad}) of anion radical formation of Ir(III) complex/DNB systems in degassed CH_3CN was calculated from transient absorption measurements. First, the DNB anion radical yields ($\Phi_{\mathrm{rad}}^{\mathrm{DNB}^{\bullet-}}$) were determined by measuring the transient absorption of $\mathrm{DNB}^{\bullet-}$ at 840 nm in the presence of different concentrations of DNB according to the following equation

$$\Phi_{\mathrm{rad}}^{\mathrm{DNB}^{\bullet-}} = \frac{\Delta \mathrm{OD}_{840\,\mathrm{nm}}^{\mathrm{DNB}^{\bullet-}}}{I_0 \times \varepsilon_{840\,\mathrm{nm}}^{\mathrm{DNB}^{\bullet-}}} \qquad (2\text{-}9),$$

where $\Delta \mathrm{OD}_{840\,\mathrm{nm}}^{\mathrm{DNB}^{\bullet-}}$, I_0, and $\varepsilon_{840\,\mathrm{nm}}^{\mathrm{DNB}^{\bullet-}}$ are the absorbance change of the DNB anion radical at 840 nm, the photon flux absorbed by Ir(III) complex, and the molar absorption coefficient of the DNB anion radical at 840 nm ($\varepsilon_{840\,\mathrm{nm}}^{\mathrm{DNB}^{\bullet-}}$ = 12,000 $\mathrm{M}^{-1}\mathrm{cm}^{-1}$) [43], respectively; I_0 was determined using benzophenone (BP) in CH_3CN as an actinometer. Because the transient absorption at 840 nm included, in part, the absorption of each Ir(III) complex cation radical, $\Delta \mathrm{OD}_{840\,\mathrm{nm}}^{\mathrm{DNB}^{\bullet-}}$ was corrected using the absorption spectra of each Ir(III) complex cation radical shown in Figure 2-14.

Figure 2-15 shows the plots of $\Phi_{\mathrm{rad}}^{\mathrm{DNB}^{\bullet-}}$ against the DNB concentration for the Ir(III) complex/DNB systems. The $\Phi_{\mathrm{rad}}^{\mathrm{DNB}^{\bullet-}}$ value was expressed the following equation:

$$\Phi_{\mathrm{rad}}^{\mathrm{DNB}^{\bullet-}} = \frac{\Phi_{\mathrm{isc}} \times k_{\mathrm{q}}[\mathrm{DNB}] \times \phi_{\mathrm{el}} \times \phi_{\mathrm{sep}}}{k_{\mathrm{q}}[\mathrm{DNB}] + (\tau_{\mathrm{p}}^{0})^{-1}} \qquad (2\text{-}10).$$

In this equation, Φ_{isc} is the quantum yield of intersystem crossing of Ir(III) complex, which is assumed to be unity [44], k_{q} is the phosphorescence quenching rate constant of

Ir(III) complex by DNB, ϕ_{el} is the yield of electron transfer in the quenching processes by DNB, and τ_{p}^{0} is the phosphorescence lifetime of each Ir(III) complex under the degassed condition, respectively. Because the electron transfer is presumed to be the dominant quenching mechanism, the ϕ_{el} value can be assumed to be unity. The plots in Figure 2-15 were fitted to eq 2-10 to give the solid curves with a ϕ_{sep} value of 0.12, 0.10, and 0.17 for $(ppy)_2Ir(acac)$/DNB, $(btp)_2Ir(acac)$/DNB, and FIrpic/DNB systems, respectively. Here the electron transfer from the triplet Ir(III) complexes to DNB produces triplet radical ion pair. Because the recombination reaction in the triplet radical ion pair is spin-forbidden, the ϕ_{sep} is expected to be close to unity. However, these systems gave significantly small ϕ_{sep} values, suggesting the presence of fast recombination reactions. The fast back-electron transfer in the triplet radical ion pair was attributed to enhanced spin−orbit coupling due to the central Ir(III) ion that facilitates spin inversion from the triplet to the singlet radical ion pair. Similar observations have been reported by Olmsted et al. [45] for the PET reactions of Ru(II) and Os(II) complexes and methylviologen.

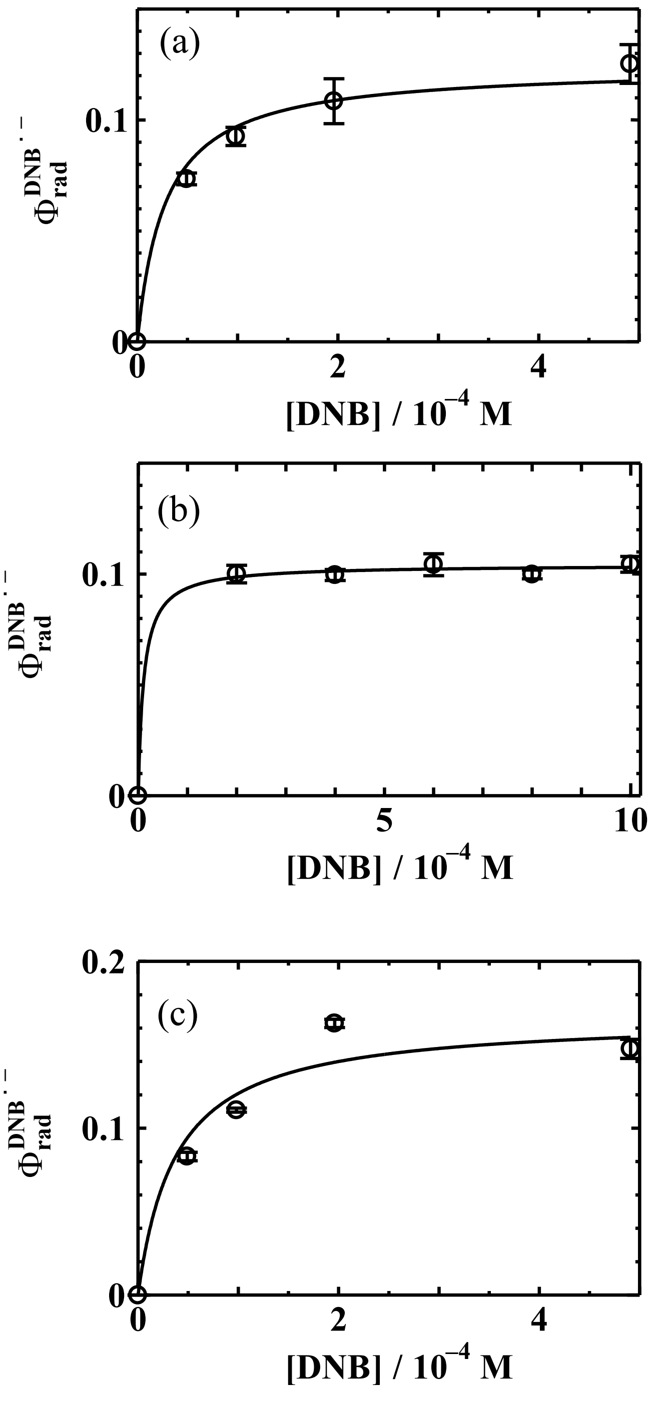

Figure 2-15. Plots of quantum yield ($\Phi_{rad}^{DNB^{\bullet-}}$) vs DNB concentrations obtained for the (a) $(ppy)_2Ir(acac)$/DNB, (b) $(btp)_2Ir(acac)$/DNB, and (c) FIrpic/DNB systems in degassed CH_3CN. The solid line represents a fitting curve based on eq 2-10.

2-3-3 Phosphorescence Quenching of Ir(III) Complexes by Molecular Oxygen

In this section, the phosphorescence quenching mechanisms of Ir(III) complexes by molecular oxygen in CH_3CN were investigated. As shown in Figure 2-16, Stern–Volmer plots of the τ_p^0/τ_p vs oxygen concentrations for all the complexes in CH_3CN showed linear relationships. The k_q values calculated from the slope of Figure 2-16 are summarized in Table 2-3. The k_q values vary from 1.4×10^9 to 2.0×10^{10} $M^{-1}s^{-1}$, depending on the reactivity of the excited triplet Ir(III) complexes with the ground-state molecular oxygen, $O_2(X^3\Sigma_g^-)$. The phosphorescence lifetimes (τ_p^0 and τ_p^{air}) of all the complexes under nitrogen-saturated and air-saturated conditions are also shown in Table 2-3.

The quantum yield (Φ_Δ) of singlet oxygen $O_2(a^1\Delta_g)$ formation following the phosphorescence quenching of Ir(III) complexes by $O_2(X^3\Sigma_g^-)$ in air-saturated CH_3CN was determined by measuring the emission intensity (I_Δ(Ir)) of the $O_2(a^1\Delta_g)$ at 1270 nm. Figure 2-17 shows the emission spectrum arising from the $a^1\Delta_g$ (v′= 0) → $X^3\Sigma_g^-$ (v″= 0) transition of singlet oxygen in the presence of FIrpic as a photosensitizer in air-saturated CH_3CN, and the obtained Φ_Δ values are summarized in Table 2-3. Under triplet sensitization, Φ_Δ is expressed as the product of the quantum yield of intersystem crossing (Φ_{isc}) for Ir(III) complexes, the fraction (P_{T,O_2}) of the excited triplet state quenched by molecular oxygen, and the fraction (f_Δ) leading to formation of $^1O_2$ in the oxygen quenching of Ir(III) complexes in air-saturated CH_3CN,

$$\Phi_\Delta = \Phi_{isc} P_{T,O_2} f_\Delta \qquad (2\text{-}11),$$

where $P_{\mathrm{T,O_2}}$ is obtained using the phosphorescence lifetime ($\tau_{\mathrm{p}}^{\mathrm{air}}$) of the air-saturated solution as 1 − $\tau_{\mathrm{p}}^{\mathrm{air}} / \tau_{\mathrm{p}}^{0}$. Because Φ_{isc} for Ir(III) complexes can be assumed to be unity [44], the f_{Δ} values can be calculated from eq 2-11. The obtained f_{Δ} values vary in the range from 0.40 to 0.97 (Table 2-3).

The Gibbs energy change (ΔG_{el}) for the electron-transfer reaction from Ir(III) complexes to molecular oxygen was calculated using eq 2-8 in Section 2-3-2. Here, the reduction potential of O_2 (−0.87 V vs SCE) was evaluated by comparting the cyclic voltammograms obtained under air-saturated and Ar-saturated conditions (Figure 2-18). The calculated ΔG_{el} values are listed in Table 2-3, along with the k_{q} values; the k_{q} values for the Ir(III) complex/O_2 systems are plotted against ΔG_{el} in Figure 2-19 (green open circle), together with those of the Ir(III) complex/AEA systems and the f_{Δ} values. The fitting curve (green line) in Figure 2-19 was calculated according to eqs 2-6 and 2-7 in Section 2-3-2 using $k_{-\mathrm{d}}/k_{\mathrm{s}} = 0.16$, $k_{-\mathrm{d}} / k_{\mathrm{el}}^{0} = 0.16$, T=298 K, and $\Delta G_{\mathrm{el}}^{\neq}(0) = 0.22$ eV as fitting parameters. Here, the limiting k_{q} value was evaluated to be 2.5 × 10^{10} $\mathrm{M^{-1}s^{-1}}$. The k_{q} values for Ir(III) complex/O_2 systems tend to decrease with increasing ΔG_{el} and exhibit an inverse relationship with the f_{Δ} values. This result indicates the involvement of electron transfer in the phosphorescence quenching of Ir(III) complexes by molecular oxygen. Therefore, the time profile of transient absorption for $(ppy)_2Ir(acac)$ at 490 nm, which exhibits a large negative ΔG_{el} in air-saturated CH_3CN, was measured (Figure 2-20). However, the long-lived component due to the $(ppy)_2Ir(acac)$ cation radical was not observed, which suggests that the phosphorescence quenching of Ir(III) complexes by molecular oxygen proceeds through a CT interaction, as has been hypothesized for some aromatic hydrocarbons [46].

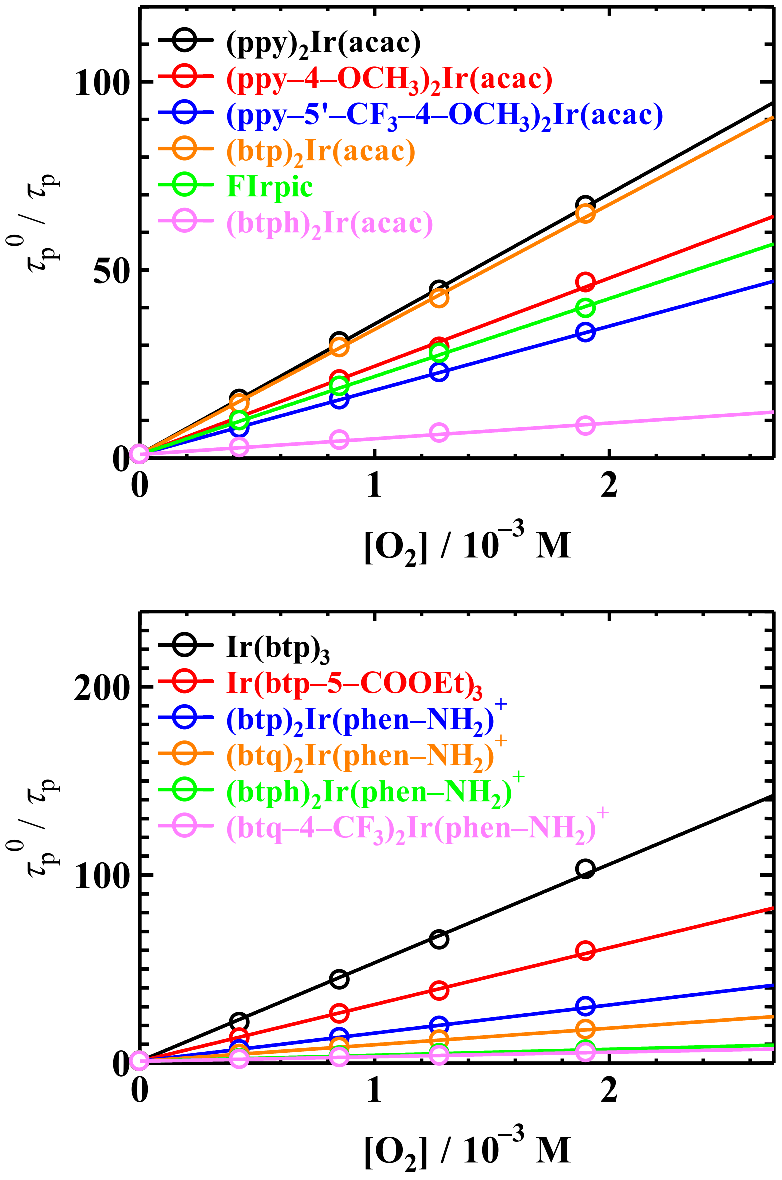

Figure 2-16. Stern–Volmer plots for the τ_p^0 / τ_p vs oxygen concentration in CH_3CN.

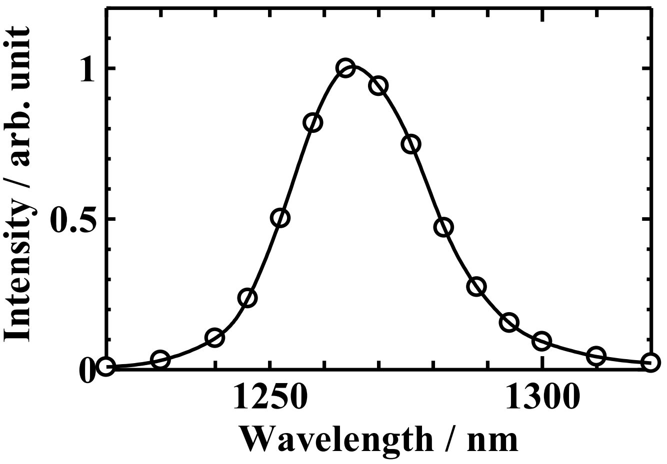

Figure 2-17. Emission spectrum of the $a^1\Delta_g$ ($v' = 0$) → $X^3\Sigma_g^-$ ($v'' = 0$) transition of molecular oxygen in the presence of FIrpic as a photosensitizer in air-saturated CH_3CN.

Table 2-3. Quenching rate constant (k_q) of Ir(III) complex in the excited triplet state by molecular oxygen, Gibbs energy change (ΔG_{el}) for the PET reaction, the quantum yield (Φ_Δ) of $^1O_2$ formation, the fraction (P_{T,O_2}) of the excited triplet state quenched by molecular oxygen, and the fraction (f_Δ) leading to formation of $^1O_2$ in the oxygen quenching of Ir(III) complexes in air-saturated CH_3CN.

Ir(III) complex	τ_p^0 /μs [a]	τ_p^{air} /μs [b]	k_q/10^9 $M^{-1}s^{-1}$ [c]	K_{SV} /10^4 M^{-1} [d]	ΔG_{el}/eV	Φ_Δ [c]	P_{T,O_2}	f_Δ [c]
(ppy-4-OCH_3)$_2$Ir(acac)	1.15	0.025	20	2.3	−0.91	0.39	0.98	0.40
(ppy)$_2$Ir(acac)	1.73	0.026	20	3.5	−0.81	0.39	0.98	0.40
(ppy-5′-CF_3-4-OCH_3)$_2$Ir(acac)	1.14	0.034	15	1.7	−0.72	0.51	0.97	0.53
FIrpic	1.74	0.044	12	2.1	−0.58	0.64	0.97	0.66
Ir(btp)$_3$	8.51	0.083	6.2	5.2	−0.50	0.59	0.99	0.60
(btp)$_2$Ir(acac)	5.26	0.081	6.3	3.3	−0.46	0.59	0.98	0.60
(btp)$_2$Ir(phen-NH_2)$^+$	6.11	0.204	2.4	1.5	−0.28	0.62	0.97	0.64
Ir(btp-5-COOEt)$_3$	6.58	0.111	4.6	3.0	−0.26	0.64	0.98	0.65
(btph)$_2$Ir(acac)	1.97	0.231	2.1	0.42	−0.10	0.85	0.88	0.97
(btq)$_2$Ir(phen-NH_2)$^+$	4.98	0.279	1.8	0.88	−0.070	0.77	0.94	0.82
(btph)$_2$Ir(phen-NH_2)$^+$	2.31	0.331	1.4	0.32	+0.11	0.79	0.86	0.92
(btq-4-CF_3)$_2$Ir(phen-NH_2)$^+$	1.25	0.223	1.9	0.24	+0.21	0.72	0.82	0.88

[a] Recorded under nitrogen-saturated conditions. [b] Recorded under air-saturated conditions. [c] Uncertainties ±5%. [d] $K_{SV} = k_q \times \tau_p^0$

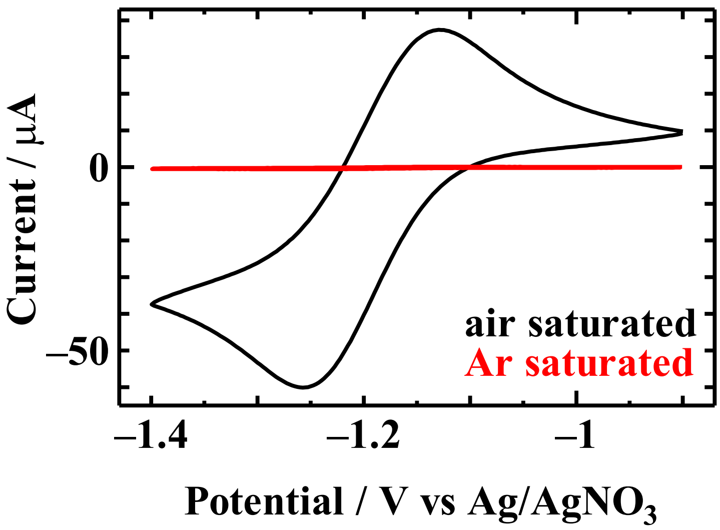

Figure 2-18. Cyclic voltammograms of O_2 in CH_3CN under air-saturated and Ar-saturated conditions.

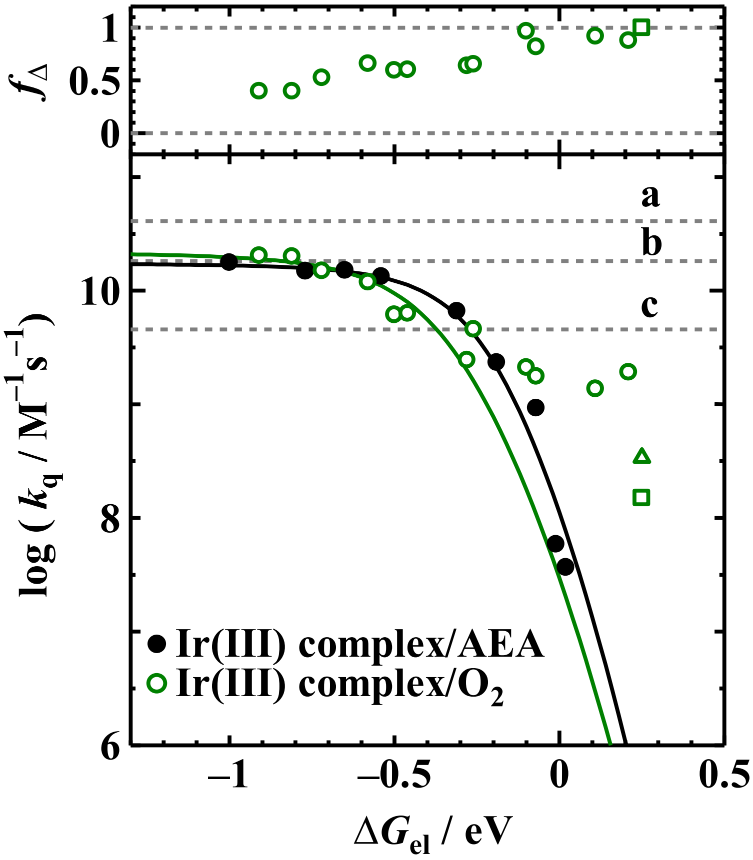

Figure 2-19. Rehm–Weller plots of the phosphorescence quenching of Ir(III) complexes by AEAs (black closed circle) and molecular oxygen (green open circle), and plots of f_Δ vs ΔG_{el}. The square and triangle symbols show the data for $Ir(bpy)_3^{3+}$ from refs. [27] and [25], respectively. The broken lines indicate (a) $\log k_d$, (b) $\log(4/9)k_d$, and (c) $\log(1/9)k_d$ for Ir(III) complex/O_2 system ($k_d = 4.1 \times 10^{10}$ $M^{-1}s^{-1}$).

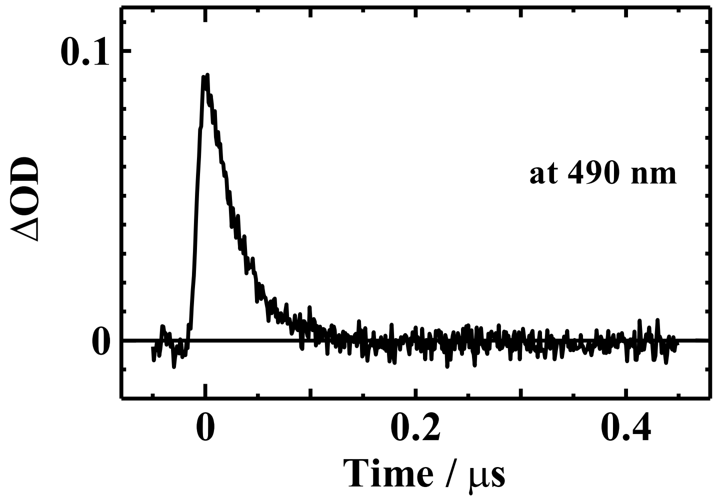

Figure 2-20. Time profile of $(ppy)_2Ir(acac)$ in air-saturated CH_3CN (λ_{mon} = 490 nm).

Here, the relation between the observed quenching rate constants (k_q) and the diffusion-controlled rate constant (k_d) is considered to reveal the phosphorescence quenching mechanism by molecular oxygen. According to the Smoluchowski equation [47], the diffusion-controlled rate constant for bimolecular reactions between molecules A and B can be expressed as

$$k_d = 4\pi N_A (D_A + D_B)(r_A + r_B) \qquad (2\text{-}12),$$

where N_A is Avogadro's constant, D_A and r_A are the diffusion coefficient and molecular radius of molecule A, and D_B and r_B are those of molecule B, respectively. Here, $(ppy)_2Ir(acac)$ was chosen as a representative Ir(III) complex in Figure 2-1 because the related data are available. The molecular radii of $(ppy)_2Ir(acac)$ and DNB were estimated from their X-ray diffraction data to be 5.75 Å [32] and 3.57 Å [48], respectively. Here, the distance between the central Ir(III) ion and the H atom of 5′-position in the phenyl ring and that from the center of benzene ring to the O atom of the nitro group were taken as the molecular radii of $(ppy)_2Ir(acac)$ and DNB, respectively. The diffusion coefficient of DNB in CH_3CN has been reported as 1.68×10^{-9} m^2s^{-1} [49], whereas that of $(ppy)_2Ir(acac)$ has not been reported. Hence, the diffusion coefficient (2.8×10^{-10} m^2s^{-1} in CH_2Cl_2 [50]) of *fac*-$Ir(ppy)_3$ was used in substitution for that of $(ppy)_2Ir(acac)$. The diffusion coefficient of *fac*-$Ir(ppy)_3$ in CH_3CN was approximated to be 3.6×10^{-10} m^2s^{-1} by using the viscosity of CH_2Cl_2 (0.449 mPa s) and CH_3CN (0.345 mPa s) [37]. The values of the diffusion coefficient and radius for molecular oxygen in CH_3CN have been reported to be 7.12×10^{-9} m^2s^{-1} [51] and 1.50 Å [52], respectively. By substituting the values for the diffusion coefficient and radius into eq 2-12, the k_d value for the Ir(III) complex/O_2 system was calculated to be 4.1×10^{10} $M^{-1}s^{-1}$, which was consistent with the reported value for the oxygen quenching of excited triplet aromatic hydrocarbons [46].

The logarithm of the calculated k_d value for the Ir(III) complex/O_2 system is plotted by the gray broken line in Figure 2-19, along with $\log(4/9k_d)$ and $\log(1/9k_d)$. As shown in Figure 2-19, the $\log k_d$ value for the Ir(III) complex/O_2 system is much larger than that for the Ir(III) complex/AEA systems because of the much larger diffusion coefficient of O_2 compared to those of AEAs. Also the different ΔG_{el} dependences were observed for the k_q values of the Ir(III) complex/AEA and the Ir(III) complex/O_2 systems. For the systems with $\Delta G_{el} \lesssim -0.2$ eV, the $\log k_q$ values of both systems give similar ΔG_{el} dependences, even though the Ir(III) complex/O_2 systems show slightly smaller $\log k_q$ values, which suggests a larger reorganization energy arising from the small molecular size of O_2. Actually, the fitting curve (green line) for the Ir(III) complex/O_2 system gave a larger $\Delta G^{\neq}_{el}(0)$ (0.22 eV) compared to that for the Ir(III) complex/AEA system (0.18 eV). The Ir(III) complex/O_2 systems with $\Delta G_{el} \gtrsim -0.2$ eV show more prominent quenching compared with the Ir(III) complex/AEA systems because of the involvement of energy transfer (internal conversion) leading to the formation of $^1O_2$, although the k_q values are less than $(1/9)k_d$. Here, the k_q values of $Ir(bpy)_3^{3+}$ reported by Demas et al. [25] and Abdel-Shafi et al. [27] were smaller than those for the other Ir(III) complexes. This is probably due to the fact that $Ir(bpy)_3^{3+}$ has a higher triplet energy compared with the other Ir(III) complexes.

In Scheme 2-1 in Section 2-1, intersystem crossing between encounter complexes with different multiplicity $^m(T_1{}^3\Sigma)$ (m = 1, 3, 5) is expected to be slow compared to complex dissociation or deactivation [53], and the CT rate constants ($^mk_{CT}$ (m = 1 and 3)) of the complexes with $\Delta G_{\mathrm{el}} \lesssim -0.1$ eV are evaluated to be much larger than the reverse CT rate constants (${}^{\mathrm{m}}k_{-\mathrm{CT}}$ (m = 1 and 3)) from the relation ${}^{\mathrm{m}}k_{\mathrm{CT}}/{}^{\mathrm{m}}k_{-\mathrm{CT}} = \exp(-\Delta G_{\mathrm{el}}/RT)$ for full-electron transfer at 298 K. Hence, ${}^{\mathrm{m}}k_{-\mathrm{CT}}$ can be neglected, and application of the steady-state approximation to the singlet, triplet, and quintet encounter pairs ${}^{1,3,5}(\mathrm{T}_1\ {}^3\Sigma)$ in Scheme 2-1 results in derivation of the equations for k_{q} and f_{Δ}

$$k_{\mathrm{q}} = k_{\mathrm{d}}\left(\frac{1}{9}\frac{{}^1k_{\mathrm{D}}}{k_{-\mathrm{d}}+{}^1k_{\mathrm{D}}} + \frac{1}{3}\frac{{}^3k_{\mathrm{D}}}{k_{-\mathrm{d}}+{}^3k_{\mathrm{D}}}\right) \qquad \text{(2-13) and}$$

$$f_{\Delta} = \frac{k_{\mathrm{d}}}{9}\left(\frac{{}^1k_{\mathrm{D}}}{k_{-\mathrm{d}}+{}^1k_{\mathrm{D}}}\right)\frac{1}{k_{\mathrm{q}}} \qquad \text{(2-14),}$$

where ${}^1k_{\mathrm{D}} = k_{\mathrm{ic}}^{1\Sigma} + k_{\mathrm{ic}}^{1\Delta} + {}^1k_{\mathrm{CT}}$ and ${}^3k_{\mathrm{D}} = k_{\mathrm{ic}}^{3\Sigma} + {}^3k_{\mathrm{CT}}$. Eqs 2-13 and 2-14 predict that, in highly exothermic electron transfer systems, CT processes become predominant and the maximum k_{q} value and the f_{Δ} value are expected to be $(4/9)k_{\mathrm{d}}$ and 0.25, respectively. However, the limiting k_{q} values for the systems with $\Delta G_{\mathrm{el}} \lesssim -0.8$ eV exceeded $4/9k_{\mathrm{d}}$, and the f_{Δ} values (0.40) were larger than 0.25 (Table 2-3). These results suggest that intersystem crossing between singlet, triplet, and quintet CT complexes cannot be neglected and that singlet-oxygen formation through the CT complexes is involved. CT interactions of O_2 with hydrocarbons have been reported to lead to an increase of spin–orbit coupling and to enhanced mixing of states of different multiplicities [54,55]. In addition, the strong heavy-atom effect of the central Ir(III) ion can accelerate the spin inversion, as observed for the Ir(III) complex/AEA systems. On the basis of these considerations, the phosphorescence quenching mechanism of Ir(III) complexes by molecular oxygen can be proposed as shown in Schemes 2-3 and 2-4, where kinetic schemes based on the energy-state diagrams for $(btq\text{-}4\text{-}CF_3)_2Ir(phen\text{-}NH_2)^+$ and FIrpic are depicted as examples for the systems with endothermic and exothermic ΔG_{el}, respectively. Figure 2-21 shows the energy-state diagram of encounter complex $^m(T_1{}^3\Sigma)$, full electron-transfer complex $^m(M^+O_2^-)$, and precursor complexes $^1(S_0{}^1\Sigma)$, $^1(S_0{}^1\Delta)$, and $^3(S_0{}^3\Sigma)$ for all Ir(III) complex/O_2 systems. It can be seen from Figure 2-21 that the Gibbs energy changes for electron transfer vary significantly depending on the energies of $^m(T_1{}^3\Sigma)$ and $^m(M^+O_2^-)$.

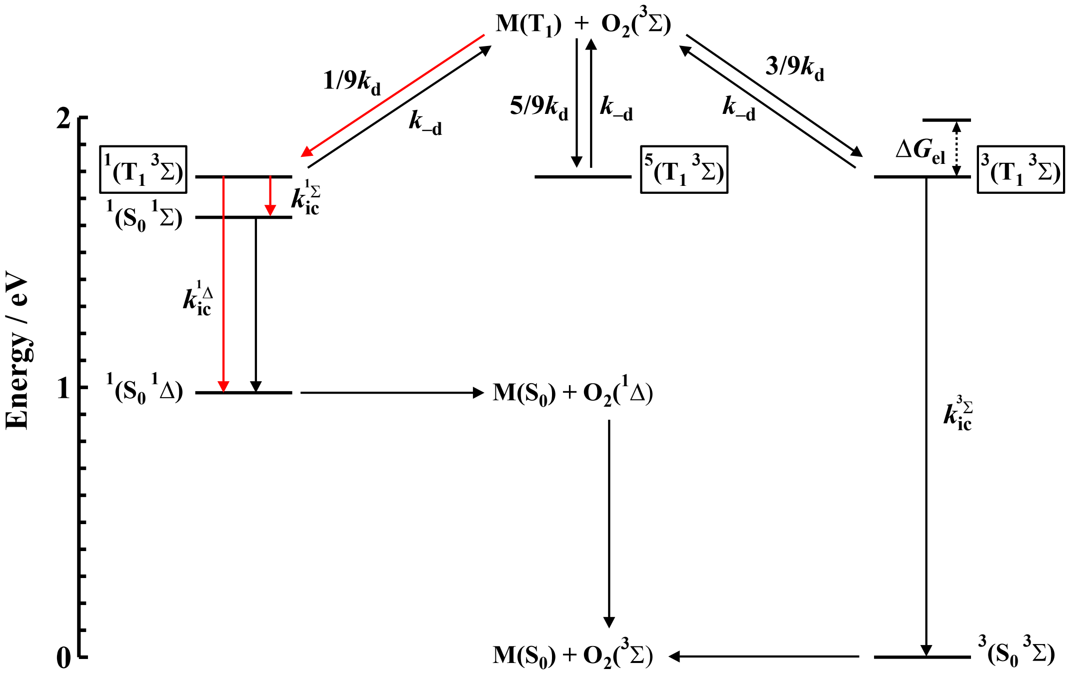

Scheme 2-3. Phosphorescence quenching pathways of Ir(III) complex/O_2 systems with $\Delta G_{\mathrm{el}} \gtrsim -0.2$ eV. Relative energies of $^{m}(T_1{}^{3}\Sigma)$ (m=1,3,5), $^{1}(S_0{}^{1}\Sigma)$, and $^{1}(S_0{}^{1}\Delta)$ against $^{3}(S_0{}^{3}\Sigma)$ for $(btq\text{-}4\text{-}CF_3)_2Ir(phen\text{-}NH_2)^+$ are depicted along with the principal deactivation processes.

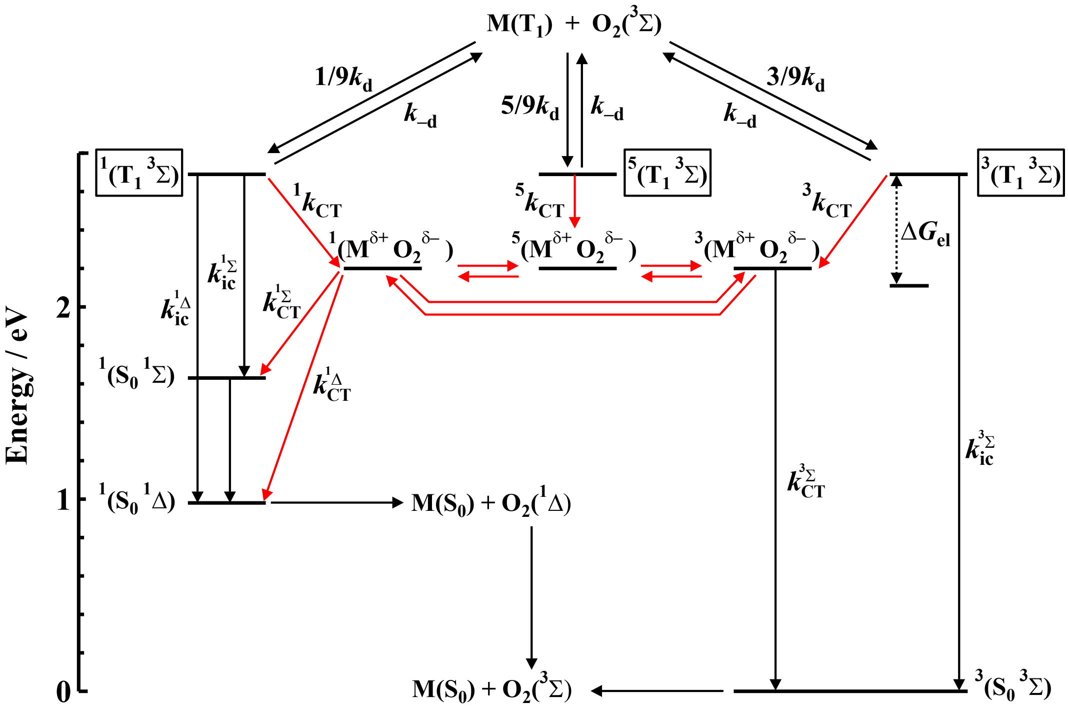

Scheme 2-4. Phosphorescence quenching pathways of Ir(III) complex/O$_2$ systems with $\Delta G_{el} \lesssim -0.2$ eV. Relative energies of $^m(T_1{}^3\Sigma)$ (m=1,3,5), $^1(S_0{}^1\Sigma)$, and $^1(S_0{}^1\Delta)$ against $^3(S_0{}^3\Sigma)$ for FIrpic are depicted along with the principal deactivation processes.

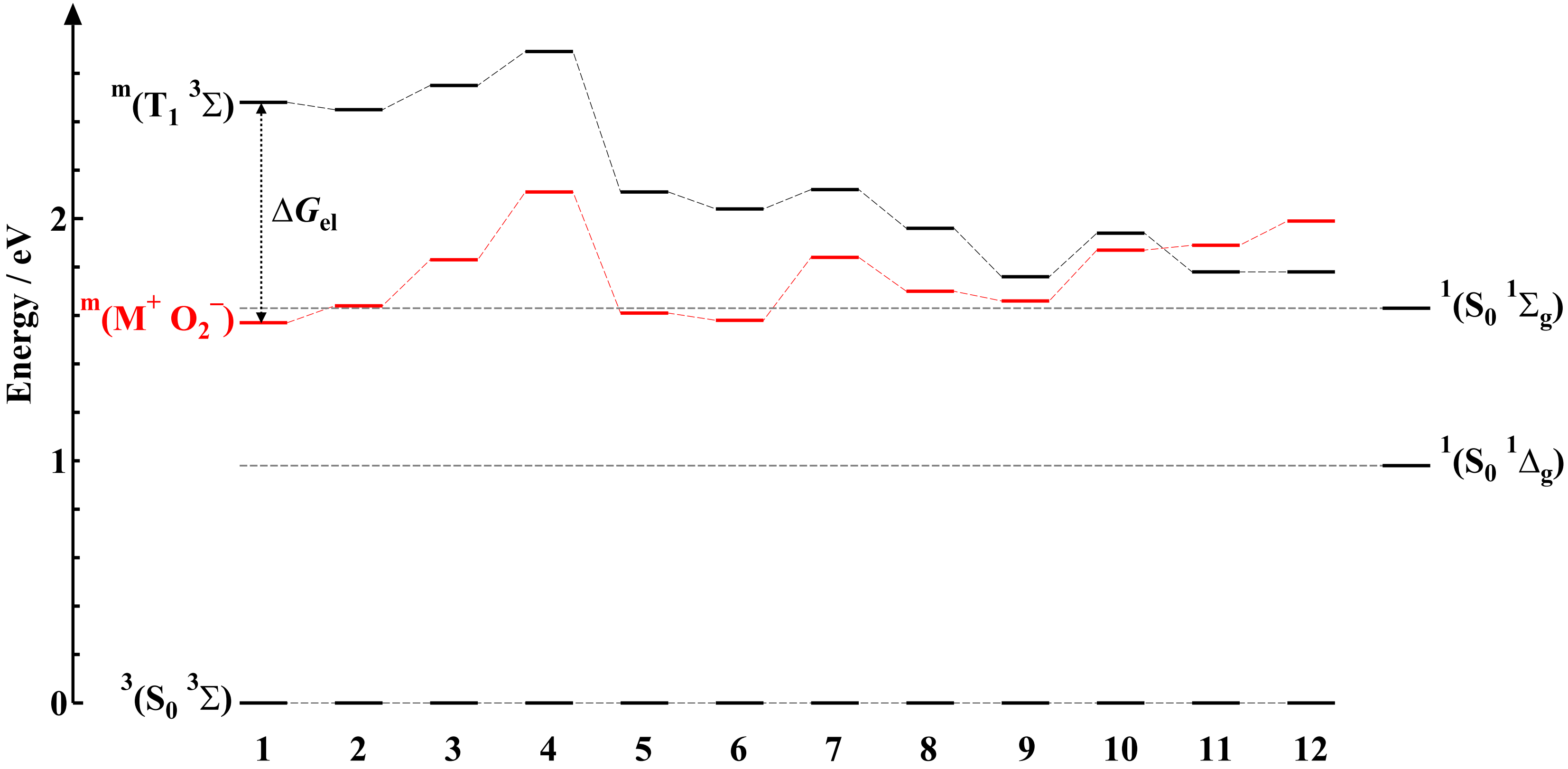

Figure 2-21. The energy state diagram of encounter complex $^{m}(T_1{}^3\Sigma)$ (m=1, 3, 5), full electron-transfer complex $^{m}(M^{+}O_2{}^{-})$, and precursor complexes $^{1}(S_0{}^1\Sigma)$, $^{1}(S_0{}^1\Delta)$, and $^{3}(S_0{}^3\Sigma)$ for all the Ir(III) complex/O_2 systems. 1: (ppy-4-OCH_3)$_2$Ir(acac), 2: (ppy)$_2$Ir(acac), 3: (ppy-5′-CF_3-4-OCH_3)$_2$Ir(acac), 4: FIrpic, 5: Ir(btp)$_3$, 6: (btp)$_2$Ir(acac), 7: (btp)$_2$Ir(phen-NH_2)$^+$, 8: Ir(btp-5-COOEt)$_3$, 9: (btph)$_2$Ir(acac), 10: (btq)$_2$Ir(phen-NH_2)$^+$, 11: (btph)$_2$Ir(phen-NH_2)$^+$, 12: (btq-4-CF_3)$_2$Ir(phen-NH_2)$^+$.

For the systems with $\Delta G_{\mathrm{el}} \gtrsim -0.1$ eV, ${}^{1}k_{\mathrm{CT}}$ and ${}^{3}k_{\mathrm{CT}}$ are considered to be negligibly small compared to ($k_{-\mathrm{d}} + k_{\mathrm{ic}}^{1\Sigma} + k_{\mathrm{ic}}^{1\Delta}$) and ($k_{-\mathrm{d}} + k_{\mathrm{ic}}^{3\Sigma}$); therefore, the following equations can be derived from eqs 2-13 and 2-14 for the internal conversion rate constants of singlet and triplet channels ($k_{\mathrm{ic}}^{1\Sigma} + k_{\mathrm{ic}}^{1\Delta}$ and $k_{\mathrm{ic}}^{3\Sigma}$):

$$k_{\mathrm{ic}}^{1\Sigma} + k_{\mathrm{ic}}^{1\Delta} = \frac{ak_{-\mathrm{d}}}{1-a} \qquad \text{(2-15) and}$$

$$k_{\mathrm{ic}}^{3\Sigma} = \frac{bk_{-\mathrm{d}}}{1-b} \qquad \text{(2-16).}$$

where $a = (9/k_{\mathrm{d}})k_{\mathrm{q}}f_{\Delta}$ and $b = (3/k_{\mathrm{d}})k_{\mathrm{q}}(1-f_{\Delta})$. According to the Eigen equation [56], the $k_{-\mathrm{d}}$ value was evaluated to be 4.3 × 10^{10} $\mathrm{M^{-1}s^{-1}}$. Thus, the magnitude of the internal conversion rate constants can be estimated by substituting the values of k_{d}, k_{q}, and f_{Δ} into eqs 2-15 and 2-16, respectively. The calculated $k_{\mathrm{ic}}^{1\Sigma} + k_{\mathrm{ic}}^{1\Delta}$ and $k_{\mathrm{ic}}^{3\Sigma}$ values for $\mathrm{(btph)_2Ir(phen\text{-}NH_2)^+}$ were 1.6 × 10^{10} $\mathrm{s^{-1}}$ and 3.5 × 10^{8} $\mathrm{s^{-1}}$, and those for $\mathrm{(btq\text{-}4\text{-}CF_3)_2Ir(phen\text{-}NH_2)^+}$ were 2.5 × 10^{10} $\mathrm{s^{-1}}$ and 7.3 × 10^{8} $\mathrm{s^{-1}}$, respectively. Kawaoka et al. proposed the expression for a theoretical internal conversion rate constant for excited sensitizer–oxygen complexes as eq 2-17 [57]:

$$k_{\mathrm{ic}} = \frac{2\pi}{\hbar}\beta^{2}F\rho(\Delta E) \qquad \text{(2-17),}$$

where β, F, and $\rho(\Delta E)$ are the electronic coupling matrix element, the Franck–Condon factor, and the density of final states with the excess energy ΔE. According to eq 2-17, the fast internal conversion of these complexes is attributable to the large Franck–Condon factor resulting from the extremely small energy gap (0.15 eV) between the T_1 state of these complexes and the ${}^{1}\Sigma_{g}^{+}$ state of molecular oxygen. Similar calculations were also performed for (btph)$_2$Ir(acac), (btq)$_2$Ir(phen-NH$_2$)$^+$, and Ir(bpy)$_3{}^{3+}$. The $k_{\mathrm{ic}}^{1\Sigma}+k_{\mathrm{ic}}^{1\Delta}$ values of (btph)$_2$Ir(acac) and (btq)$_2$Ir(phen-NH$_2$)$^+$ were evaluated to be 3.5×10^{10} s^{-1} and 2.0×10^{10} s^{-1}, and the calculated $k_{\mathrm{ic}}^{3\Sigma}$ values were 2.0×10^{8} s^{-1} and 1.0×10^{9} s^{-1}, respectively. The phosphorescence quenching rate constant of Ir(bpy)$_3{}^{3+}$ by molecular oxygen has been reported by Abdel-Shafi et al. [27] and Demas et al. [25] to be 1.5×10^{8} M^{-1}s^{-1} and 3.4×10^{8} M^{-1}s^{-1}, respectively; the value of f_{Δ} has been reported to be 1.0 [27]. On the basis of these data, $k_{\mathrm{ic}}^{1\Sigma}+k_{\mathrm{ic}}^{1\Delta}$ of Ir(bpy)$_3{}^{3+}$ was calculated to be 1.5×10^{9} s^{-1} and 3.4×10^{9} s^{-1}. The obtained IC rate constants are summarized in Table 2-4, together with the energy differences ΔE between the excited triplet state of the Ir(III) complexes and the $^1\Sigma_g{}^+$, $^1\Delta_g$, and $^3\Sigma_g{}^-$ states of molecular oxygen. Figure 2-22 shows plots of log(k_{ic}) vs the triplet energy (E_{T}) of the Ir(III) complexes. The energy-gap dependence of log($k_{\mathrm{ic}}^{1\Sigma}+k_{\mathrm{ic}}^{1\Delta}$) is consistent with eq 2-17, which predicts that the IC rate increases with decreasing excess energy ΔE. Demas et al. [25] attributed the unexpectedly small k_{q} value of Ir(bpy)$_3{}^{3+}$ to the large charges on the complexes; these charges give tight solvation spheres that retard penetration of O$_2$ to an effective quenching distance. The results in this study suggest that a rational explanation can also be made on the basis of the energy gap dependence of the internal conversion. In contrast with log($k_{\mathrm{ic}}^{1\Sigma}+k_{\mathrm{ic}}^{1\Delta}$), the magnitude of log($k_{\mathrm{ic}}^{3\Sigma}$) exhibits a less clear but opposite ΔE dependence. This result suggests that the contribution of CT quenching cannot be neglected in deactivation of the triplet encounter pair ^{3}(T$_1{}^3\Sigma$).

Table 2-4. Energy difference ΔE (eV) between the T_1 state of Ir(III) complexes and $^1\Sigma_g^+$, $^1\Delta_g$, and $^3\Sigma_g^-$ states of molecular oxygen, and the internal conversion rate constants ($k_{ic}^{^1\Sigma} + k_{ic}^{^1\Delta}$ and $k_{ic}^{^3\Sigma}$) of Ir(III) complex/O_2 systems in CH_3CN.

Ir(III) complex	$\Delta E(T_1, {}^1\Sigma_g^+)$	$\Delta E(T_1, {}^1\Delta_g)$	$k_{ic}^{^1\Sigma} + k_{ic}^{^1\Delta}$ /10^{10} s^{-1}	$\Delta E(T_1, {}^3\Sigma_g^-)$	$k_{ic}^{^3\Sigma}$ /10^8 s^{-1}
$(btph)_2Ir(acac)$	+0.13	+0.78	3.5	+1.76	2.0
$(btq)_2Ir(phen\text{-}NH_2)^+$	+0.31	+0.96	2.0	+1.94	10
$(btph)_2Ir(phen\text{-}NH_2)^+$	+0.15	+0.80	1.6	+1.78	3.5
$(btq\text{-}4\text{-}CF_3)_2Ir(phen\text{-}NH_2)^+$	+0.15	+0.80	2.5	+1.78	7.3
$Ir(bpy)_3^{3+}$ [a]	+0.92	+1.57	0.15	+2.55	—
$Ir(bpy)_3^{3+}$ [b]	+0.92	+1.57	0.34	+2.55	—

[a] Ref. [27]. [b] Ref. [25].

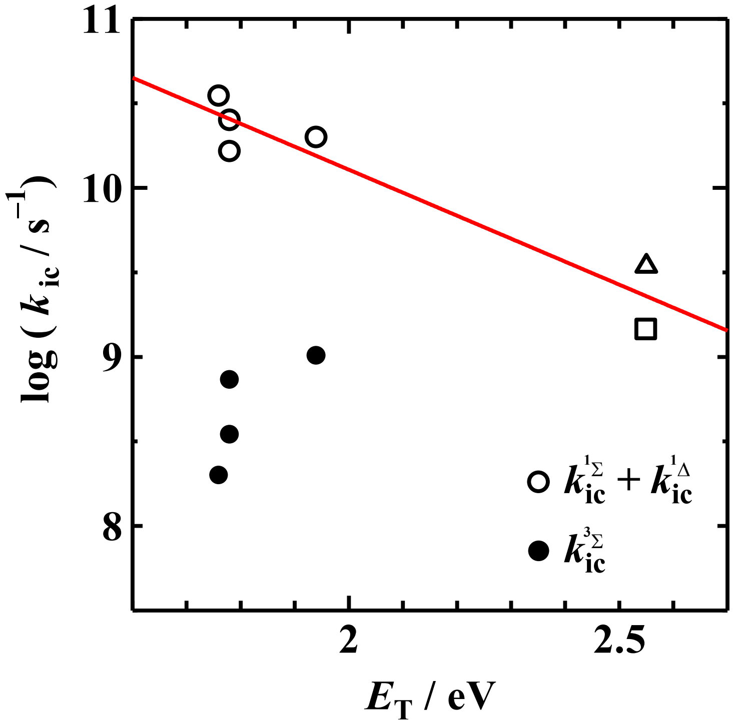

Figure 2-22. Plots of log($k_{ic}^{1\Sigma} + k_{ic}^{1\Delta}$) (open circle) and log($k_{ic}^{3\Sigma}$) (closed circle) vs triplet energy (E_T) of (btph)$_2$Ir(acac), (btq)$_2$Ir(phen-NH$_2$)$^+$, (btph)$_2$Ir(phen-NH$_2$)$^+$, and (btq-4-CF$_3$)$_2$Ir(phen-NH$_2$)$^+$. The open-square and open-triangle symbols denote log^1k_D calculated for Ir(bpy)$_3^{3+}$ using the data in refs. [27] and [25], respectively.

2-3-4 Comparison with Phosphorescence Quenching of Ru(II) Complexes by Molecular Oxygen

Ru(II) complexes have a similar electronic structure with the Ir(III) complexes, i.e., d^6 electronic structure. Hence, the comparison of the electronic interactions of Ru(II) and Ir(III) complexes with molecular oxygen is of great interest. Abdel-Shafi et al. have reported the phosphorescence quenching of some Ru(II) complexes by molecular oxygen and photosensitized generation of singlet oxygen [27,58−61]. Most of the Ru(II) complexes studied so far are cationic, and the Gibbs energy changes for electron transfer reactions with molecular oxygen are slightly negative or positive ($-0.20 < \Delta G_{\mathrm{el}} < 0.20$ eV) as shown in Figure 2-23. As a result, Ru(II) complex/O_2 systems exhibit much smaller k_{q} values compared with the Ir(III) complexes with $\Delta G_{\mathrm{el}} \lesssim -0.50$ eV; the deactivation of encounter complexes of Ru(II) complex/O_2 systems in the excited state is considered to be mainly due to internal conversion and the contribution of CT processes to phosphorescence quenching will be negligibly small. As can be seen from Figure 2-23, the ΔG_{el} and k_{q} values of Ir(III) complexes extend over a much wider range as compared with those of Ru(II) complexes. Since the Ir(III) complexes with a negatively large ΔG_{el} can act as a strong reducing agent in the excited triplet state, they are favorable for photoredox catalyst.

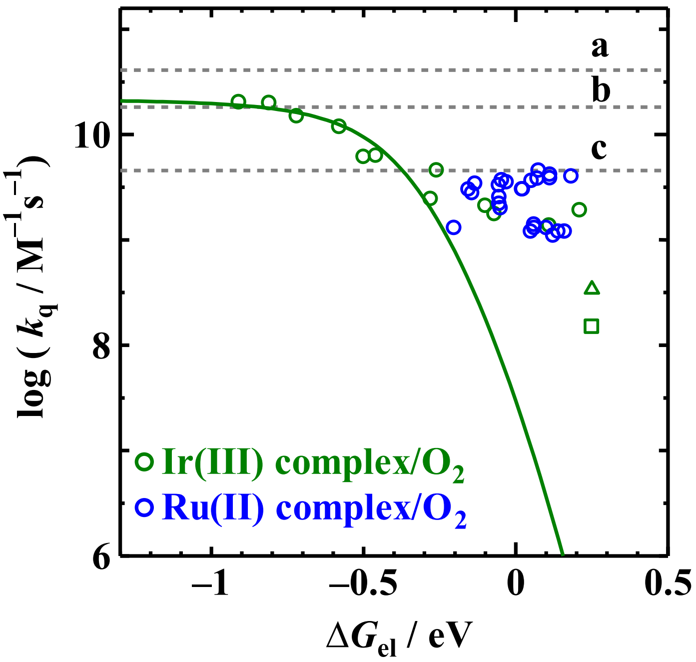

Figure 2-23. Rehm-Weller plots of logk_q vs ΔG_{el} for Ir(III) and Ru(II) complexes/O_2 systems (green circle and blue circle, respectively) [27,58−61]. The dotted lines show (a) logk_d, (b) log(4/9k_d), and (c) log(1/9k_d).

2-3-5 Application of Ir(III) Complexes to Biological Oxygen Probes

As described in Chapter 1, Ir(III) complexes are useful as a biological oxygen probe, because their phosphorescence intensity and lifetime vary significantly depending on the ambient oxygen concentration [2,9−13]. Not only measurements of intracellular oxygen levels but also the tissue oxygen status of a specific organ can be evaluated by measuring the phosphorescence lifetime of Ir(III) complexes delivered into biological targets. A rational design is desired for the development of optimum probes for intracellular and tissue oxygen measurements. One of the most important photophysical properties required for biological oxygen probes is a good sensitivity to oxygen. The oxygen sensitivity can be evaluated by the Stern–Volmer constant (K_{sv}) which is the product of the phosphorescence quenching rate constant (k_q) by molecular oxygen and the intrinsic lifetime (τ_p^0) of the excited triplet Ir(III) complexes. As shown in Table 2-3 in Section 2-3-3, the Ir(III) complex/O_2 systems with a negatively-large ΔG_{el} value give a larger K_{sv} because of the contribution of CT quenching. These complexes tend to give lower f_Δ values, i.e., lower singlet-oxygen production yields, which is favorable for decreasing damage to biological targets.

In order to use Ir(III) complexes as biological oxygen probes, the phosphorescence quenching by endogenous biological substances other than molecular oxygen must be avoided. The results of the present study show that electron transfer quenching is possible if excited triplet Ir(III) complexes interact with biological substances with electron-accepting ability being equal to or higher than molecular oxygen. For example, riboflavin and ubiquinone-10 have relatively-high electron-accepting ability (E_{red} = −0.80 V [62] and −0.602 V [63] vs SCE in CH_3CN, respectively). Although the possibility of electron transfer quenching will depend on the localization of probe complexes in living cells and the concentration of quenchers, consideration of the contribution of electron transfer quenching due to biological substances will be necessary. To avoid electron transfer reactions between Ir(III) complexes and endogenous biological substances, Ir(III) complexes with higher oxidation potentials and lower triplet energies are favorable as biological oxygen probes. Although the cationic Ir(III) complexes, $(btq)_2Ir(phen\text{-}NH_2)^+$, $(btph)_2Ir(phen\text{-}NH_2)^+$, and $(btq\text{-}4\text{-}CF_3)_2Ir(phen\text{-}NH_2)^+$ have relatively-low oxygen sensitivities among the compounds listed in Table 2-3, these complexes show the NIR phosphorescence, which is beneficial for tissue oxygen measurements; in addition, these complexes exhibit lower electron-transfer reactivities, which inhibits electron transfer quenching by biological substances.

2-4 Conclusions

Using a series of neutral and cationic Ir(III) complexes with different oxidation potentials and triplet energies, the relationship between the phosphorescence quenching rate constant (k_q) and the Gibbs energy change (ΔG_{el}) of electron transfer for the Ir(III) complex/AEAs (DNB, NB, and DCB) and Ir(III) complex/O_2 systems were elucidated. Electron transfer reactions between Ir(III) complexes and AEAs were confirmed by the transient absorption spectra of the product radical ions. The separation yields of the radical ion pair in Ir(III) complex/DNB systems were observed to be 0.10–0.17. The significantly small separation yields were attributable to efficient recombination reaction in the radical ion pair, which might originate from heavy-atom effects of the central Ir(III) ion. For the Ir(III) complex/O_2 systems with $\Delta G_{el} \lesssim -0.2$ eV, the $\log k_q$ exhibited a similar ΔG_{el} dependence as the Ir(III) complex/AEA systems, suggesting the contribution of electron transfer. However, in these systems, the k_q values were slightly smaller than those of the AEA systems, and the transient absorption arising from the radical cation product was not observed in the $(ppy)_2Ir(acac)/O_2$ system with $\Delta G_{el} = -0.81$ eV. These results suggested that the phosphorescence quenching of Ir(III) complexes by molecular oxygen occurs through a CT channel with a relatively-large reorganization energy arising from the small molecular size of O_2. The ΔG_{el} dependences of k_q and f_Δ (the efficiency of singlet-oxygen production from triplet states quenched by molecular oxygen) suggested that the phosphorescence quenching of Ir(III) complexes by molecular oxygen proceeds by two competing pathways: an nCT channel, where the rate conforms to the energy-gap law, and a CT channel, where the rate is dominated by ΔG_{el}. The diffusion-controlled rate constant (k_d) for the Ir(III) complex/O_2 systems was calculated to be 4.1×10^{10} $M^{-1}s^{-1}$.

For the systems with $\Delta G_{\mathrm{el}} \lesssim -0.8$ eV, the limiting k_{q} value was 2.5×10^{10} $\mathrm{M}^{-1}\mathrm{s}^{-1}$, which is somewhat larger than $(4/9)k_{\mathrm{d}}$, and the f_{Δ} values were greater than 0.25, suggesting the involvement of singlet-oxygen formation through the triplet or quintet CT complex. For the systems with $\Delta G_{\mathrm{el}} \gtrsim -0.2$ eV, the k_{q} values were less than $(1/9)k_{\mathrm{d}}$ and the f_{Δ} values were close to unity (0.82–0.97). These results demonstrate that the nCT channels through the singlet encounter complex are the main deactivation route.

References

[1] Nazeeruddin, Md. K.; Humphry-Baker, R.; Berner, D.; Rivier, S.; Zuppiroli, L.; Graetzel, M. *J. Am. Chem. Soc.* **2003**, *125*, 8790−8797.

[2] Zhang, S.; Hosaka, M.; Yoshihara, T.; Negishi, K.; Iida, Y.; Tobita, S.; Takeuchi, T. *Cancer Res*. **2010**, *70*, 4490−4498.

[3] Zhao, Q.; Yu, M.; Shi, L.; Liu, S.; Li, C.; Shi, M.; Zhou, Z.; Huang, C.; Li, F. *Organometallics* **2010**, *29*, 1085−1091.

[4] Baldo, M. A.; Lamansky, S.; Burrows, P. E.; Thompson, M. E.; Forrest, S. R. *Appl. Phys. Lett.* **1999**, *75*, 4−6.

[5] Adachi, C.; Baldo, M. A.; Thompson, M. E.; Forrest, S. R. *J. Appl. Phys.* **2001**, *90*, 5048−5051.

[6] Prier, C. K.; Rankic, D. A.; MacMillan, D. W. C. *Chem. Rev.* **2013**, *113*, 5322-5363.

[7] Takizawa, S.; Pérez-Bolívar, C.; Anzenbacher, P. Jr.; Murata, S. *Eur. J. Inorg. Chem.* **2012**, 3975−3979.

[8] Telitel, S.; Dumur, F.; Telitel, S.; Soppera, O.; Lepeltier, M.; Guillaneuf, Y.; Poly, J.; Morlet-Savary, F.; Fioux, P.; Fouassier, J.-P.; Gigmes, D.; Lalevée, J. *Polym. Chem.* **2015**, *6*, 613−624.

[9] Yoshihara, T.; Yamaguchi, Y.; Hosaka, M.; Takeuchi, T.; Tobita, S. *Angew. Chem. Int. Ed.* **2012**, *51*, 4148−4151.

[10] Murase, T.; Yoshihara, T.; Tobita, S. *Chem. Lett*. **2012**, *41*, 262−263.

[11] Yoshihara, T.; Hosaka, M.; Terata, M.; Ichikawa, K.; Murayama, S.; Tanaka, A.; Mori, M.; Itabashi, H.; Takeuchi, T.; Tobita, S. *Anal. Chem*. **2015**, *87*, 2710−2717.

[12] Yoshihara, T.; Murayama, S.; Masuda, T.; Kikuchi, T.; Yoshida, K.; Hosaka, M.;

Tobita, S. *J. Photochem. Photobiol. A: Chem.* **2015**, *299*, 172−182.

[13] Hirakawa, Y.; Yoshihara, T.; Kamiya, M.; Mimura, I.; Fujikura, D.; Masuda, T.; Kikuchi, R.; Takahashi, I.; Urano, Y.; Tobita, S.; Nangaku, M. *Sci. Rep.* **2015**, *5*, 1−10.

[14] Darmanyan, A. P.; Lee, W.; Jenks, W. S. *J. Phys. Chem. A* **1999**, *103*, 2705−2711.

[15] Schmidt, R. *Photochem. Photobiol.* **2006**, *82*, 1161−1177.

[16] Wilkinson F.; Abdel-Shafi, A. A. *J. Phys. Chem. A* **1997**, *101*, 5509−5516.

[17] Schmidt, R.; Shafii, F. *J. Phys. Chem. A* **2001**, *105*, 8871−8877.

[18] Schmidt, R.; Shafii, F.; Schweitzer, C.; Abdel-Shafi A. A.; Wilkinson, F. *J. Phys. Chem. A* **2001**, *105*, 1811−1817.

[19] Schweitzer, C.; Mehrdad, Z.; Shafii, F.; Schmidt, R. *J. Phys. Chem. A* **2001**, *105*, 5309−5316.

[20] Wilkinson, F.; McGarvey, D. J.; Olea, A. F. *J. Am. Chem. Soc.* **1993**, *115*, 12144−12151.

[21] Schweitzer, C.; Mehrdad, Z.; Noll, A.; Grabner, E.-W.; Schmidt, R. *Helv. Chim. Acta.* **2001**, *84*, 2493−2507.

[22] Gijzeman, O. L. J.; Kaufman, F.; Porter, G. *J. Chem. Soc. Faraday Trans. 2* **1973**, *69*, 708−726.

[23] Garner, A.; Wilkinson, F. *Chem. Phys. Lett.* **1977**, *45*, 432−435.

[24] Demas, J. N.; Harris, E. W.; Flynn, C. M. Jr.; Diemente, D. *J. Am. Chem. Soc.* **1975**, *97*, 3838−3839.

[25] Demas, J. N.; Harris, E. W.; McBride, R. P. *J. Am. Chem. Soc.* **1977**, *99*, 3547−3551.

[26] Gao, R.; Ho, D. G.; Hernandez, B.; Selke, M.; Murphy, D.; Djurovich, P. I.; Thompson, M. E. *J. Am. Chem. Soc.* **2002**, *124*, 14828−14829.

[27] Abdel-Shafi, A. A.; Bourdelande, J. L.; Ali, S. S. *Dalton Trans.* **2007**, 2510−2516.

[28] Djurovich, P. I.; Murphy, D.; Thompson, M. E.; Hernandez, B.; Gao, R.; Hunt, P. L.; Selke, M. *Dalton Trans.* **2007**, 3763−3770.

[29] Takizawa, S.; Aboshi, R.; Murata, S. *Photochem. Photobiol. Sci.* **2011**, *10*, 895−903.

[30] Ashen-Garry, D.; Selke, M. *Photochem. Photobiol.* **2014**, *90*, 257−274.

[31] Ruggi, A.; Mauro, M.; Polo, F.; Reinhoudt, D. N.; Cola, L. D.; Velders A. H. *Eur. J. Inorg. Chem.* **2012**, 1025−1037.

[32] Lamansky, S.; Djurovich, P.; Murphy, D.; Abdel-Razzaq, F.; Kwong, R.; Tsyba, I.; Bortz, M.; Mui, B.; Bau, R.; Thompson, M. E. *Inorg. Chem.* **2001**, *40*, 1704−1711.

[33] Jung, K. M.; Kim, K. H.; Jin, J.-I.; Cho, M. J.; Choi, D. H. J. Polym. Sci. Part A: Polym. Chem. 2008, 46, 7517−7533.

[34] Hasebe, N.; Suzuki, K.; Horiuchi, H.; Suzuki, H.; Yoshihara, T.; Okutsu, T.; Tobita, S. *Anal. Chem.* **2015**, *87*, 2360−2366.

[35] Schmidt, R.; Tanielian, C.; Dunsbach, R.; Wolff, C. *J. Photochem. Photobiol. A: Chem.* **1994**, *79*, 11−17.

[36] Yersin, H.; Rausch, A. F.; Czerwieniec, R.; Hofbeck, T.; Fischer, T. *Coord. Chem. Rev.* **2011**, *255*, 2622−2652.

[37] Montalti, M.; Credi, A.; Prodi, L.; Gandolfi, M. T. *Handbook of Photochemistry, 3rd Ed.*; CRC Press: Boca Raton, 2005.

[38] Agmon, N.; Levine, R. D. *Chem. Phys. Lett.* **1977**, *52*, 197−201.

[39] Balzani, V.; Bolletta, F.; Scandola, F. *J. Am. Chem. Soc.* **1980**, *102*, 2152−2163.

[40] Rehm, D.; Weller, A. *Isr. J. Chem.* **1970**, *8*, 259−271.

[41] King, K. A.; Spellane, P. J.; Watts, R. J. *J. Am. Chem. Soc.* **1985**, *107*, 1431−1432.

[42] Shida, T. *Electronic Absorption Spectra of Radical Ions.*; Elsevier: Amsterdam, 1988.

[43] Sauer, A.; Wasgestian F.; Nickel, U. *Bull. Chem. Soc. Jpn.* **1989**, *62*, 2688−2692.

[44] Endo, A.; Suzuki, K.; Yoshihara, T.; Tobita, S.; Yahiro, M.; Adachi, C. *Chem. Phys. Lett.* **2008**, *460*, 155−157.

[45] Olmsted, J. III; Meyer, T. J. *J. Phys. Chem.* **1987**, *91*, 1649−1655.

[46] Abdel-Shafi, A. A.; Wilkinson, F. *J. Phys. Chem. A* **2000**, *104*, 5747−5757.

[47] Alwattar, A. H.; Lumb, M. D.; Birks, J. B. In *Organic Molecular Photophysics*; Birks, J. B., Ed.; Wiley: New York, 1973; Vol. 1, p. 403.

[48] Lü, J.-M.; Rosokha, S. V.; Lindeman, S. V.; Neretin, I. S.; Kochi, J. K. *J. Am. Chem. Soc.* **2005**, *127*, 1797−1809.

[49] Macías-Ruvalcaba, N. A.; Evans, D. H. *J. Phys. Chem. B* **2005**, *109*, 14642−14647.

[50] Reid, E. F.; Burn, P. L.; Lo, S.-C.; Hogan, C. F. *Electrochimica Acta.* **2013**, *100*, 72−77.

[51] Tsushima, M.; Tokuda, K.; Ohsaka, T. *Anal. Chem.* **1994**, *66*, 4551−4556.

[52] Bondi, A. van der Waals Volumes and Radii. *J. Phys. Chem.* **1964**, *68*, 441−451.

[53] Grewer, C.; Brauer, H.-D. *J. Phys. Chem.* **1993**, *97*, 5001−5006.

[54] Tsubomura, H.; Mulliken, R. S. *J. Am. Chem. Soc.* **1960**, *82*, 5966−5974.

[55] Minaev, B. F.; Kukueva, V. V.; Ågren, H. *J. Chem. Soc. Faraday Trans.* **1994**, *90*, 1479−1486.

[56] Eigen, M. *Z. Phys. Chem. N.F.* **1954**, *1*, 176−200.

[57] Kawaoka, K.; Khan, A. U.; Kearns, D. R. *J. Chem. Phys.* **1967**, *46*, 1842−1853.

[58] Abdel-Shafi, A. A.; Beer, P. D.; Mortimer, R. J.; Wilkinson, F. *Phys. Chem. Chem. Phys.* **2000**, *2*, 3137−3144.

[59] Abdel-Shafi, A. A.; Beer, P. D.; Mortimer, R. J.; Wilkinson, F. *J. Phys. Chem. A.* **2000**, *104*, 192−202.

[60] Abdel-Shafi, A. A.; Beer, P. D.; Mortimer, R. J.; Wilkinson, F. *Helev. Chim. Acta.* **2001**, *84*, 2784−2795.

[61] Abdel-Shafi, A. A.; Worral, D. R.; Ershov, A. Y. *Dalton Trans.* **2004**, 30−36.

[62] Porcal, G.; Bertolotti, S. G.; Previtali, C. M.; Encinas, M. V. *Phys. Chem. Chem. Phys.* **2003**, *5*, 4123−4128.

[63] Prince, R. C.; Dutton, P. L.; Bruce, J. M. *FEBS Lett.* **1983**, *160*, 273−276.

Appendix 2-1 Kinetics of Photoinduced Electron-Transfer Reaction

The reaction sequence of photoinduced electron-transfer reactions from the excited donor molecules (D*) to the electron acceptors (A) can be expressed as.

$$\mathbf{^3D^* + A \underset{\mathit{k}_{-d}}{\overset{\mathit{k}_d}{\rightleftarrows}} (^3D^{*}\cdots A) \underset{\mathit{k}_{-el}}{\overset{\mathit{k}_{el}}{\rightleftarrows}} (D^{\cdot +}\cdots A^{\cdot -}) \xrightarrow{\mathit{k}_s} D^{\cdot +} + A^{\cdot -}}$$

Scheme A-1

where $(\mathrm{D}^{*}\ldots\mathrm{A})$, $(\mathrm{D}^{\bullet+}\ldots\mathrm{A}^{\bullet-})$, and $\mathrm{D}^{\bullet+}+\mathrm{A}^{\bullet-}$ are the encounter complex, the radical ion pair, and the free radical ions, k_{d} and $k_{-\mathrm{d}}$ are the diffusion rate constant and the dissociation rate constant, k_{el} and $k_{-\mathrm{el}}$ are the electron transfer and back electron-transfer rate constants, and k_{s} is the separation rate constant, respectively.

By applying the steady-state approximation for the encounter complex and radical ion pair (eqs A-1 and A-2), eq A-3 can be derived.

$$\frac{\mathrm{d}[(\mathrm{D}^{*}\ldots\mathrm{A})]}{\mathrm{dt}} = k_{\mathrm{d}}[\mathrm{D}^{*}][\mathrm{A}] - (k_{-\mathrm{d}} + k_{\mathrm{el}})[(\mathrm{D}^{*}\ldots\mathrm{A})] + k_{-\mathrm{el}}[(\mathrm{D}^{*}\ldots\mathrm{A})] = 0 \qquad \text{(A-1)}$$

$$\frac{\mathrm{d}[(\mathrm{D}^{\bullet+}\ldots\mathrm{A}^{\bullet-})]}{\mathrm{dt}} = k_{\mathrm{el}}[(\mathrm{D}^{*}\ldots\mathrm{A})] - (k_{-\mathrm{el}} + k_{\mathrm{s}})[(\mathrm{D}^{\bullet+}\ldots\mathrm{A}^{\bullet-})] = 0 \qquad \text{(A-2) and}$$

$$[(\mathrm{D}^{*}\ldots\mathrm{A})] = \frac{(k_{-\mathrm{el}} + k_{\mathrm{s}})}{k_{\mathrm{el}}}[(\mathrm{D}^{\bullet+}\ldots\mathrm{A}^{\bullet-})] \qquad \text{(A-3).}$$

By substituting eq A-3 into eq A-1, the following equations are obtained,

$$k_{\mathrm{d}}[\mathrm{D}^{*}][\mathrm{A}] - \left\{\frac{(k_{-\mathrm{d}} + k_{\mathrm{el}})(k_{-\mathrm{el}} + k_{\mathrm{s}})}{k_{\mathrm{el}}} - k_{-\mathrm{el}}\right\}[(\mathrm{D}^{\bullet+}\ldots\mathrm{A}^{\bullet-})] = 0 \qquad \text{(A-4) and}$$

$$k_{\mathrm{d}}[\mathrm{D}^{*}][\mathrm{A}] = \left(\frac{k_{-\mathrm{d}}k_{-\mathrm{el}} + k_{-\mathrm{d}}k_{\mathrm{s}} + k_{\mathrm{el}}k_{\mathrm{s}}}{k_{\mathrm{el}}}\right)[(\mathrm{D}^{\bullet+}\ldots\mathrm{A}^{\bullet-})] \qquad \text{(A-5).}$$

On the other hand, quenching follows the following relation

$$k_{\mathrm{q}}[\mathrm{D}^{*}][\mathrm{A}] = k_{\mathrm{s}}[(\mathrm{D}^{\bullet+} \ldots \mathrm{A}^{\bullet-})] \tag{A-6}$$

Hence eqs A-7 and A-8 can be derived from eqs A-5 and A-6,

$$\frac{k_{\mathrm{d}}k_{\mathrm{s}}}{k_{\mathrm{q}}}[(\mathrm{D}^{\bullet+} \ldots \mathrm{A}^{\bullet-})] = \left(\frac{k_{-\mathrm{d}}k_{-\mathrm{el}} + k_{-\mathrm{d}}k_{\mathrm{s}} + k_{\mathrm{el}}k_{\mathrm{s}}}{k_{\mathrm{el}}}\right)[(\mathrm{D}^{\bullet+} \ldots \mathrm{A}^{\bullet-})] \quad \text{(A-7) and}$$

$$k_{\mathrm{q}} = \frac{k_{\mathrm{d}}k_{\mathrm{el}}k_{\mathrm{s}}}{k_{-\mathrm{d}}k_{-\mathrm{el}} + k_{-\mathrm{d}}k_{\mathrm{s}} + k_{\mathrm{el}}k_{\mathrm{s}}} = \frac{k_{\mathrm{d}}}{1 + \dfrac{k_{-\mathrm{d}}}{k_{\mathrm{el}}}\left(1 + \dfrac{k_{-\mathrm{el}}}{k_{\mathrm{s}}}\right)} \tag{A-8}$$

Appendix 2-2 Kinetics for the Quenching of the Excited Triplet Molecule by Molecular Oxygen

Proposed mechanism for quenching of the excited triplet molecules by molecular oxygen is shown in Scheme B-1.

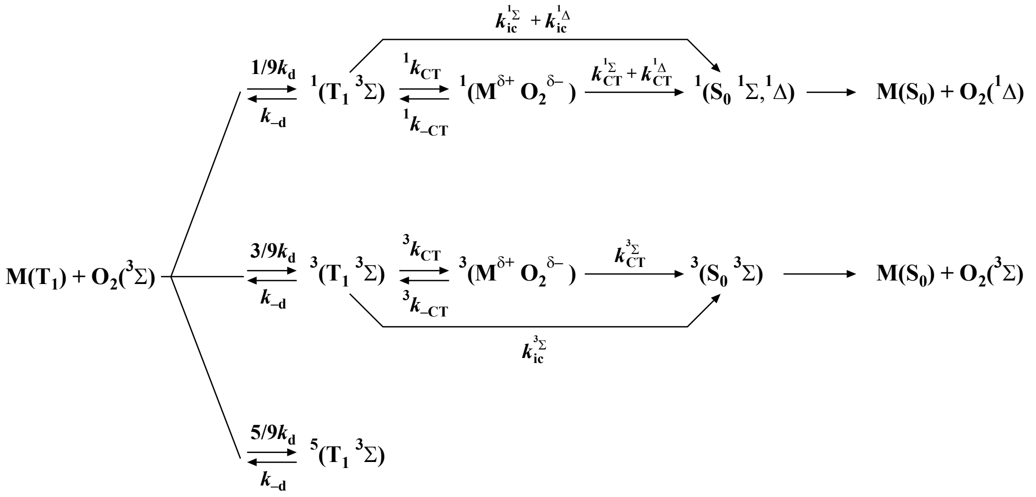

Scheme B-1

where $^m(T_1\,^3\Sigma)$ and $^m(M^{\delta+}\,O_2^{\delta-})$ are the encounter and charge transfer complexes (m=1,3, 5), $^1(S_0\,^1\Sigma,^1\Delta)$ and $^3(S_0\,^3\Sigma)$ are the precursor complexes, k_d and k_{-d} are the diffusion and dissociation rate constants, and k_{ic} and k_{CT} are the rates of internal conversion and charge transfer, respectively. The CT rate constants ($^mk_{CT}$ (m = 1 and 3)) of the complexes with $\Delta G_{el} \lesssim -0.1$ eV are evaluated to be much larger than the reverse CT rate constants ($^mk_{-CT}$ (m = 1 and 3)) from the relation $^mk_{CT}/^mk_{-CT} = \exp(-\Delta G_{el}/RT)$ for full-electron transfer at 298K. Hence, $^mk_{-CT}$ can be neglected.

According to scheme B-1, eq B-1 is derived,

$$-\frac{d[T_1]}{dt} = k_d[M(T_1)][O_2(^3\Sigma)] - k_{-d}([^1(T_1\,^3\Sigma)] + [^3(T_1\,^3\Sigma)] + [^5(T_1\,^3\Sigma)]) \qquad \text{(B-1).}$$

With the steady-state approximation for $[^1(T_1\,^3\Sigma)]$, $[^3(T_1\,^3\Sigma)]$, and $[^5(T_1\,^3\Sigma)]$,

$$\frac{\mathrm{d}[{}^{1}(\mathrm{T}_1\,{}^{3}\Sigma)]}{\mathrm{dt}}=\frac{1}{9}k_{\mathrm{d}}[\mathrm{M(T_1)}][\mathrm{O_2}({}^{3}\Sigma)]-(k_{-\mathrm{d}}+k_{\mathrm{ic}}^{1\Sigma}+k_{\mathrm{ic}}^{1\Delta}+{}^{1}k_{\mathrm{CT}})[{}^{1}(\mathrm{T}_1\,{}^{3}\Sigma)]=0 \qquad \text{(B-2),}$$

$$\frac{\mathrm{d}[{}^{3}(\mathrm{T}_1\,{}^{3}\Sigma)]}{\mathrm{dt}}=\frac{3}{9}k_{\mathrm{d}}[\mathrm{M(T_1)}][\mathrm{O_2}({}^{3}\Sigma)]-(k_{-\mathrm{d}}+k_{\mathrm{ic}}^{3\Sigma}+{}^{3}k_{\mathrm{CT}})[{}^{3}(\mathrm{T}_1\,{}^{3}\Sigma)]=0 \qquad \text{(B-3), and}$$

$$\frac{\mathrm{d}[{}^{5}(\mathrm{T}_1\,{}^{3}\Sigma)]}{\mathrm{dt}}=\frac{5}{9}k_{\mathrm{d}}[\mathrm{M(T_1)}][\mathrm{O_2}({}^{3}\Sigma)]-k_{-\mathrm{d}}[{}^{5}(\mathrm{T}_1\,{}^{3}\Sigma)]=0 \qquad \text{(B-4).}$$

Eqs B-5, B-6, and B-7 are derived from eqs B-2, B-3, and B-4,

$$[{}^{1}(\mathrm{T}_1\,{}^{3}\Sigma)]=\frac{1}{9}\frac{k_{\mathrm{d}}}{k_{-\mathrm{d}}+k_{\mathrm{ic}}^{1\Sigma}+k_{\mathrm{ic}}^{1\Delta}+{}^{1}k_{\mathrm{CT}}}[\mathrm{M(T_1)}][\mathrm{O_2}({}^{3}\Sigma)] \qquad \text{(B-5),}$$

$$[{}^{3}(\mathrm{T}_1\,{}^{3}\Sigma)]=\frac{3}{9}\frac{k_{\mathrm{d}}}{k_{-\mathrm{d}}+k_{\mathrm{ic}}^{3\Sigma}+{}^{3}k_{\mathrm{CT}}}[\mathrm{M(T_1)}][\mathrm{O_2}({}^{3}\Sigma)] \qquad \text{(B-6), and}$$

$$[{}^{5}(\mathrm{T}_1\,{}^{3}\Sigma)]=\frac{5}{9}\frac{k_{\mathrm{d}}}{k_{-\mathrm{d}}}[\mathrm{M(T_1)}][\mathrm{O_2}({}^{3}\Sigma)] \qquad \text{(B-7).}$$

By substituting eqs B-5, B-6, and B-7 into eq B-1, eq B-8 is obtained

$$\begin{aligned}
-\frac{\mathrm{d}[\mathrm{T_1}]}{\mathrm{dt}}&=k_{\mathrm{d}}[\mathrm{M(T_1)}][\mathrm{O_2}({}^{3}\Sigma)]-\frac{1}{9}\frac{k_{\mathrm{d}}k_{-\mathrm{d}}}{k_{-\mathrm{d}}+k_{\mathrm{ic}}^{1\Sigma}+k_{\mathrm{ic}}^{1\Delta}+{}^{1}k_{\mathrm{CT}}}[\mathrm{M(T_1)}][\mathrm{O_2}({}^{3}\Sigma)]\\
&\quad-\frac{3}{9}\frac{k_{\mathrm{d}}k_{-\mathrm{d}}}{k_{-\mathrm{d}}+k_{\mathrm{ic}}^{3\Sigma}+{}^{3}k_{\mathrm{CT}}}[\mathrm{M(T_1)}][\mathrm{O_2}({}^{3}\Sigma)]-\frac{5}{9}\frac{k_{\mathrm{d}}k_{-\mathrm{d}}}{k_{-\mathrm{d}}}[\mathrm{M(T_1)}][\mathrm{O_2}({}^{3}\Sigma)]\\
&=\frac{4}{9}k_{\mathrm{d}}[\mathrm{M(T_1)}][\mathrm{O_2}({}^{3}\Sigma)]-\frac{1}{9}\frac{k_{\mathrm{d}}k_{-\mathrm{d}}}{k_{-\mathrm{d}}+k_{\mathrm{ic}}^{1\Sigma}+k_{\mathrm{ic}}^{1\Delta}+{}^{1}k_{\mathrm{CT}}}[\mathrm{M(T_1)}][\mathrm{O_2}({}^{3}\Sigma)]\\
&\quad-\frac{3}{9}\frac{k_{\mathrm{d}}k_{-\mathrm{d}}}{k_{-\mathrm{d}}+k_{\mathrm{ic}}^{3\Sigma}+{}^{3}k_{\mathrm{CT}}}[\mathrm{M(T_1)}][\mathrm{O_2}({}^{3}\Sigma)]\\
&=\frac{1}{9}\frac{k_{\mathrm{ic}}^{1\Sigma}+k_{\mathrm{ic}}^{1\Delta}+{}^{1}k_{\mathrm{CT}}}{k_{-\mathrm{d}}+k_{\mathrm{ic}}^{1\Sigma}+k_{\mathrm{ic}}^{1\Delta}+{}^{1}k_{\mathrm{CT}}}[\mathrm{M(T_1)}][\mathrm{O_2}({}^{3}\Sigma)]\\
&\quad+\frac{3}{9}\frac{k_{\mathrm{ic}}^{3\Sigma}+{}^{3}k_{\mathrm{CT}}}{k_{-\mathrm{d}}+k_{\mathrm{ic}}^{3\Sigma}+{}^{3}k_{\mathrm{CT}}}[\mathrm{M(T_1)}][\mathrm{O_2}({}^{3}\Sigma)]
\end{aligned} \qquad \text{(B-8).}$$

Therefore, the quenching rate constant (k_q) is shown as the following equation,

$$k_\mathrm{q} = k_\mathrm{d}\left(\frac{1}{9}\frac{k_\mathrm{ic}^{1\Sigma} + k_\mathrm{ic}^{1\Delta} + {}^{1}k_\mathrm{CT}}{k_{-\mathrm{d}} + k_\mathrm{ic}^{1\Sigma} + k_\mathrm{ic}^{1\Delta} + {}^{1}k_\mathrm{CT}} + \frac{1}{3}\frac{k_\mathrm{ic}^{3\Sigma} + {}^{3}k_\mathrm{CT}}{k_{-\mathrm{d}} + k_\mathrm{ic}^{3\Sigma} + {}^{3}k_\mathrm{CT}}\right) \qquad \text{(B-9).}$$

By replacing ${}^{1}k_\mathrm{D}$ and ${}^{3}k_\mathrm{D}$ by $k_\mathrm{ic}^{1\Sigma} + k_\mathrm{ic}^{1\Delta} + {}^{1}k_\mathrm{CT}$ and $k_\mathrm{ic}^{3\Sigma} + {}^{3}k_\mathrm{CT}$, respectively, k_q and the fraction (f_Δ) leading to formation of ${}^{1}\mathrm{O}_2$ in the oxygen quenching of the excited triplet molecules are given by eqs B-10 and B-11, respectively.

$$k_\mathrm{q} = k_\mathrm{d}\left(\frac{1}{9}\frac{{}^{1}k_\mathrm{D}}{k_{-\mathrm{d}} + {}^{1}k_\mathrm{D}} + \frac{1}{3}\frac{{}^{3}k_\mathrm{D}}{k_{-\mathrm{d}} + {}^{3}k_\mathrm{D}}\right) \qquad \text{(B-10) and}$$

$$f_\Delta = \frac{k_\mathrm{d}}{9}\left(\frac{{}^{1}k_\mathrm{D}}{k_{-\mathrm{d}} + {}^{1}k_\mathrm{D}}\right)\frac{1}{k_\mathrm{q}} \qquad \text{(B-11).}$$

Chapter 3

Absolute Phosphorescence Quantum Yields of Singlet Molecular Oxygen in Solution Determined Using an Integrating Sphere Instrument

3-1 Introduction

In Chapter 2, it was shown that singlet oxygen ($O_2(a^1\Delta_g)$) is produced in the phosphorescence quenching of the excited triplet Ir(III) complexes by molecular oxygen. As described in Chapter 1, singlet oxygen is one of the reactive oxygen species and plays an important role in various photochemical and biological processes [1−3]. Therefore, it is important to clarify the photophysical properties of $O_2(a^1\Delta_g)$ produced under the presence of transition metal complexes.

The photoluminescence quantum yield (Φ_{PL}) is one of the most important photophysical quantities of a molecule because it allows the emission capacity of luminescent molecules to be assessed and it enables the rate constants of various relaxation processes from the excited states to be determined in combination with other lifetime data [4−6]. To date, various methods to determine the Φ_{PL} have been developed [7−9]. The conventional relative (or secondary) method, which is currently the most widely used method, requires a standard substance for which Φ_{PL} has been accurately determined. The relative method also requires corrections for the refractive index of solvent when different solvents are used as standard and sample solutions. On the other hand, Vavilov [10] reported an absolute method in which a solid scatterer (magnesium oxide) is used to absolutely calibrate the detector/excitation system. This method does not require a standard solution, but requires various complex corrections in order to obtain accurate quantum yields [11].

As an alternative method, the absolute method using an integrating sphere has recently been developed as a method that does not require a standard substance or complex corrections [12−20]. The integrating sphere can eliminate much optical anisotropy by multiple reflections on the inner surface of the integrating sphere. Suzuki and coworkers have recently designed a new integrating sphere instrument for measuring the absolute emission quantum yield in the visible wavelength region [21−23]. This instrument consisted of a monochromatized Xe lamp, an integrating sphere, and a multichannel analyzer equipped with a back-thinned charge-coupled device (BT-CCD) detector. Excitation photons that are not absorbed by the sample solution and the emitted photons from the sample undergo repeated reflection on the inner surface of the integrating sphere, thus averaging the effects of polarization and refractive index. With this instrument, they measured the absolute fluorescence quantum yields of various common standard solutions and found good agreement between the measured yields and the literature values, thus confirming the reliability of the instrument.

Since NIR light is less invasive to biological cells and tissues compared with the shorter wavelength photons and permits the measurement of deeper tissues when compared to visible light, near-infrared (NIR)-emitting probes have been developed for biological oxygen imaging. To assess the utility of NIR-emitting probes, the emission quantum yield is an essential prerequisite. Recently, an integrating sphere instrument for the measurement of absolute photoluminescence quantum yields in the spectral region from ca. 400 to 1000 nm was designed by Würth et al. [13] This instrument permits measurements of small sample volume in the microliter range, thus allowing analysis of very small biological and bioanalytical samples. Using this instrument, the absolute fluorescence quantum yields of NIR dyes that can be used as standards for the fluorescence quantum yield in the NIR region were determined.

In this study, a new integrating sphere instrument that can be used for the measurement of emission quantum yield in the visible to NIR region ($\lambda = 350-1650$ nm) is developed. Using this system, the absolute measurement of the quantum yield of $a^1\Delta_g$ ($v' = 0$) → $X^3\Sigma_g^-$ ($v'' = 0$) emission which has the peak at around 1270 nm from singlet oxygen was performed for the first time. Although there have been few reports on quantum yield of $O_2(a^1\Delta_g) \rightarrow O_2(X^3\Sigma_g^-)$ emissions, all the measurements reported to date were carried out based on the relative method. In spite of various improvements in the apparatus, detector sensitivity in the NIR region, corrections for spectral response and choice of standard, large scatter is seen for the reported $\Phi_p^{1\Delta}$ values [24]. The present absolute $\Phi_p^{1\Delta}$ measurements were thus performed to confirm the usefulness of absolute quantum yield measurements in the NIR region.

3-2 Experimental Section

3-2-1 Materials

Carbon tetrachloride (CCl_4, spectrophotometric grade, >99.7%; Kanto Chemical), carbon disulfide (CS_2, spectral grade, >99.9%, Kanto Chemical), toluene ($PhCH_3$; spectral grade, >99.8%, Wako Pure Chemical), chlorobenzene (PhCl, >99.0%; Wako Pure Chemical), bromobenzene (PhBr, >98.0%, Kanto Chemical), iodobenzene (PhI, >99.0%, Tokyo Chemical Industries), chloroform ($CHCl_3$, spectrophotometric grade, >99.7%, Kanto Chemical), acetonitrile (CH_3CN, spectrophotometric grade, >99.7%, Kanto Chemical), acetonitrile-d_3 (CD_3CN, NMR grade, Kanto Chemical), ethanol (EtOH, spectral grade, >99.5%, Kishida Chemical), ethanol-d_1 (EtOD, >95.0%, Tokyo Chemical Industries), benzene (C_6H_6, spectral grade, >99.8%, Wako Pure Chemical), and benzene-d_6 (C_6D_6, NMR grade, Kanto Chemical) were used as solvent. These solvents were used without further purification. 2-Methyltetrahydrofuran (2-MeTHF, >98.0%, Tokyo Chemical Industries) was purified by distillation. As the singlet oxygen sensitizer, two compounds: perinaphthenone (PN, 97%, Sigma-Aldrich) and platinum(II) meso-tetra(pentafluorophenyl)porphine (PtTFPP, Frontier Scientific) (Figure 3-1) were used. PN has already been established as a singlet oxygen sensitizer [25], although the excitation wavelength is limited to below ~410 nm. In several solvents employed in the present study (CS_2, PhCl, PhBr, and PhI), absorption of solvent was not negligible at excitation wavelengths <410 nm; therefore, PtTFPP which can be used for excitation at longer wavelengths (525 nm) was used [26]. PN was purified by column chromatography using chloroform/ethyl acetate (99:1, v/v) as an eluent. PtTFPP was used as received, after confirming the purity by thin-layer chromatography.

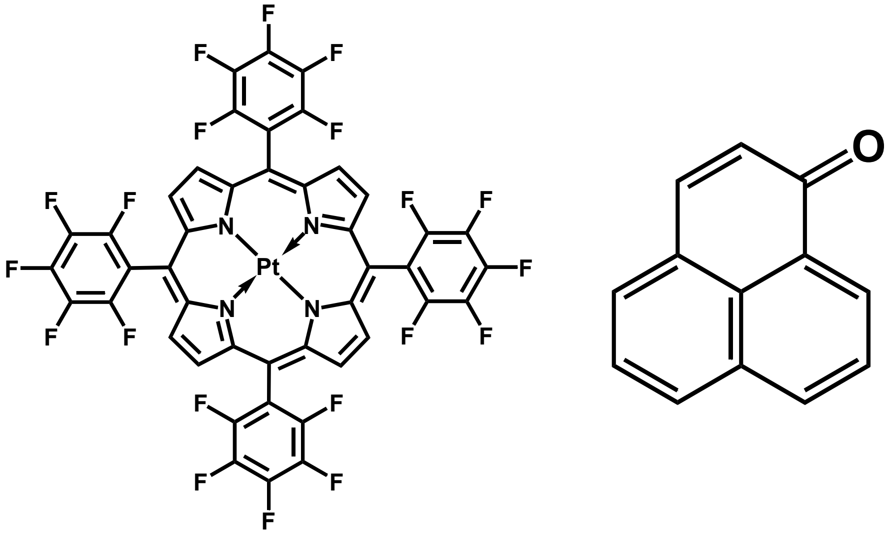

PtTFPP PN

Figure 3-1. Chemical structures of platinum(II) meso-tetra(pentafluorophenyl)porphine (PtTFPP) and perinaphthenone (PN).

3-2-2 Absorption and Emission Spectra

Absorption and emission spectra were recorded using the instruments described in Section 2-2-2.

3-2-3 Emission Quantum Yield of Near-infrared (NIR) Emission

Absolute Method

The emission quantum yield measurement of the $a^1\Delta_g$ ($v' = 0$) → $X^3\Sigma_g^-$ ($v'' = 0$) transition of singlet oxygen ($\Phi_p^{1\Delta}$) was carried out on an absolute photoluminescence quantum yield measurement system which was newly constructed in Hamamatsu Photonics K.K. The schematic diagram of this system is shown in Figure 3-2. This instrument consisted of a 150 W Xe arc lamp (Hamamatsu, L9588-04) as the excitation light source, an integrating sphere, two multichannel analyzers, and a personal computer. A quartz cell with an optical path length of 1 cm was set into the integrating sphere. Excitation light was introduced into the integrating sphere to irradiate the sample. A band-pass filter (center wavelength 525 nm, full width at half-maximum (fwhm) 50 nm) and an IR absorbing filter were placed between the Xe light source and the integrating sphere in order to select excitation wavelengths. To avoid direct detection of the introduced excitation light and/or emission from the sample, the integrating sphere with an inner diameter of ca. 84 mm had a baffle between the sample and detection exit positions. Spectralon was fitted in the inner surface of the integrating sphere as a reflecting material; this provided a high reflectance of 99% between 350 and 1650 nm. Two different photonic multichannel analyzers (Hamamatsu, C10027-02 and C10028-01) were used to detect excitation and emission spectra between 350 and 1650 nm with good spectral sensitivity.

The former multichannel analyzer (MCA1) uses a BT-CCD with 1024 channels as the detector and has a measurable wavelength range from 350 to 1100 nm (0.73 nm/channel). The latter (MCA2) employs an InGaAs linear image sensor with 256 photosensitive channels and can be used for measurements between 900 and 1650 nm (2.9 nm/channel). These systems were completely calibrated for sensitivity of the spectral region from 350 to 1650 nm using deuterium and halogen standard light sources. These standard light sources were calibrated in accordance with measurement standards traceable to primary standards (national standards) located at the National Metrology Institute of Japan. The primary measurement standards are based on physical units of measurement according to the International System of Units (SI). The photoluminescence quantum yield (Φ_{PL}) can be derived from the following equation

$$\Phi_{\mathrm{PL}} = \frac{N(\mathrm{Em})}{N(\mathrm{Abs})} = \frac{\int \frac{\lambda}{hc}\left[I_{\mathrm{em}}^{\mathrm{sample}}(\lambda) - I_{\mathrm{em}}^{\mathrm{reference}}(\lambda)\right] d\lambda}{\int \frac{\lambda}{hc}\left[I_{\mathrm{ex}}^{\mathrm{reference}}(\lambda) - I_{\mathrm{ex}}^{\mathrm{sample}}(\lambda)\right] d\lambda} \tag{3-1}$$

where *N*(Abs) denotes the number of photons absorbed by a sample, *N*(Em) stands for the number of photons emitted from a sample, λ, h, and c are the wavelength, Planck's constant, and the velocity of light, respectively, $I_{\mathrm{ex}}^{\mathrm{sample}}$ and $I_{\mathrm{ex}}^{\mathrm{reference}}$ are the integrated intensities of the excitation light in the presence and absence of a sample, respectively, and $I_{\mathrm{em}}^{\mathrm{sample}}$ and $I_{\mathrm{em}}^{\mathrm{reference}}$ are the photoluminescence intensities in the presence and absence of a sample, respectively [21].

Relative Method

Figure 3-3 shows the block diagram of the instrument for the quantum yield measurement based on the relative method. The excitation wavelength was selected from the light of 150 W Xe arc lamp (Hamamatsu, L9588-04) by passing through a band-pass filter (center wavelength 525 nm, fwhm 50 nm). The excitation light was focused into a quartz cell with and without sample solution. The emission of singlet oxygen from each solution was recorded on a spectrally calibrated photonic multichannel analyzer (Hamamatsu, C10028-01) equipped with an InGaAs linear image sensor as a detector.

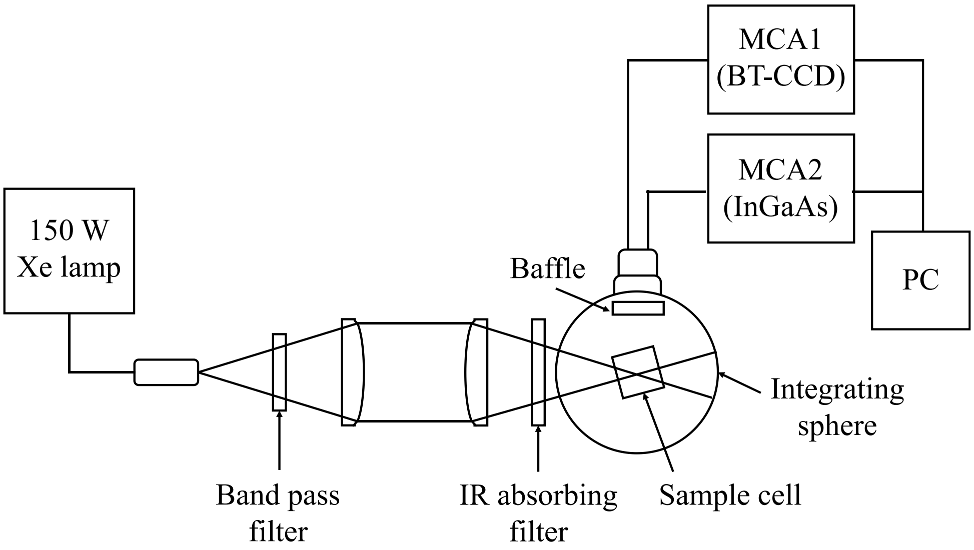

Figure 3-2. A new integrating sphere instrument developed for the absolute photoluminescence quantum yield measurements in the wavelength range of 350−1650 nm.

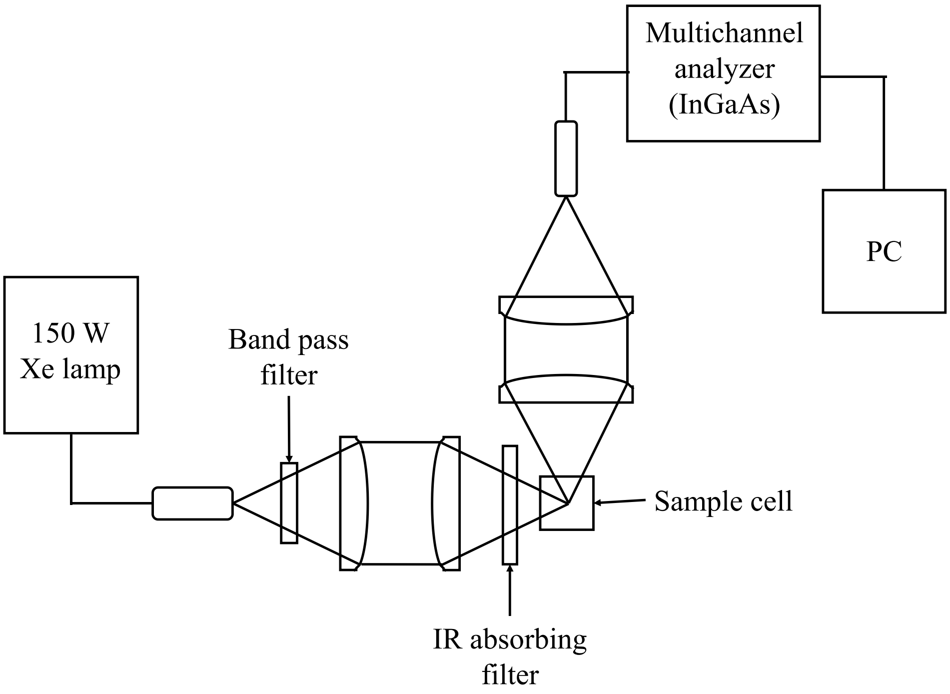

Figure 3-3. The block diagram of experimental setup for quantum yield measurements based on the relative method.

3-2-4 Time-Resolved Photoacoustic Measurements

To determine the quantum yield of intersystem crossing ($\phi_{\rm isc}$) of PtTFPP, the time-resolved photoacoustic (PA) measurements were carried out. The third harmonic of a Nd^{3+}:YAG laser (355 nm, Spectra-Physics, GCR-130, pulse width 6 ns) was used as the excitation light source. The PA signals derived from nonradiative transitions of solute molecules were detected using a piezoelectric transducer (Panametrics, Model V103, 1 MHz) and amplified using a high gain preamiplifier (Panametrics, Model 5676, 40 dB). The output voltage was recorded on a digitizing oscilloscope (Tektronix, TDS-744, 500 MHz, sample rate 2GS/s) and transferred to a personal computer. The laser fluence was varied using a neutral density filter, and the energy of laser pulse was recorded on a pyroelectronic energy meter (Laser Precision, RjP735 and Rj 7610). Figure 3-4 shows the schematic diagram of this instrument. The absorbance of each sample solution was adjusted to be ca. 0.18 at excitation wavelength of 355 nm. The intensity (H) of the PA signal can be described as the following equation,

$$H = KE_{\rm L}\alpha(1\text{-}10^{-A}) \qquad (3\text{-}2)$$

where K is a constant including the thermoelastic properties of the solution and instrumental factors, $E_{\rm L}$ is the laser pulse fluence, A is the absorbance of the sample solution, and α is the fraction of energy deposited in the medium as prompt heat within the time resolution of the experiment. Since it is known that the α values for the reference compound, 2-hydroxybenzophenone (2HBP), in CCl_4 and CH_3CN can be presumed to be unity, the α value of the PtTFPP solution can be determined from the ratio of the slopes of straight lines. The $\phi_{\rm isc}$ value was determined by the following equation based on the energy balance,

$$E_\lambda = \phi_f \langle E_S \rangle + \phi_{isc} E_T + \alpha E_\lambda \qquad (3\text{-}3)$$

where E_λ is the energy of the excitation photon (337 kJmol^{-1}), ϕ_f and ϕ_{isc} are the quantum yields of the fluorescence and intersystem crossing, $\langle E_S \rangle$ is the average energy dissipated by fluorescence from the excited singlet state, and E_T is the energy of the excited triplet state, respectively.

3-2-5 Quantum Yield Measurements of Singlet Oxygen Formation and Emission Lifetime of Singlet Oxygen

Quantum yield of singlet oxygen formation and emission lifetime of singlet oxygen were measured using the instrument described in Section 2-2-7. Here, the second harmonic (532 nm) of Nd^{3+}: YAG laser was used as excitation wavelength in the emission lifetime measurements of CS_2 and halogenated benzene solutions.

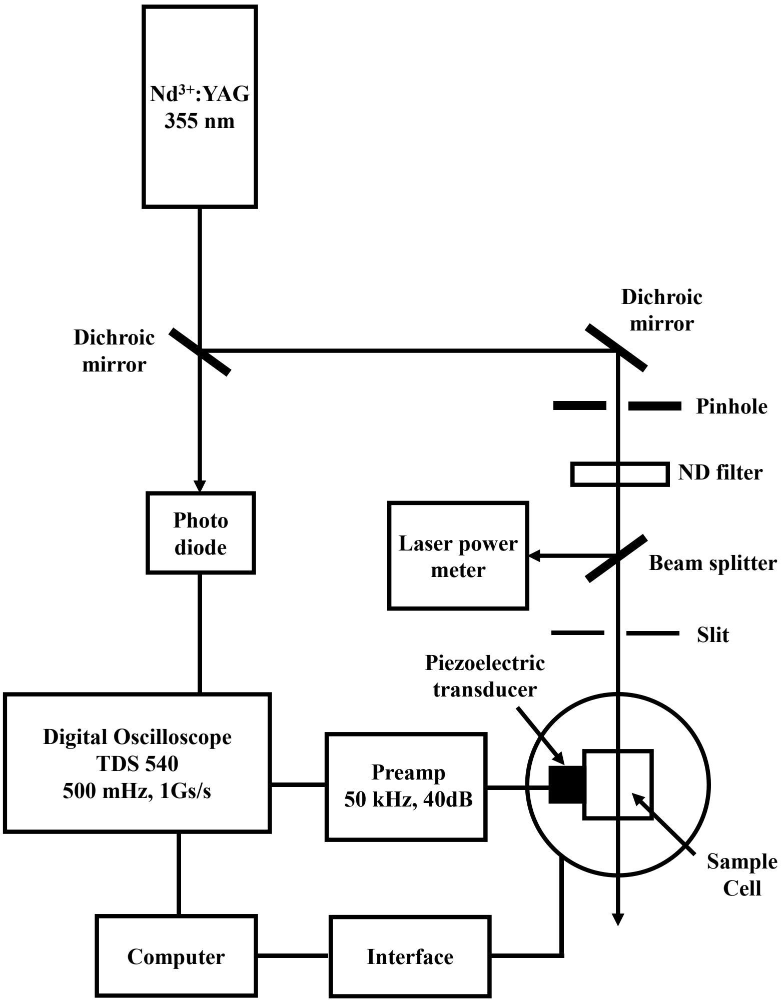

Figure 3-4. Schematic diagram of time-resolved photoacoustic measurement instrument.

3-3 Results and Discussion

3-3-1 Spectral Calibration of Integrating Sphere Instrument

The integrating sphere instrument developed for absolute quantum yield measurements of NIR emission up to 1650 nm employs two multichannel analyzer systems using BT-CCD and InGaAs as detectors (MCA1 and MCA2 in Figure 3-2, respectively). To measure the emission quantum yield of $O_2(a^1\Delta_g)$ which has an emission peak at about 1270 nm, the former analyzer was used to measure the excitation light profile at around 525 nm and the latter was used to obtain the emission profile of the $a^1\Delta_g$ ($v' = 0$) → $X^3\Sigma_g^-$ ($v'' = 0$) transition. The spectral response of this instrument was fully calibrated using deuterium and halogen standard light sources for the wavelength range between 350 and 1100 nm and 900−1650 nm for MCA1 and MCA2, respectively. To confirm the reliability of the spectral calibrations, the emission quantum yield of a phosphor, Y_2O_2S:Yb,Er [27], which gives an emission spectrum in the 900−1100 nm region was measured (Figure 3-5). The discrepancy at around a peak (980 nm) might be caused by the difference in the spectral resolution between MCA1 (1024 channels for 350−1100 nm) and MCA2 (256 channels for 900−1650 nm), and those at around 920 and 1090 nm are attributable to lower sensitivities of MCA2 and MCA1 in these spectral regions. The influence of these differences can be ignored in the quantum yield measurements; measurements using the multichannel analyzer equipped with a BT-CCD detector (MCA1) gave a quantum yield of 0.392, and those using the combination of MCA1 (for excitation) and MCA2 equipped with an InGaAs detector (for emission) gave nearly the same quantum yield (0.393). The good agreement in the observed quantum yields demonstrates that the combined detection system consisting of MCA1 (for excitation) and MCA2 (for emission) is precisely corrected for spectral sensitivity.

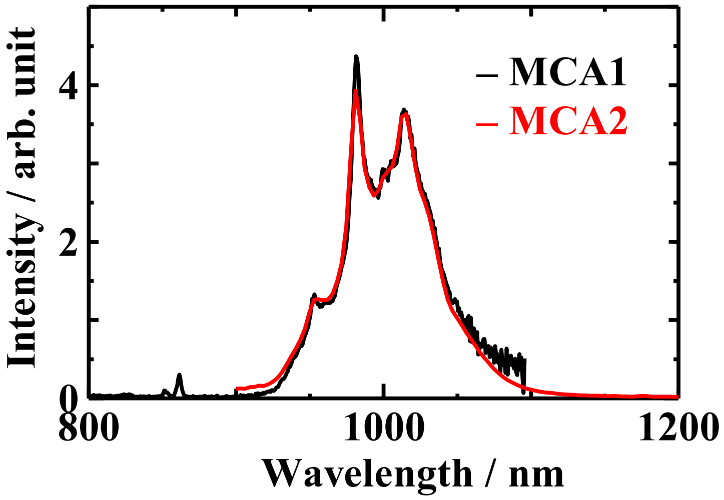

Figure 3-5. Emission spectra of Y_2O_2S:Yb,Er measured using MCA1 and MCA2 of the integrating sphere instrument shown in Figure 3-2.

3-3-2 Quantum Yield of $a^1\Delta_g \rightarrow X^3\Sigma_g^-$ Emission of O_2 in Solution

Singlet oxygen ($a^1\Delta_g$) was produced by energy transfer from the excited triplet PtTFPP (T_1) to molecular oxygen in the ground state ($X^3\Sigma_g^-$). Figure 3-6 shows the energy state diagram of the collision complex between the photosensitizer PtTFPP and molecular oxygen in solution, which includes relevant intramolecular and intermolecular relaxation processes. Using the rate constants and quantum yields of various deactivation processes, the observed emission quantum yield ($\Phi_p^{1\Delta}$) of $O_2(a^1\Delta_g)$ is given by

$$\Phi_p^{1\Delta} = \Phi^{1\Delta}\phi_p = \Phi^{1\Delta}\frac{k_r^{1\Delta}}{k_r^{1\Delta} + k_{nr}^{1\Delta} + k_q[S] + k_q'[O_2]} = \Phi^{1\Delta}k_r^{1\Delta}\tau_p^{1\Delta} \qquad (3\text{-}4)$$

where $\Phi^{1\Delta}$, ϕ_p, and $\tau_p^{1\Delta}$ are the quantum yield of singlet oxygen formation, and the phosphorescence quantum yield and lifetime of the $a^1\Delta_g$ (v′ = 0) state in solvents, respectively, $k_r^{1\Delta}$ and $k_{nr}^{1\Delta}$ are the radiative and nonradiation rate constants of $O_2(a^1\Delta_g)$, k_q and k_q' are the bimolecular quenching rate constants of $O_2(a^1\Delta_g)$ by photosensitizer and $O_2(X^3\Sigma_g^-)$, and [S] and [O_2] are the concentrations of the photosensitizer and $O_2(X^3\Sigma_g^-)$ in solution, respectively.

Figure 3-7 shows the excitation light profile and the emission spectrum of $O_2(a^1\Delta_g)$ obtained by setting quartz cells with and without a sample solution, when an air-saturated CCl_4 solution of PtTFPP is set inside the integrating sphere. The excitation light profile after passing through a band-pass filter with the center wavelength of 525 nm (black line) is decreased by light absorption of PtTFPP solution (red line). The difference of the integrated intensities in the absence and presence of PtTFPP solution (shaded area) is proportional to the number of photons absorbed by PtTFPP solution. The emission spectrum (red line) observed at around 1270 nm can be attributed to the $a^1\Delta_g$ (v′ = 0) →

$X^3\Sigma_g^-$ ($v'' = 0$) emission of singlet oxygen from the characteristic wavelength. The area of this emission band is proportional to the number of photons emitted by the $a^1\Delta_g \rightarrow X^3\Sigma_g^-$ transition. By using eq 3-1, the absolute emission quantum yield ($\Phi_p^{1\Delta}$) of $O_2(a^1\Delta_g)$ in air-saturated CCl_4 was found to be 1.8×10^{-2} at [PtTFPP] = 7.4×10^{-6} M by calculating the ratio between the absorbed area in the excitation light profile and the integrated emission intensity at around 1270 nm in Figure 3-7.

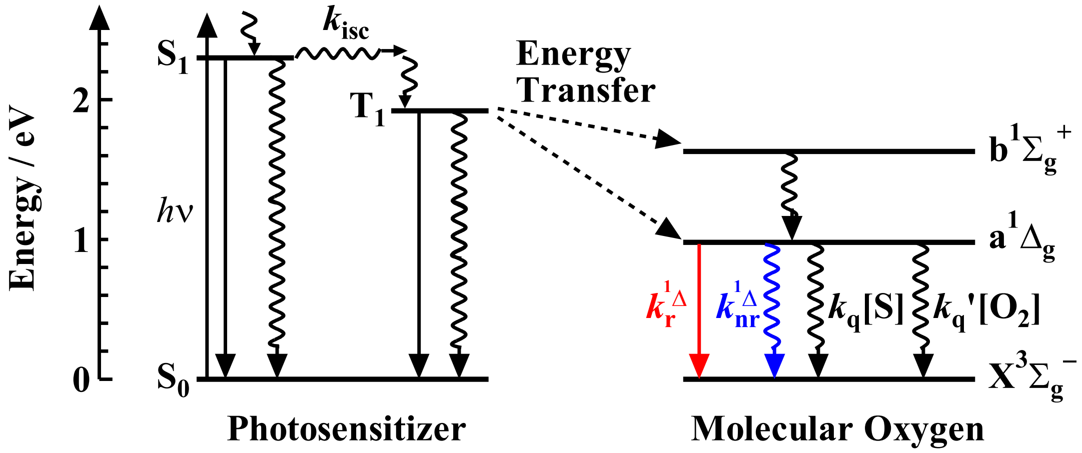

Figure 3-6. Energy state diagram of collision complexes between photosensitizer (PtTFPP) and molecular oxygen. Relaxation processes involving energy transfer from photosensitizer to molecular oxygen are denoted by the rate constant or quantum efficiency.

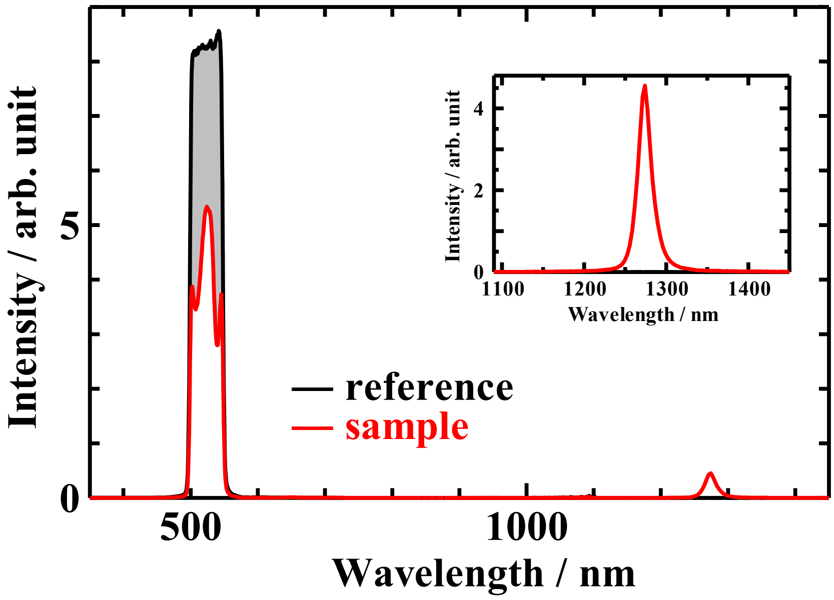

Figure 3-7. Excitation light profiles and emission spectrum with (red line) and without (black line) PtTFPP solution (7.4 × 10^{-6} M in CCl_4) obtained using the instrument shown in Figure 3-2. Excitation wavelengths were selected using a band-pass filter (center wavelength 525 nm, fwhm 50 nm). Inset shows the expanded emission spectrum of $O_2(a^1\Delta_g)$ in CCl_4. Exposure times in the emission spectral measurements were set to 3 s.

Because the emission lifetimes of the $a^1\Delta_g \rightarrow X^3\Sigma_g^-$ transition in CCl_4 and CS_2 were much longer than those in other solvents used in this study (vide infra), the $O_2(a^1\Delta_g)$ emission in CCl_4 and CS_2 appears to be quenched by collisions with the photosensitizer molecule (PtTFPP) and molecular oxygen in the ground state ($X^3\Sigma_g^-$). By using eq 3-5, the quenching rate constants (k_q) by PtTFPP in air-saturated CCl_4 and CS_2 were examined. Equation 3-5 was derived from eq 3-4 by assuming that $\Phi^{^1\Delta} = 1$ as described in Section 3-3-3.

$$\left(\Phi_p^{^1\Delta}\right)^{-1} = \frac{k_r^{^1\Delta} + k_{nr}^{^1\Delta} + k_q'[O_2]}{k_r^{^1\Delta}} + \frac{k_q}{k_r^{^1\Delta}}[S] \qquad (3\text{-}5)$$

Figure 3-8 shows the plots of $\left(\Phi_p^{^1\Delta}\right)^{-1}$ vs the PtTFPP concentrations in CCl_4 and CS_2, which gave straight lines. From the slopes ($k_q / k_r^{^1\Delta}$) of these straight lines and $k_r^{^1\Delta}$ described in Section 3-3-4, the bimolecular quenching rate constants (k_q) of $O_2(a^1\Delta_g)$ by PtTFPP in CCl_4 and CS_2 were determined to be 2.5×10^6 and 1.5×10^6 $M^{-1}s^{-1}$, respectively. From the values of intercept, the $\Phi_p^{^1\Delta}$ values in the absence of sensitizer quenching in CCl_4 and CS_2 were estimated to be 2.2×10^{-2} and 6.4×10^{-2}, respectively. These $\Phi_p^{^1\Delta}$ include quenching due to ground-state $O_2(X^3\Sigma_g^-)$, although the contribution is small, even in air-saturated CCl_4 and CS_2, as discussed in Section 3-3-4.

Similar measurements of absolute emission quantum yield for $O_2(a^1\Delta_g)$ were performed in different solvents. For example, Figure 3-9a and b show the excitation light profiles and emission spectra measured in air-saturated CH_3CN and EtOH, respectively. Although the integrating sphere instrument gave clearly the emission spectrum of $O_2(a^1\Delta_g)$ in CH_3CN, the emission band at around 1270 nm in EtOH was very weak because of the extremely low emission quantum yield. Hence, $\Phi_{\mathrm{p}}^{^1\Delta}$ measurements based on the relative method were also performed in order to confirm the reliability of the absolute quantum yield measurements in solvents that give an emission quantum yield lower than ca. 10^{-4}. Using the absolute $\Phi_{\mathrm{p}}^{^1\Delta}$ value in $\mathrm{CCl_4}$ ($\Phi_{\mathrm{p}}^{^1\Delta}(\mathrm{CCl_4})$) as a reference, the relative $\Phi_{\mathrm{p}}^{^1\Delta}$ value for PtTFPP solutions in different solvents ($\Phi_{\mathrm{p}}^{^1\Delta}(\mathrm{X})$) was calculated according to eq 3-6:

$$\Phi_{\mathrm{p}}^{^1\Delta}(\mathrm{X}) = \Phi_{\mathrm{p}}^{^1\Delta}(\mathrm{CCl_4}) \frac{I(\mathrm{X})}{I(\mathrm{CCl_4})} \frac{(1-T(\mathrm{CCl_4}))}{(1-T(\mathrm{X}))} \frac{n^2(\mathrm{X})}{n^2(\mathrm{CCl_4})} \qquad (3\text{-}6)$$

where $I(\mathrm{X})$ and $I(\mathrm{CCl_4})$ are the integrated emission intensity of $\mathrm{O_2(a^1\Delta_g)}$ taken in solvent X and reference $\mathrm{CCl_4}$, $T(\mathrm{X})$ and $T(\mathrm{CCl_4})$ represent the transmittance of excitation light for PtTFPP solutions in solvent X and $\mathrm{CCl_4}$ measured by using integrating sphere instrument, and $n(\mathrm{X})$ and $n(\mathrm{CCl_4})$ are the refractive index of the solvent X and $\mathrm{CCl_4}$. The results in different solvents obtained by using the instruments based on absolute and relative methods are shown in Appendices 3-1 and 3-2.

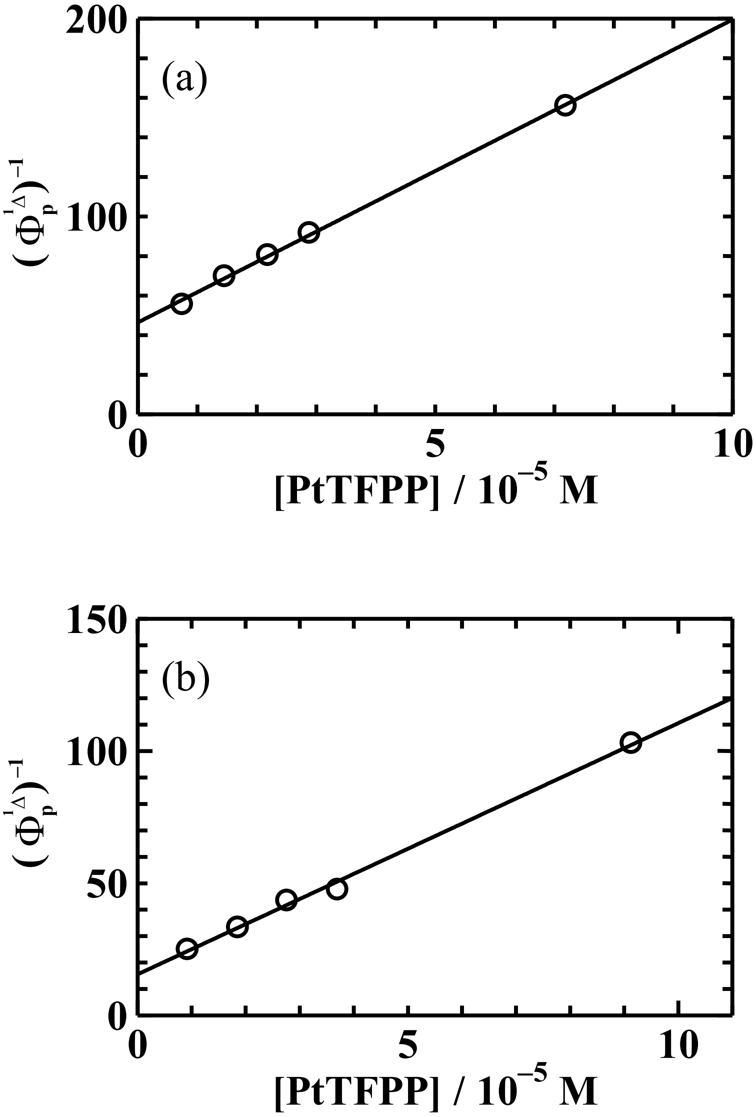

Figure 3-8. Plots of the inverse of $\Phi_p^{^1\Delta}$ vs PtTFPP concentrations in (a) CCl_4 and (b) CS_2 at 293 K taken using an integrating sphere instrument shown in Figure 3-2.

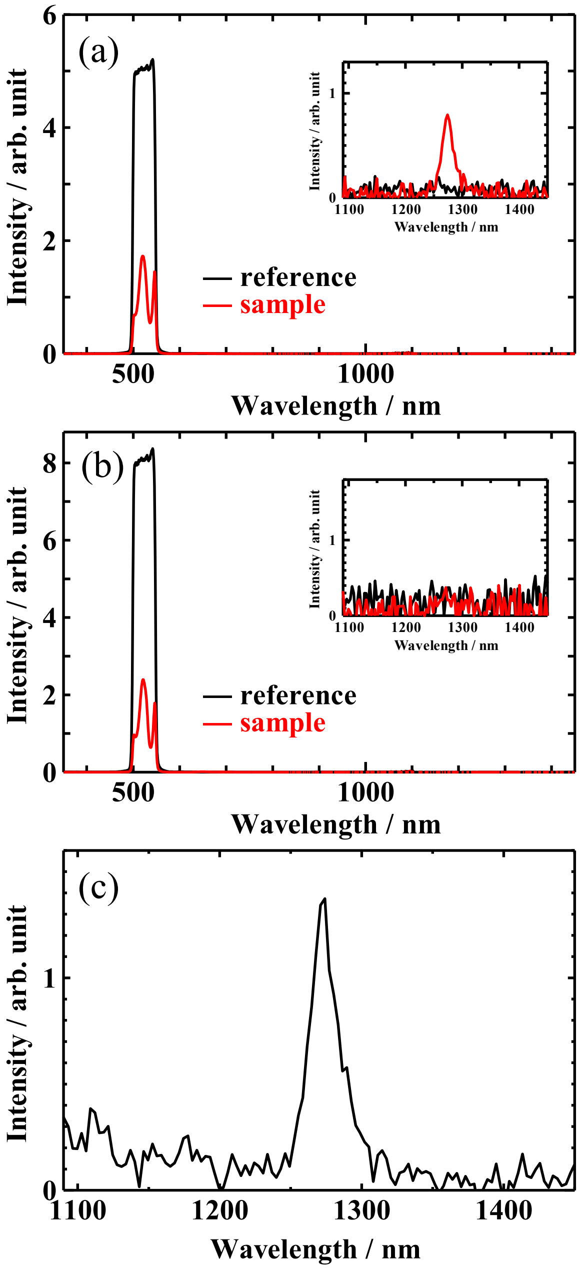

Figure 3-9. Excitation light profiles and emission spectrum of (a) CH_3CN solution and (b) EtOH solution with (red line) and without (black line) PtTFPP obtained using the instrument shown in Figure 3-2. Excitation wavelengths were selected using a band pass filter (center wavelength 525 nm, fwhm 50 nm). Insets of (a) and (b) show the expanded emission spectrum of $O_2(a^1\Delta_g)$ in CH_3CN and EtOH, respectively. Emission spectrum of $O_2(a^1\Delta_g)$ in EtOH obtained by using the instrument in Figure 3-3 is shown in (c). Exposure times in the emission spectral measurements were set to 5 s for (a) and (b), and 8 s for (c), respectively.

The $\Phi_p^{1\Delta}$ values obtained using the instruments shown in Figures 3-2 and 3-3 are listed in Table 3-1 along with the literature values measured by the relative method [28−34]. The absolute $\Phi_p^{1\Delta}$ value of 2.2×10^{-2} in CCl_4, which is corrected for sensitizer quenching, is much larger than the value of 4.4×10^{-3} reported by Krasnovsky, who measured the $\Phi_p^{1\Delta}$ value using the fluorescence quantum yield of tetraphenylporphin as a standard [28]. The discrepancy might originate, at least in part, from sensitizer-induced quenching occurring in the experiments by Krasnovsky. The $\Phi_p^{1\Delta}$ value of 2.2×10^{-2} in CCl_4 reported by Losev et al. [29], which was obtained using the emission of Li−Nd phosphate glass as a standard, is very similar to the obtained value in this study. Losev et al. determined $\Phi_p^{1\Delta}$ for an exceedingly dilute sensitizer solution (1.2×10^{-8} M) to compensate for sensitizer quenching. However, their $\Phi_p^{1\Delta}$ values in benzene and toluene are about 1 order of magnitude larger than the obtained values in this study [30]. The absolute and relative $\Phi_p^{1\Delta}$ values of this study in benzene (C_6H_6) are 2.6×10^{-5} and 3.2×10^{-5}, respectively. These are consistent with the value (4.7×10^{-5}) determined by Schmidt [31] using the fluorescence quantum yield of different sensitizers as reference, although their value is somewhat larger than the value obtained in this study. Schmidt et al. determined the $\Phi_p^{1\Delta}$ in other solvents based on the relative method using their $\Phi_p^{1\Delta}$ (4.7×10^{-5}) in C_6H_6 as reference [32]. Systematic differences between the $\Phi_p^{1\Delta}$ values in this study and those by Schmidt et al. are, therefore, attributable to differences in the $\Phi_p^{1\Delta}$ values in C_6H_6. On the other hand, the $\Phi_p^{1\Delta}$ values reported by Shimizu et al. [33,34] were found to be 1 order of magnitude smaller than the values of this study in all solvents. They first determined the absolute $\Phi_p^{1\Delta}$ value in CCl_4 by using the fluorescence quantum yield of quinine bisulfate in 1 N H_2SO_4 as a standard [33], and then the $\Phi_{\mathrm{p}}^{1\Delta}$ value in other solvents based on the relative method was determined using their absolute $\Phi_{\mathrm{p}}^{1\Delta}$ value in CCl_4 [34]. Thus, the systematic discrepancy with the $\Phi_{\mathrm{p}}^{1\Delta}$ value in this sturdy may have come from their lower $\Phi_{\mathrm{p}}^{1\Delta}$ value in CCl_4. Shimizu et al. used a photon-counting technique based on pulsed laser excitation to determine quantum yields, and time-resolved detection was employed to remove unwanted emission with lifetimes different from that of $O_2(a^1\Delta_g)$ [33,34]. In this study, however, short-lifetime components other than $O_2(a^1\Delta_g)$ were not observed in the emission decay profiles at 1270 nm. So time-resolved analyses are not necessary for the quantum yield measurements of the systems in this study.

As noted below, the quantum yield of singlet oxygen formation ($\Phi^{1\Delta}$) of air-saturated PtTFPP solutions can be assumed to be unity in all solvents used. Hence, the $\Phi_{\mathrm{p}}^{1\Delta}$ values in Table 3-1 correspond to the intrinsic phosphorescence quantum yields ϕ_{p} of $O_2(a^1\Delta_g)$ in these solvents.

Table 3-1. Comparison of $\Phi_{p}^{1\Delta}$ values in different solvents at 293 K obtained in this study with values from the literature.[a]

	$\Phi_{p}^{1\Delta}$					
	this work					
solvent	absolute	relative	KR	LO	SC	SH
CCl_4	2.2×10^{-2} [b]		4.4×10^{-3} [c]	2.2×10^{-2} [d]	8.9×10^{-2} [e]	1.38×10^{-3} [f]
CS_2	6.4×10^{-2} [b]				4.0×10^{-2} [e]	
C_6H_6	2.6×10^{-5}	3.2×10^{-5}		1.4×10^{-4} [g]	4.7×10^{-5} [h]	4.5×10^{-6} [i]
C_6D_6	5.5×10^{-4}	6.4×10^{-4}				
$PhCH_3$	1.7×10^{-5}	2.9×10^{-5}		1.2×10^{-4} [g]		4.3×10^{-6} [i]
PhCl	4.0×10^{-5}	5.2×10^{-5}				
PhBr	4.4×10^{-5}	6.2×10^{-5}				
PhI	3.3×10^{-5}	4.6×10^{-5}				
$CHCl_3$	1.2×10^{-4}	1.2×10^{-4}			3.6×10^{-4} [e]	2.05×10^{-5} [i]
CH_3CN	1.5×10^{-5}	2.2×10^{-5}			7.0×10^{-5} [e]	3.8×10^{-6} [i]
CD_3CN	4.6×10^{-4}	3.7×10^{-4}				
EtOH	ND	4.8×10^{-6}				5.8×10^{-7} [i]
EtOD	ND	9.8×10^{-6}				

[a] KR, Krasnovsky et al.; LO, Losev et al.; SC, Schmidt et al.; SH, Shimizu et al.

[b] The values extrapolated to [PtTFPP] = 0. [c] Ref [28]. [d] Ref [29]. [e] Ref [32]. [f] Ref [33]. [g] Ref [30]. [h] Ref [31]. [i] Ref [34].

3-3-3 Photophysical Properties of PtTFPP and Quantum Yield of Singlet Oxygen Formation

The absorption and emission spectra of the photosensitizer PtTFPP in 2-methyltetrahydrofuran (2-MeTHF) solution at room temperature and at 77 K are shown in Figure 3-10. The lowest absorption band for PtTFPP was observed at around 540 nm. The emission spectrum of PtTFPP at room temperature was significantly quenched by oxygen and could be assigned to phosphorescence (Figure 3-11). Fluorescence was not observed, even at 77 K, thus suggesting that the quantum yield of intersystem crossing (ϕ_{isc}) is close to unity. To evaluate the ϕ_{isc} values of PtTFPP, the time-resolved photoacoustic measurements of PtTFPP solutions in CCl_4 and CH_3CN were performed. Figure 3-12 shows the laser power dependences of PA signal amplitude of PtTFPP and 2HBP as a reference in CCl_4 and CH_3CN. As shown in Figure 3-12, there were linear relationships between PA signal amplitude and the laser energy. These results indicate that biphotonic processes and ground state depletion are not involved. From the ratio of the slopes of the straight lines of PtTFPP and 2HBP, the α values of PtTFPP in CCl_4 and CH_3CN were determined to be 0.47 and 0.45, respectively. The triplet energy (E_{T}) of PtTFPP was determined to be 185 $\mathrm{kJmol^{-1}}$ from the phosphorescence spectrum at 77K shown in Figure 3-10. Because the fluorescence quantum yield (ϕ_{f}) in eq 3-3 could be assumed to be zero, the ϕ_{isc} values of PtTFPP were calculated to be 0.96 and 1.01 in CCl_4 and CH_3CN, respectively.

The quantum yield of singlet oxygen formation of PtTFPP in different solvents ($\Phi^{1\Delta}(\mathrm{PtTFPP})$) under air-saturated condition was evaluated using the $\Phi^{1\Delta}$ values in perinaphthenone (PN) solution ($\Phi^{1\Delta}(\mathrm{PN})$) in the same solvent as reference. Here, the

$\Phi^{1\Delta}(\mathrm{PN})$ values were presumed to be unity in the solvents used in this study [25]. $O_2(a^1\Delta_g)$ was formed by 355 nm laser pulse excitation of PtTFPP solutions using the apparatus shown in Figure 2-5 in Section 2-2-7, and the $a^1\Delta_g \rightarrow X^3\Sigma_g^-$ emission intensity ($I^{1\Delta}(\mathrm{PtTFPP})$) extrapolated to the laser pulse peak was compared with that of ($I^{1\Delta}(\mathrm{PN})$) obtained for PN solutions with the same solvent according to the following equation:

$$\Phi^{1\Delta}(\mathrm{PtTFPP}) = \Phi^{1\Delta}(\mathrm{PN}) \frac{I^{1\Delta}(\mathrm{PtTFPP})}{I^{1\Delta}(\mathrm{PN})} \frac{A(\mathrm{PN})}{A(\mathrm{PtTFPP})} \qquad (3\text{-}7)$$

where A(PtTFPP) and A(PN) are the absorbances of PtTFPP and PN solutions at 355 nm, respectively. The obtained $\Phi^{1\Delta}$ values in selected solvents are summarized in Table 3-2. Although the $\Phi^{1\Delta}$ values in CS_2, PhCl, PhBr, and PhI could not be determined owing to the absorption of solvent molecules at 355 nm, it can be seen from Table 3-2 that the quantum yield of $O_2(a^1\Delta_g)$ formation can be assumed to be unity in these solvents.

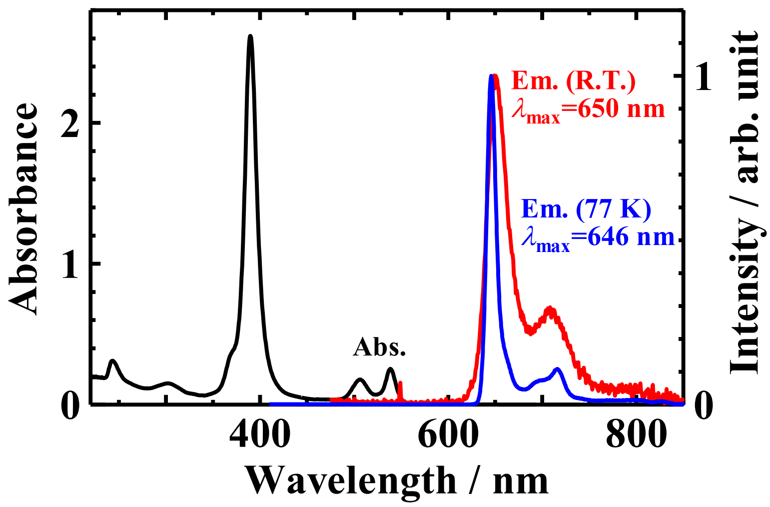

Figure 3-10. Absorption (black line) and emission spectra of PtTFPP in deaerated 2-MeTHF at room temperature (red line) and 77 K (blue line) (λ_{exc} = 355 nm).

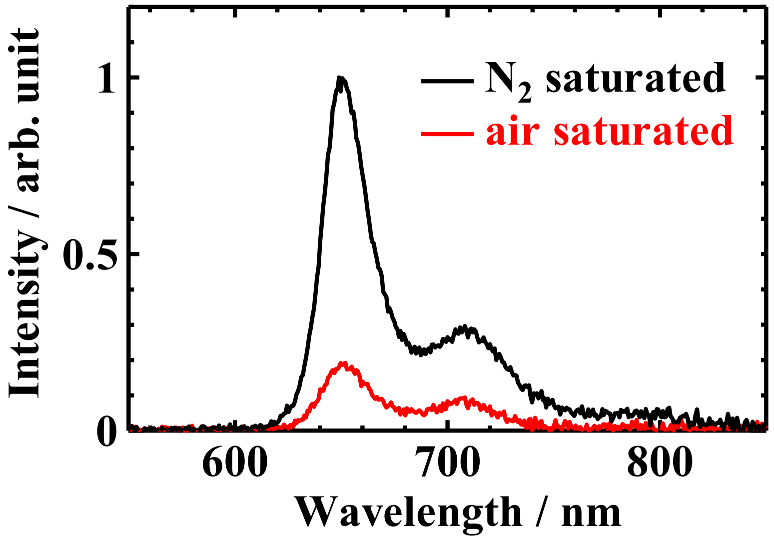

Figure 3-11. Emission spectra of PtTFPP in N_2-saturated (black line) and air-saturated (red line) in 2-MeTHF.

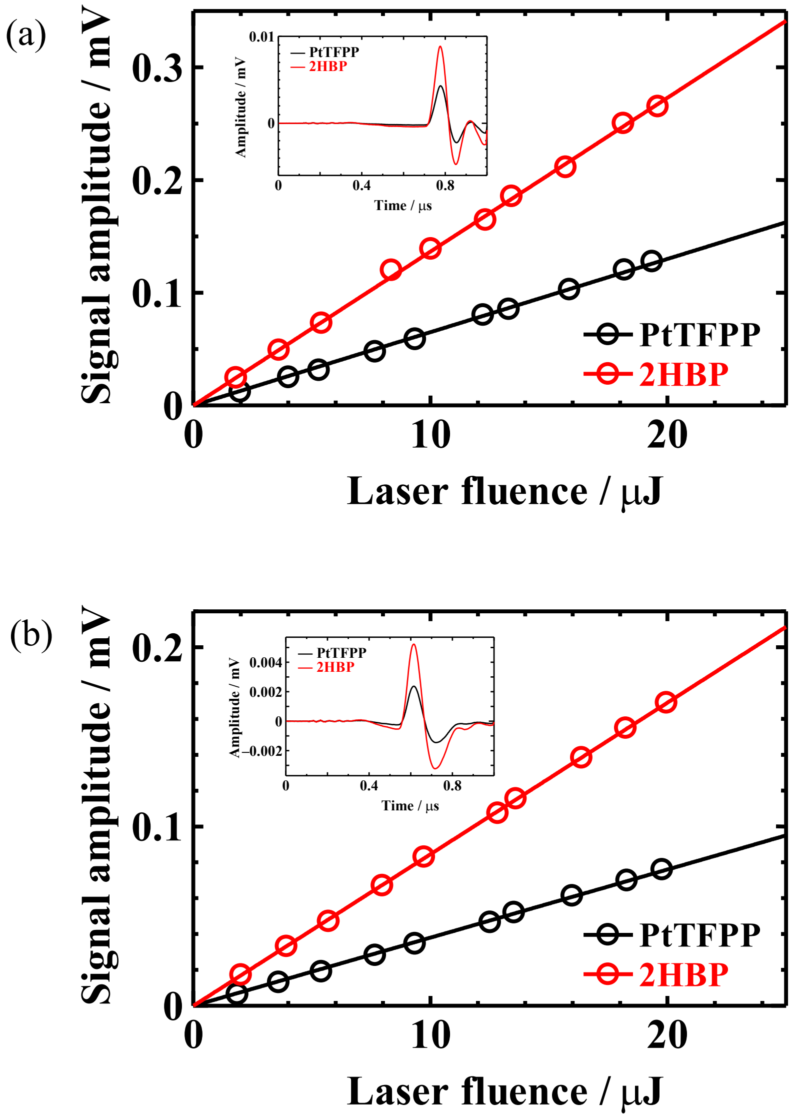

Figure 3-12. Laser energy dependencies of PA signal amplitude of PtTFPP and 2HBP in (a) CCl_4 and (b) CH_3CN at 293 K (λ_{exc} = 355 nm). Inset of (a) and (b) shows the PA signals in CCl_4 and CH_3CN, respectively.

Table 3-2. Quantum yield of singlet oxygen formation ($\Phi^{^1\Delta}$) and photophysical parameters of singlet oxygen in different solvents (sensitizer: PtTFPP).

solvent	$\Phi^{^1\Delta}$ [a]	$\tau_p^{^1\Delta}$ / μs	$\Phi_p^{^1\Delta}$	$k_r^{^1\Delta}$ / s^{-1}	$k_{nr}^{^1\Delta}$ / s^{-1}
CCl_4	1.00	5.04×10^3 [b]	8.1×10^{-3} [b] (2.2×10^{-2}) [c]	1.6	6.8×10^1
CS_2		9.08×10^3 [b]	1.4×10^{-2} [b] (6.4×10^{-2}) [c]	1.6	1.4×10^1
C_6H_6	0.98	31.7	3.2×10^{-5}	1.1	3.2×10^4
C_6D_6	0.99	608	5.5×10^{-4}	0.90	1.6×10^3
$PhCH_3$	0.98	31.2	2.9×10^{-5}	0.93	3.2×10^4
PhCl		44.8	5.2×10^{-5}	1.2	2.2×10^4
PhBr		43.1	6.2×10^{-5}	1.4	2.3×10^4
PhI		28.5	4.6×10^{-5}	1.6	3.5×10^4
$CHCl_3$	1.00	173	1.2×10^{-4}	0.69	5.8×10^3
CH_3CN	0.98	83.4	2.2×10^{-5}	0.27	1.2×10^4
CD_3CN	0.96	1.59×10^3	4.6×10^{-4}	0.29	6.3×10^2
EtOH	0.96	15.2	4.8×10^{-6}	0.32	6.6×10^4
EtOD	0.99	32.4	9.8×10^{-6}	0.30	3.1×10^4

[a] Uncertainties ± 10%.

[b] $\tau_p^{^1\Delta}$ and $\Phi_p^{^1\Delta}$ were measured for solutions with the same PtTFPP concentration.

[c] The values extrapolated to [PtTFPP] = 0.

3-3-4 Radiative and Nonradiative Rate Constants of $O_2(a^1\Delta_g)$

The most important parameters for understanding the photophysical properties of $O_2(a^1\Delta_g)$ in solution are the radiative and nonradiative rate constants. Because the ϕ_{isc} and $\Phi^{1\Delta}$ of air-saturated PtTFPP solutions can be assumed to be unity in all the solvents used in this study, the radiative rate constant ($k_r^{1\Delta}$) can be calculated from the $\Phi_p^{1\Delta}$ and $\tau_p^{1\Delta}$ values measured under identical sensitizer and O_2 concentrations according to eq 3-4. Therefore, the $\tau_p^{1\Delta}$ values for air-saturated PtTFPP solutions were measured using the apparatus shown in Figure 2-5. Here, the PtTFPP concentration was adjusted to be equal to that used in the $\Phi_p^{1\Delta}$ measurement in each solvent. The phosphorescence decay curves of $O_2(a^1\Delta_g)$ measured in air-saturated CCl_4 and CH_3CN are shown in Figure 3-13. Both decay curves followed single exponential decay functions, and the lifetimes were found to be 5.04 ms and 83.4 μs in CCl_4 and CH_3CN, respectively. The $\tau_p^{1\Delta}$ values obtained in different air-saturated solvents are shown in Table 3-2, and the decay curves of singlet oxygen in different air-saturated solvents are shown in Appendix 3-3. As shown in Table 3-2, the lifetime of $O_2(a^1\Delta_g)$ varies significantly depending on the solvent, as reported previously [34]. Assuming that the values of ϕ_{isc} and $\Phi^{1\Delta}$ in eq 3-4 are unity in the solvents used, the $k_r^{1\Delta}$ values were calculated from $\tau_p^{1\Delta}$ and $\Phi_p^{1\Delta}$, as shown in Table 3-2. To compare the $k_r^{1\Delta}$ values in this study with those reported by other groups, the representative literature values for $k_r^{1\Delta}$ are summarized in Table 3-3. The $k_r^{1\Delta}$ values reported by Schmidt and co-workers [35,36], Ogilby and co-workers [37,38] and Darmanyan [39] are similar to the values determined using an integrating sphere instrument, although their $k_r^{1\Delta}$ values in all solvents are somewhat larger than the values obtained in this study. The $k_r^{1\Delta}$ values reported by Shimizu et al. [34] are nearly 1 order of magnitude smaller than the values of this study in all solvents. This difference can be vested in their $\Phi_{\mathrm{p}}^{1\Delta}$ value in CCl_4, which was about 1 order of magnitude smaller than the values of this study (Table 3-1). As evident from Table 3-3, the $k_{\mathrm{r}}^{1\Delta}$ values are much larger than that (2.6×10^{-4} s^{-1}) in the isolated $O_2(a^1\Delta_g)$ [40] and vary depending on the solvent. This is consistent with the former results shown in Table 3-3 [34−39]. The mechanism of the collision-induced $a^1\Delta_g \rightarrow X^3\Sigma_g^-$ transitions has been widely studied by experiments [36,39,41,42] and theoretical treatments [43,44].

The $k_{\mathrm{nr}}^{1\Delta}$ values were derived using $\tau_{\mathrm{p}}^{1\Delta}$ and $k_{\mathrm{r}}^{1\Delta}$ in Table 3-2 according to eq 3-8:

$$k_{\mathrm{nr}}^{1\Delta} = (\tau_{\mathrm{p}}^{1\Delta})^{-1} - (k_{\mathrm{r}}^{1\Delta} + k_{\mathrm{q}}[\mathrm{S}] + k_{\mathrm{q}}'[\mathrm{O_2}]) \qquad (3\text{-}8)$$

where the contribution of the quenching processes by the photosensitizer molecule and molecular oxygen in the ground state, which are denoted as $k_q[S]$ and $k_q'[O_2]$ in eq 3-8, was neglected for all solvents other than CCl_4 and CS_2, because $k_q[S]$ and $k_q'[O_2]$ are much smaller than $(\tau_{\mathrm{p}}^{1\Delta})^{-1}$. In CCl_4 and CS_2, the $k_q[S]$ values were calculated to be 1.2×10^2 and 8.5×10^1 s^{-1} using the k_q values and the photosensitizer concentrations, which were used in lifetime measurements. The quenching rate constants k_q' by $O_2(X^3\Sigma_g^-)$ in CCl_4 and CS_2 were evaluated to be 3.5×10^3 and 6.4×10^3 $M^{-1}s^{-1}$ from the $\tau_{\mathrm{p}}^{1\Delta}$ in different O_2 concentrations reported by Schmidt et al. [45], and the $k_q'[O_2]$ values were estimated to be 9.1 and 9.6 s^{-1}, respectively. The obtained $k_{\mathrm{nr}}^{1\Delta}$ values are listed in the last column of Table 3-2. As can be seen in Table 3-2, the $k_{\mathrm{nr}}^{1\Delta}$ values vary significantly depending on the solvent nature; the $k_{\mathrm{nr}}^{1\Delta}$ in solvents with C−H bond(s) is much larger than those in CCl_4 and CS_2, and deuteration of the C−H bond substantially reduces $k_{\mathrm{nr}}^{1\Delta}$. Similar solvent effects on nonradiative transitions have also been recognized in lifetime measurements [45,46] and can be explained by electronic-to-vibrational energy transfer; thus, the electronic excitation energy of $O_2(a^1\Delta_g)$ is converted into the vibrational energy of $O_2(X^3\Sigma_g^-)$ and peripheral X−Y bonds of the solvent molecule (Figure 3-14). The quenching rate constant (k_q) by solvent molecules has been expressed by the following equation [24,47],

$$k_\mathrm{q} \approx Z\sum_{\mathrm{sv''}} F_\mathrm{s} F_{\mathrm{v''}} R_{\mathrm{sv''}} \qquad (3\text{-}9),$$

where Z is a term that is independent of the specific nature of the solvent, F_s is the Franck-Condon factor for a particular (0 → s) vibrational transition of the solvent, $F_{v''}$ is the corresponding factor for the ($v' = 0 \rightarrow v''$) vibronic transition of $^1O_2$ to the ground state, and $R_{sv''}$ is related to the energy difference between the oxygen vibronic transition and the appropriate solvent vibrational energy level (an off-resonance factor). Because the $R_{sv''}$ value is increased with a decrease of the energy difference between two transitions, the k_q value by C−H bond becomes larger than that by C−D bond.

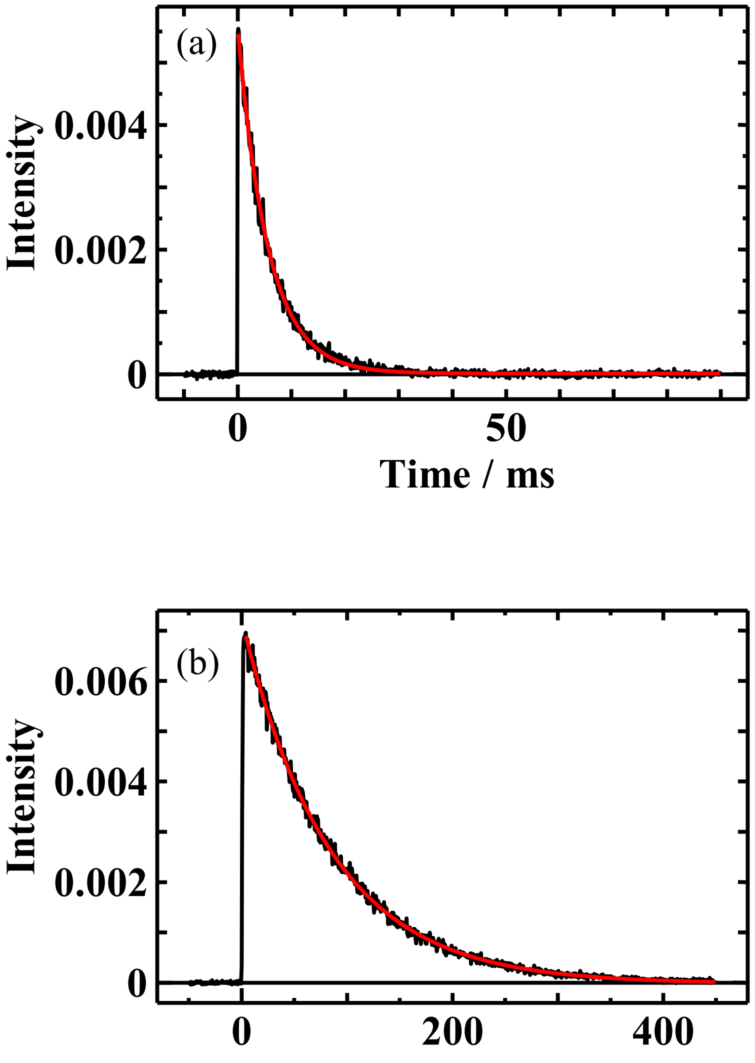

Figure 3-13. Phosphorescence decay curves of $O_2(a^1\Delta_g)$ observed in air-saturated (a) CCl_4 and (b) CH_3CN solutions of PtTFPP at 293 K (λ_{exc} = 355 nm). The experimental curves are well fitted to single exponential functions (red lines).

Table 3-3. Comparison of radiative rate constant ($k_r^{1\Delta}$) of singlet oxygen in different solvents obtained in this study with values in the literature.[a]

	$k_r^{1\Delta}$ / s^{-1}				
solvent	this work	SC	OG [b]	DAR [c]	SH [d]
CCl_4	1.6	1.17 [e]		0.91	0.041
CS_2	1.6	3.14 [e]	3.11	2.14	
C_6H_6	1.1	1.50 [f]			0.143
C_6D_6	0.90	1.335 [f]			
$PhCH_3$	0.93		1.44		0.135
PhCl	1.2		1.68		
PhBr	1.4		1.97		
PhI	1.6	2.61 [e]	2.61		
$CHCl_3$	0.69	0.96 [e]	1.13	1.14	0.088
CH_3CN	0.27		0.450		
CD_3CN	0.23				0.045
EtOH	0.32			0.55	
EtOD	0.30		0.345	0.35	0.040

[a] SC, Schmidt et al.; OG, Ogilby et al.; DAR, Darmanyan; SH, Shimizu et al.
[b] Ref [38]. [c] Ref [39]. [d] Ref [34]. [e] Ref [36]. [f] Ref [35].

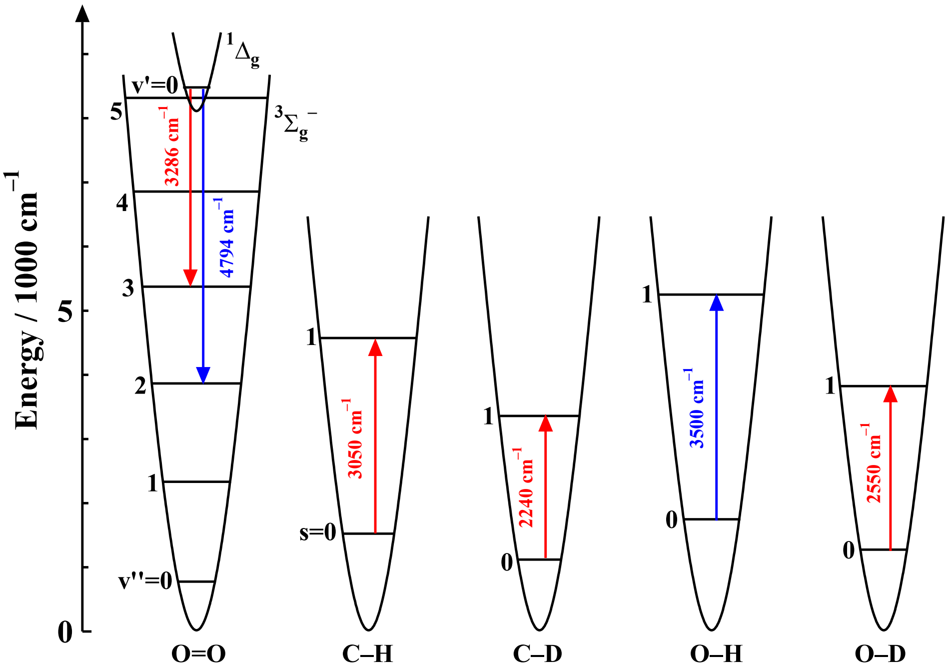

Figure 3-14. Electronic-to-vibrational energy transfer from $O_2(a^1\Delta_g)$ to X−Y bonds (X−Y = C−H, C−D, O−H, and O−D).

3-4 Conclusions

A new integrating sphere instrument was designed for measurements of absolute emission quantum yield in the spectral region between 350 and 1650 nm. To enable measurements over a wide spectral range, two photonic multichannel analyzers (MCAs) equipped with BT-CCD and InGaAs detectors were employed in this system. Both detection systems were spectrally calibrated by using standard light sources. With this instrument, the first measurements of the absolute quantum yield ($\Phi_{\mathrm{p}}^{1\Delta}$) of the $a^1\Delta_g$ ($v' = 0$) → $X^3\Sigma_g^-$ ($v'' = 0$) emission at around 1270 nm of singlet oxygen in selected solvents were performed. The obtained $\Phi_{\mathrm{p}}^{1\Delta}$ values were consistent with the literature values determined based on the relative method. Using the $\Phi_{\mathrm{p}}^{1\Delta}$ and the lifetime of $O_2(a^1\Delta_g)$ emission obtained at the same sensitizer and O_2 concentrations, the radiative ($k_{\mathrm{r}}^{1\Delta}$) and nonradiative ($k_{\mathrm{nr}}^{1\Delta}$) rate constants of $O_2(a^1\Delta_g)$ were determined in different solvents. Significant solvent effects were observed in the values of $\Phi_{\mathrm{p}}^{1\Delta}$ and $\tau_{\mathrm{p}}^{1\Delta}$. These results are attributed to the marked change in the $k_{\mathrm{nr}}^{1\Delta}$ value, which can be explained by electronic-to-vibrational energy transfer.

References

[1] Tørring, T.; Helmig, S.; Ogilby, P. R.; Gothelf, K. V. *Acc. Chem. Res.* **2014**, *47*, 1799−1806.

[2] Fischer, B. B.; Hideg, É.; Krieger-Liszkay, A. *Antioxid. Redox Signaling* **2013**, *18*, 2145−2162.

[3] Foote, C. S. *Science* **1968**, *162*, 963−970.

[4] Turro, N. J.; Ramamurthy, V.; Scaiano, J. C. *Modern Molecular Photochemistry of Organic Molecules*; University Science Books: Sausalito, CA, 2010.

[5] Lakowicz, J. R. *Principles of Fluorescence Spectroscopy*, *3rd ed.*; Springer: New York, 2006.

[6] Valuer, B. *Molecular Fluorescence*; Wiley-VCH: Weinheim, Germany, 2002.

[7] Resch-Genger, U.; Rurack, K. *Pure Appl. Chem.* **2013**, *85*, 2005−2026.

[8] Resch-Genger, U.; DeRose, P. C. *Pure Appl. Chem.* **2012**, *84*, 1815−1835.

[9] Brouwer, A. M. *Pure Appl. Chem.* **2011**, *83*, 2213−2228.

[10] Vavilov, S. I. *Z. Phys*. **1924**, *22*, 266−272.

[11] Demas, J. N.; Crosby, G. A. *J. Phys. Chem.* **1971**, *75*, 991−1024.

[12] Würth, C.; Grabolle, M.; Pauli, J.; Spieles, M.; Resch-Genger, U. *Nat. Protoc.* **2013**, *8*, 1535−1550.

[13] Würth, C.; Pauli, J.; Lochmann, C.; Spieles, M.; Resch-Genger, U. *Anal. Chem.* **2012**, *84*, 1345−1352.

[14] Würth, C.; González, M. G.; Niessner, R.; Panne, U.; Haisch, C.; Resch-Genger, U. *Talanta*, **2012**, *90*, 30−37.

[15] Würth, C.; Grabolle, M.; Pauli, J.; Spieles, M.; Resch-Genger, U. *Anal. Chem.* **2011**,

83, 3431−3439.

[16] Semonin, O. E.; Johnson, J. C.; Luther, J. M.; Midgett, A. G.; Nozik, A. J.; Beard, M. C. *J. Phys. Chem. Lett.* **2010**, *1*, 2445−2450.

[17] Kato, R.; Suzuki, K.; Furube, A.; Kotani, M.; Tokumaru, K. *J. Phys. Chem. C* **2009**, *113*, 2961−2965.

[18] Gaigalas, A. K.; Wang, L. *J. Res. Natl. Inst. Stand. Technol.* **2008**, *113*, 17−28.

[19] Porrès, L.; Holland, A.; Pålsson, L.-O.; Monkman, A. P.; Kemp, C.; Beeby, A. *J. Fluoresc.* **2006**, *16*, 267−272.

[20] Kawamura, Y.; Sasabe, H.; Adachi, C. *Jpn. J. Appl. Phys*. **2004**, *43*, 7729−7730.

[21] Suzuki, K.; Kobayashi, A.; Kaneko, S.; Takehira, K.; Yoshihara, T.; Ishida, H.; Shiina, Y.; Oishi, S.; Tobita, S. *Phys. Chem. Chem. Phys.* **2009**, *11*, 9850−9860.

[22] Ishida, H.; Tobita, S.; Hasegawa, Y.; Katoh, R.; Nozaki, K. *Coord. Chem. Rev.* **2010**, *254*, 2449−2458.

[23] Kobayashi, A.; Suzuki, K.; Yoshihara, T.; Tobita, S. *Chem. Lett.* **2010**, *39*, 282−283.

[24] Schweizer, C.; Schmidt, R. *Chem. Rev.* **2003**, *103*, 1685−1757.

[25] Schmidt, R.; Tanielian, C.; Dunsbach, R.; Wolff, C. *J. Photochem. Photobiol. A: Chem.* **1994**, *79*, 11−17.

[26] Lai, S.-W.; Hou, Y.-J.; Che, C.-M.; Pang, H.-L.; Wong, K.-Y.; Chang, C. K.; Zhu, N. *Inorg. Chem.* **2004**, *43*, 3724−3732.

[27] Wang, H.; Xing, M.; Luo, X.; Zhou, X.; Fu, Y.; Jiang, T.; Peng, Y.; Ma, Y.; Duan, X. *J. Alloys Compd.* **2014**, *587*, 344−348.

[28] Krasnovsky A. A., Jr. *Chem. Phys. Lett.* **1981**, *81*, 443−445.

[29] Losev, A. P.; Byteva, I. M.; Gurinovich, G. P. *Chem. Phys. Lett.* **1988**, *143*, 127−129.

[30] Losev, A. P.; Nichiporovich, I. N.; Byteva, I. M.; Drozdov, N. N.; Al Jghgami, I. F. *Chem. Phys. Lett.* **1991**, *181*, 45−50.

[31] Schmidt, R. *Chem. Phys. Lett.* **1988**, *151*, 369−374.

[32] Schmidt, R.; Seikel, K.; Brauer, H.-D. *J. Phys. Chem.* **1989**, *93*, 4507−4511.

[33] Shimizu, O.; Watanabe, J.; Imakubo, K.; Naito, S. *J. Phys. Soc. Jpn.* **1998**, *67*, 3664−3667.

[34] Shimizu, O.; Watanabe, J.; Imakubo, K.; Naito, S. *Chem. Lett.* **1999**, 67−68.

[35] Schmidt, R.; Afshari, E. *J. Phys. Chem.* **1990**, *94*, 4377−4378.

[36] Schmidt, R.; Shafii, F.; Hild, M. *J. Phys. Chem. A* **1999**, *103*, 2599−2605.

[37] Scurlock, R. D.; Nonell, S.; Braslavsky, S. E.; Ogilby, P. R. *J. Phys. Chem.* **1995**, *99*, 3521−3526.

[38] Poulsen, T. D.; Ogilby, P. R.; Mikkelsen, K. V. *J. Phys. Chem. A* **1998**, *102*, 9829−9832.

[39] Darmanyan, A. P. *J. Phys. Chem. A* **1998**, *102*, 9833−9837.

[40] Badger, R. M.; Wright, A. C.; Whitlock, R. F. *J. Chem. Phys.* **1965**, *43*, 4345−4350.

[41] Hidemori, T.; Akai, N.; Kawai, A.; Shibuya, K. *J. Phys. Chem. A* **2012**, *116*, 2032−2038.

[42] Hild, M.; Schmidt, R. *J. Phys. Chem. A* **1999**, *103*, 6091−6096.

[43] Minaev, B. F.; Murugan, N. A.; Ågren, H. *Int. J. Quantum Chem.* **2013**, *113*, 1847−1867.

[44] Minaev, B. F.; Minaev, V. A.; Evtuhov, Y. V. *Int. J. Quantum Chem.* **2009**, *109*, 500−515.

[45] Schmidt, R.; Afshari, E. *Ber. Bunsen-Ges. Phys. Chem.* **1992**, *96*, 788−794.

[46] Merkel, P. B.; Kearns, D. R. *J. Am. Chem. Soc.* **1972**, *94*, 7244−7253.

[47] Hurst, J. R.; Schuster, G. B. *J. Am. Chem. Soc.* **1983**, *105*, 5756−5760.

Appendix 3-1 Results of the Measurements in Different Solvents Based on Absolute Method

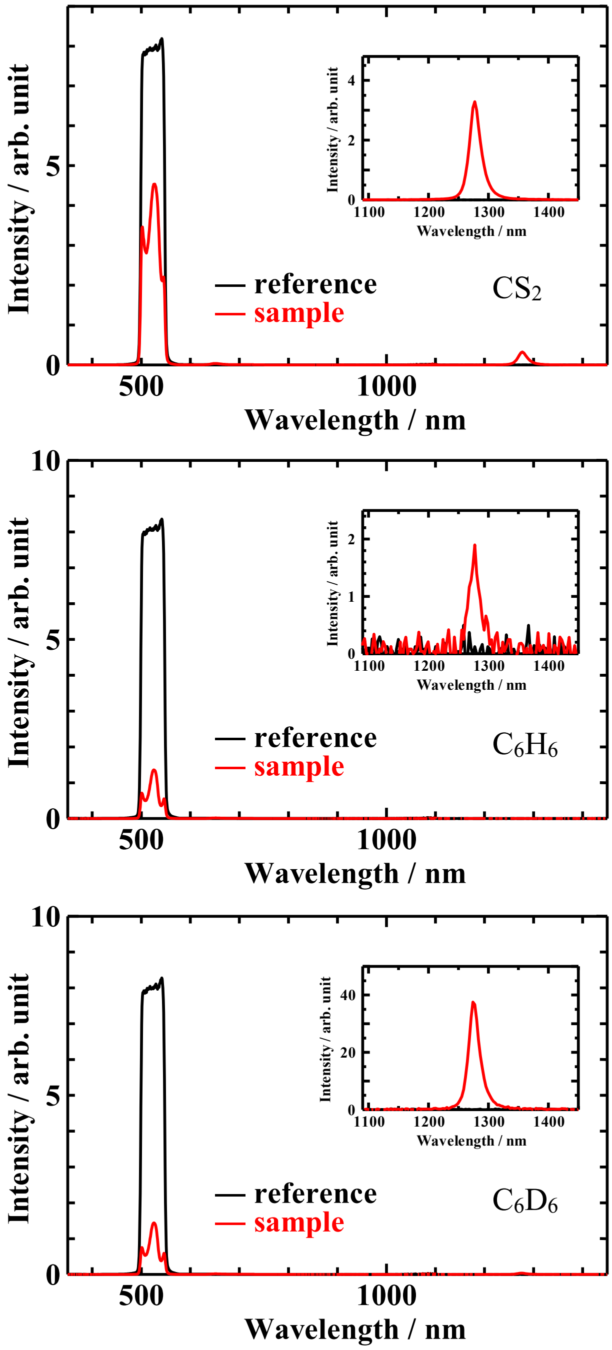

Figure S3-1. Excitation light profiles and emission spectra with (red line) and without (black line) PtTFPP in CS_2, C_6H_6, and C_6D_6 solutions obtained using the instrument shown in Figure 3-2. Exposure times in the emission spectral measurements were set to 1 s for CS_2, 5 s for C_6H_6 and C_6D_6, respectively.

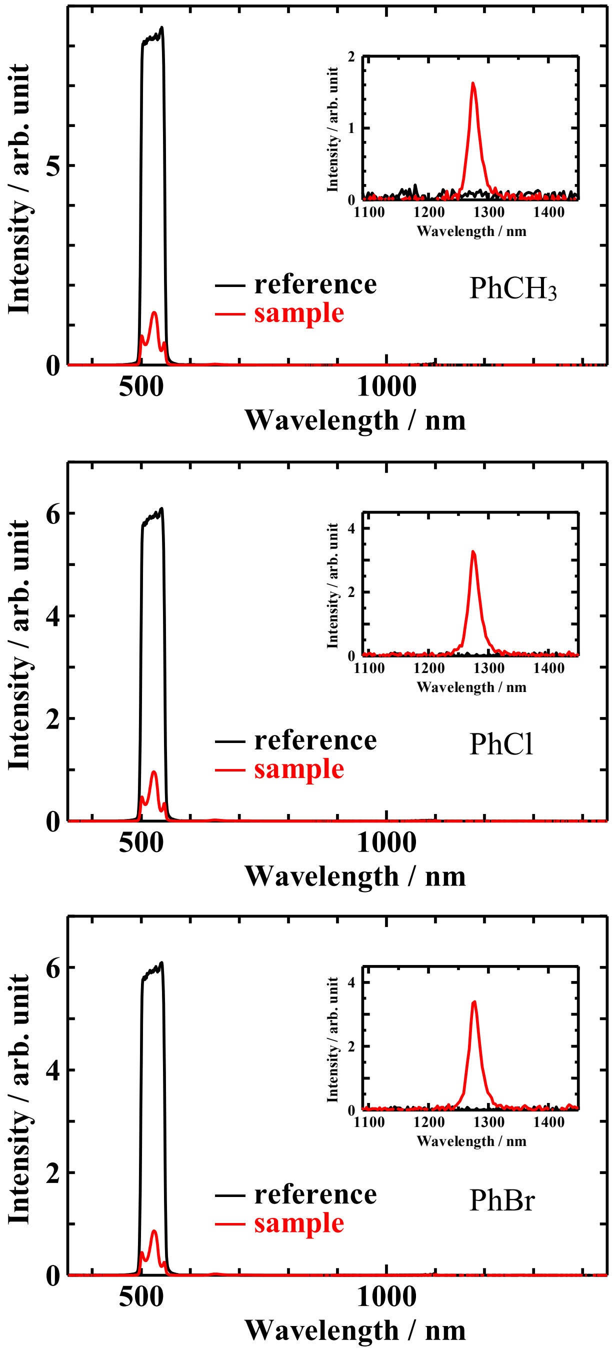

Figure S3-2. Excitation light profiles and emission spectra with (red line) and without (black line) PtTFPP in PhCH$_3$, PhCl, and PhBr solutions obtained using the instrument shown in Figure 3-2. Exposure times in the emission spectral measurements were set to 5 s for PhCH$_3$, PhCl, and PhBr, respectively.

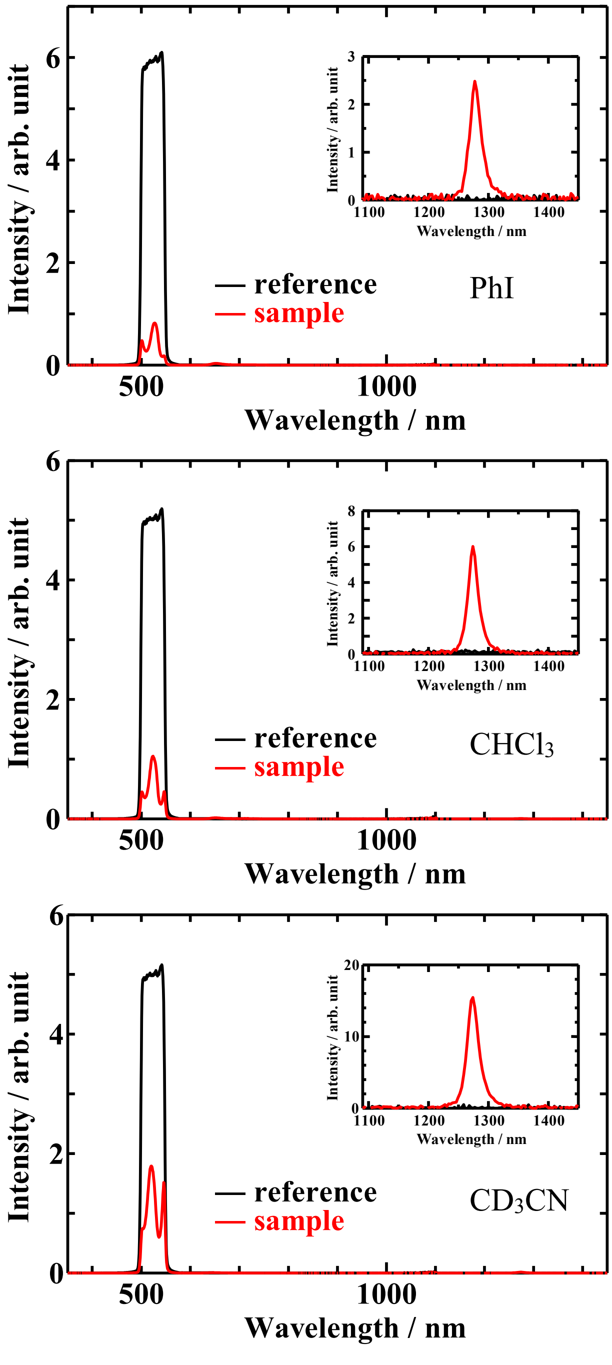

Figure S3-3. Excitation light profiles and emission spectra with (red line) and without (black line) PtTFPP in PhI, $CHCl_3$, and CD_3CN solutions obtained using the instrument shown in Figure 3-2. Exposure times in the emission spectral measurements were set to 5 s for PhI, $CHCl_3$, and CD_3CN, respectively.

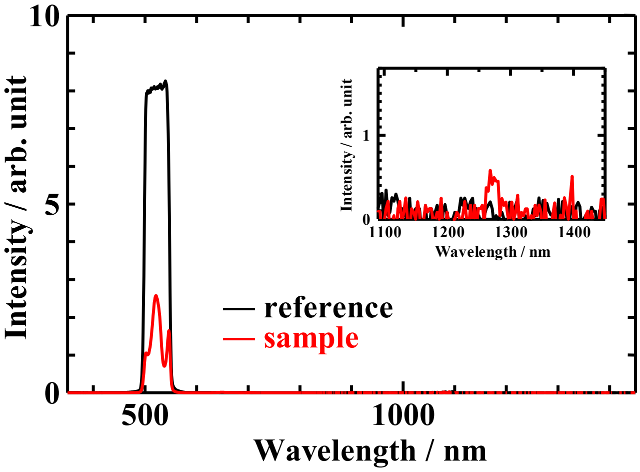

Figure S3-4. Excitation light profiles and emission spectra with (red line) and without (black line) PtTFPP in EtOD solution obtained using the instrument shown in Figure 3-2. Exposure times in the emission spectral measurements were set to 5 s for EtOD.

Appendix 3-2 Results of the Measurements in Different Solvents Based on Relative Method

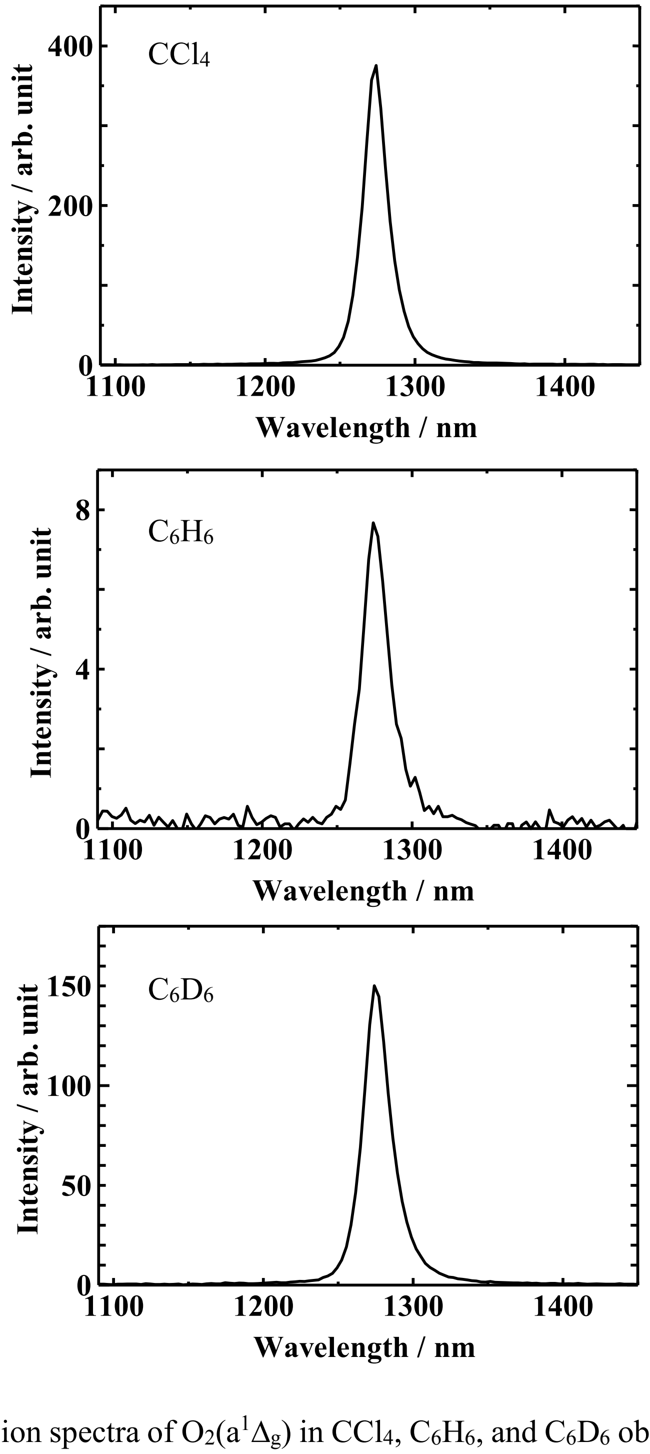

Figure S3-5. Emission spectra of $O_2(a^1\Delta_g)$ in CCl_4, C_6H_6, and C_6D_6 obtained by using the instrument in Figure 3-3. Exposure times were set to 1 s for CCl_4, for 6 s C_6H_6, and C_6D_6, respectively.

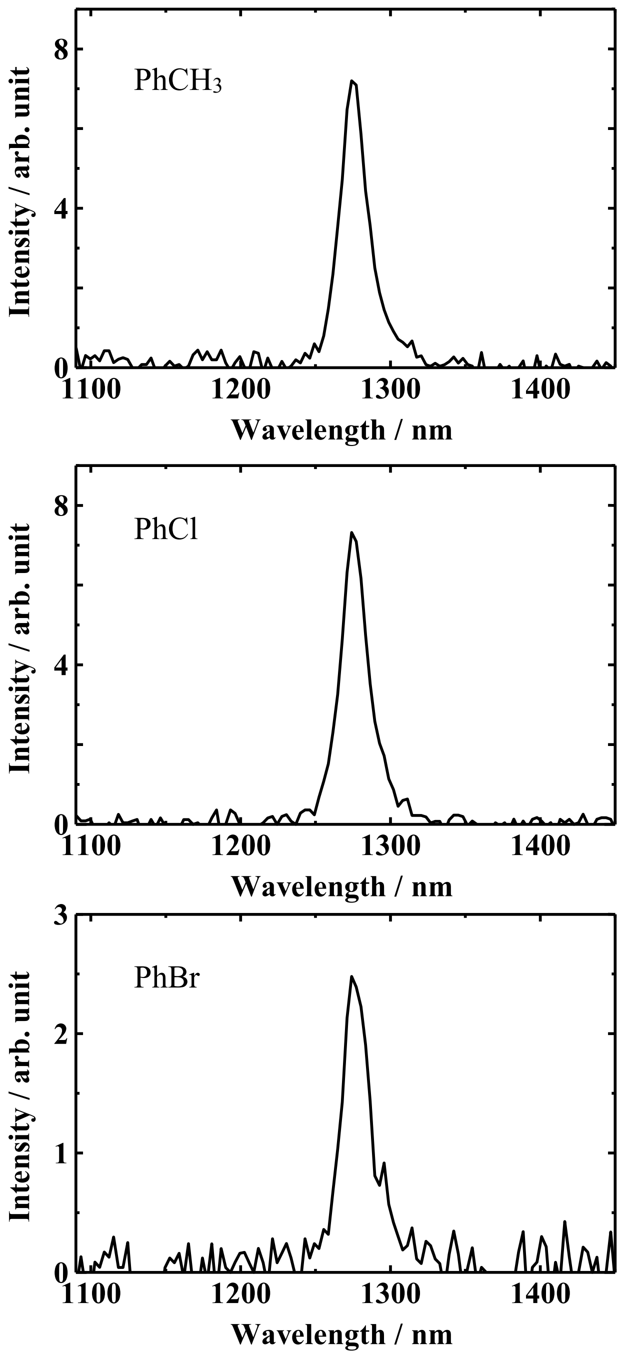

Figure S3-6. Emission spectra of $O_2(a^1\Delta_g)$ in $PhCH_3$, PhCl, and PhBr obtained by using the instrument in Figure 3-3. Exposure times were set to 6 s for $PhCH_3$, 3 s for PhCl, and 1 s for PhBr, respectively.

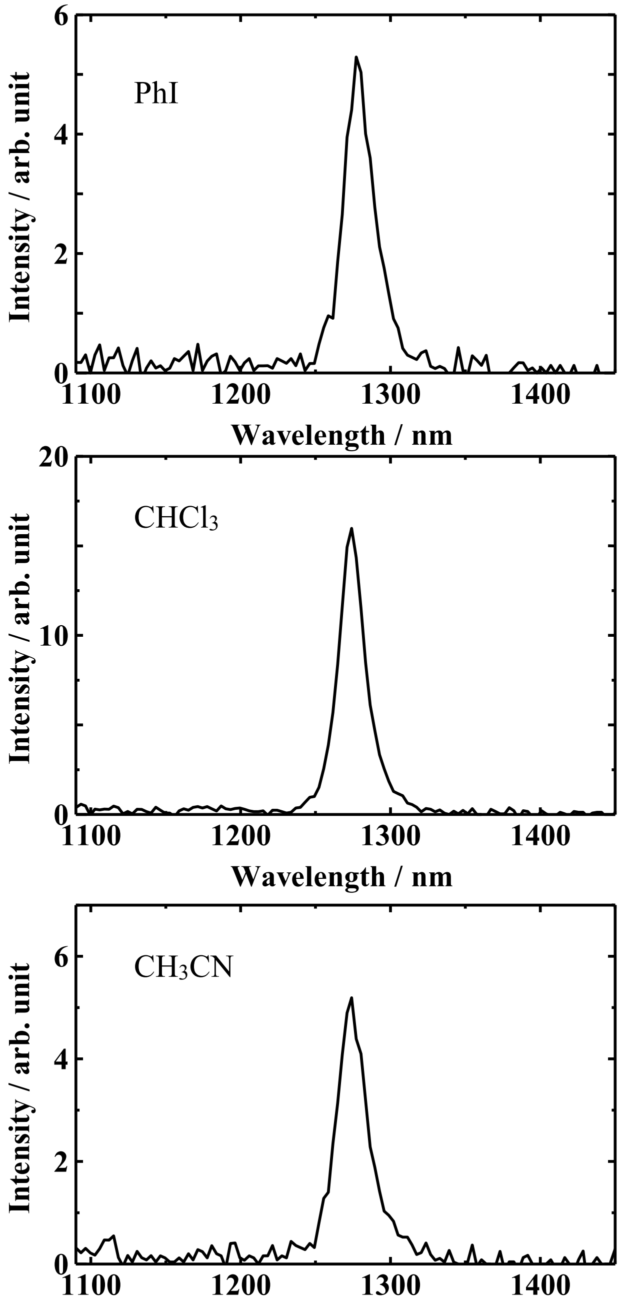

Figure S3-7. Emission spectra of $O_2(a^1\Delta_g)$ in PhI, $CHCl_3$, and CH_3CN obtained by using the instrument in Figure 3-3. Exposure times were set to 3 s for PhI and $CHCl_3$, and 6 s for CH_3CN, respectively.

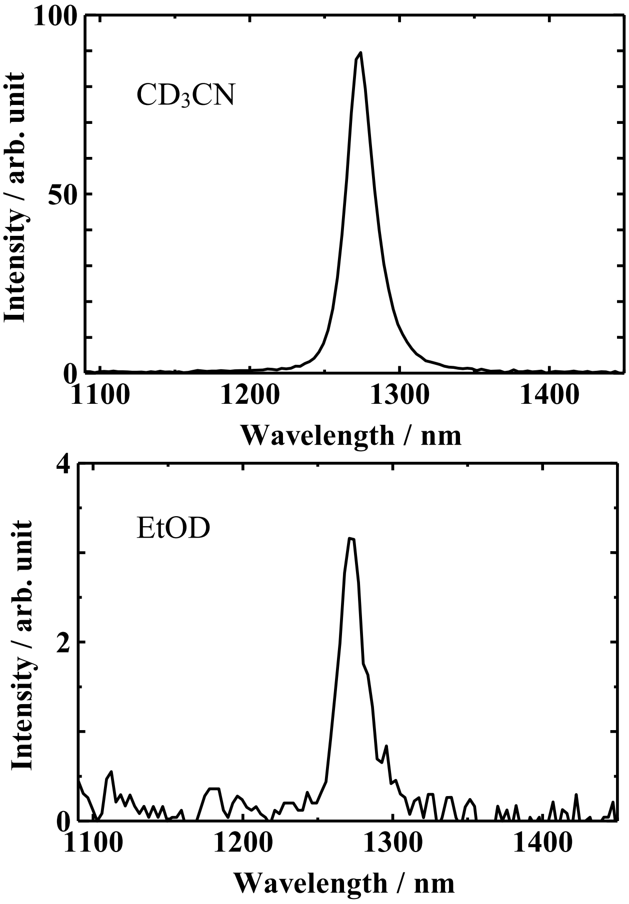

Figure S3-8. Emission spectra of $O_2(a^1\Delta_g)$ in CD_3CN and EtOD obtained by using the instrument in Figure 3-3. Exposure times were set to 6 s for CD_3CN, and 8 s (averaging 10 times) for EtOD, respectively.

Appendix 3-3 The Decay Curves of Singlet Oxygen in Different Solvents

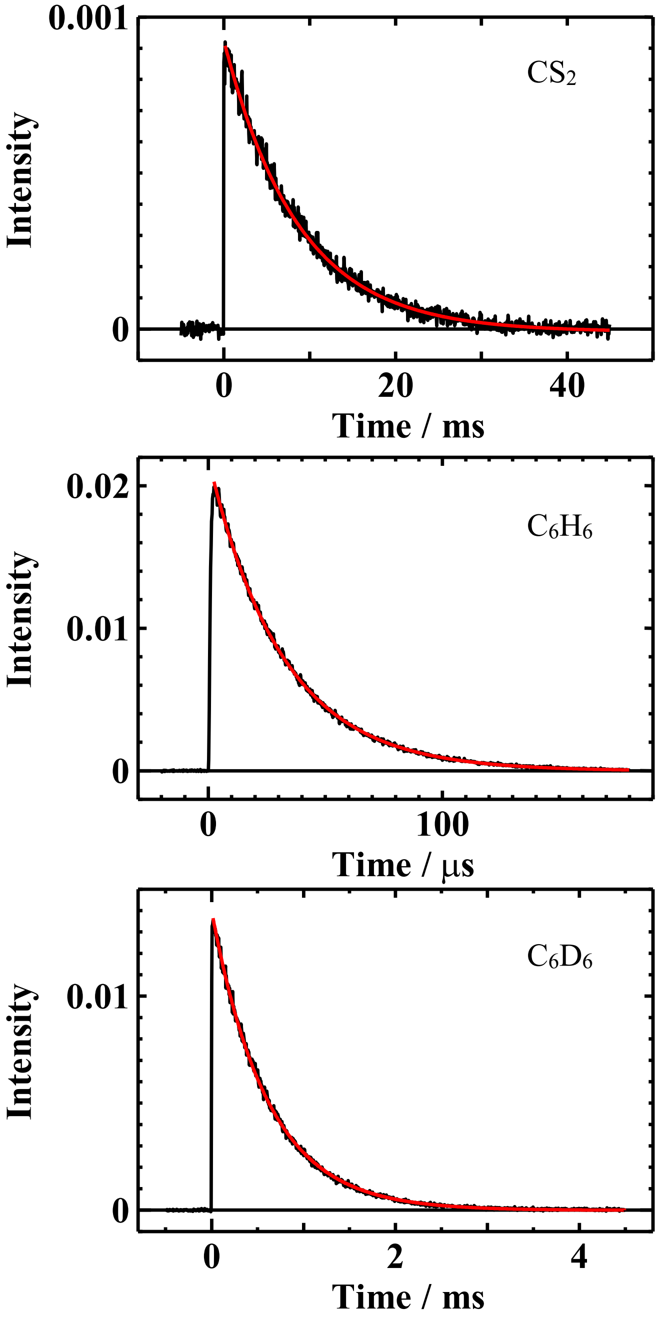

Figure S3-9. Phosphorescence decay curves of $O_2(a^1\Delta_g)$ observed in air-saturated CS_2 (λ_{exc} = 532 nm), C_6H_6, and C_6D_6 (λ_{exc} = 355 nm) solutions of PtTFPP at 293 K. The experimental curves are well fitted to single exponential functions (red lines).

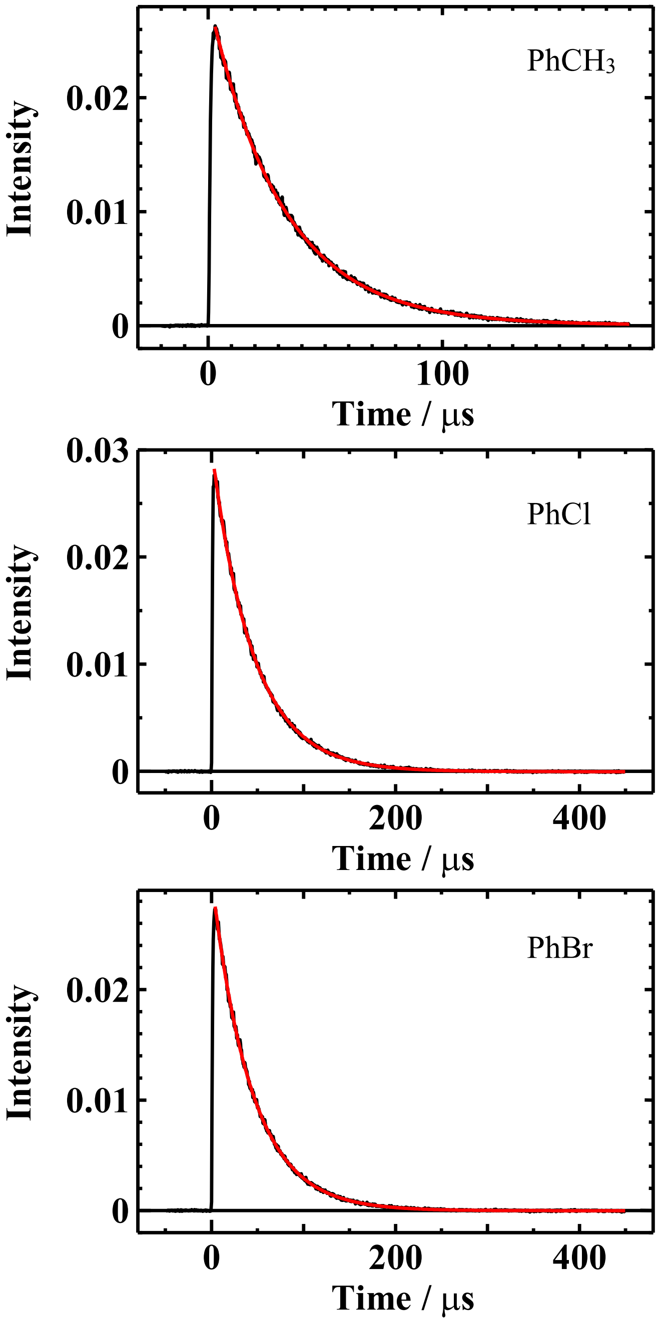

Figure S3-10. Phosphorescence decay curves of $O_2(a^1\Delta_g)$ observed in air-saturated $PhCH_3$ (λ_{exc} = 355 nm), PhCl, and PhBr (λ_{exc} = 532 nm) solutions of PtTFPP at 293 K. The experimental curves are well fitted to single exponential functions (red lines).

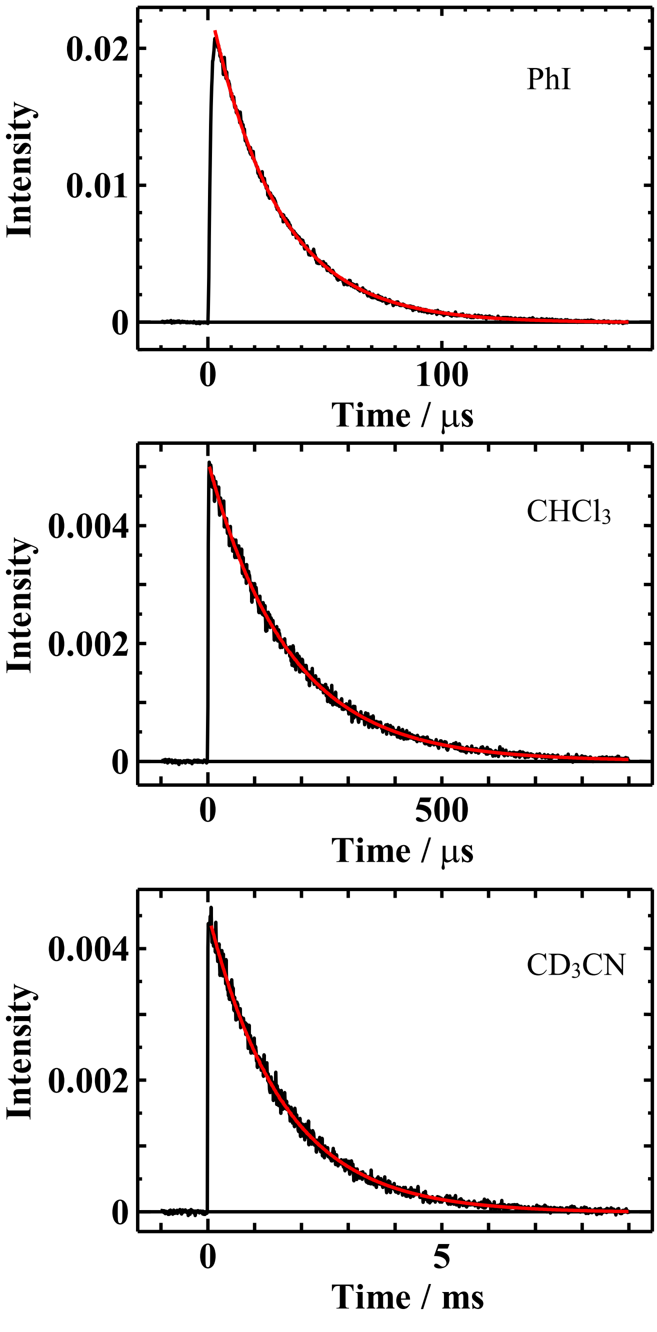

Figure S3-11. Phosphorescence decay curves of $O_2(a^1\Delta_g)$ observed in air-saturated PhI (λ_{exc} = 532 nm), $CHCl_3$, and CD_3CN (λ_{exc} = 355 nm) solutions of PtTFPP at 293 K. The experimental curves are well fitted to single exponential functions (red lines).

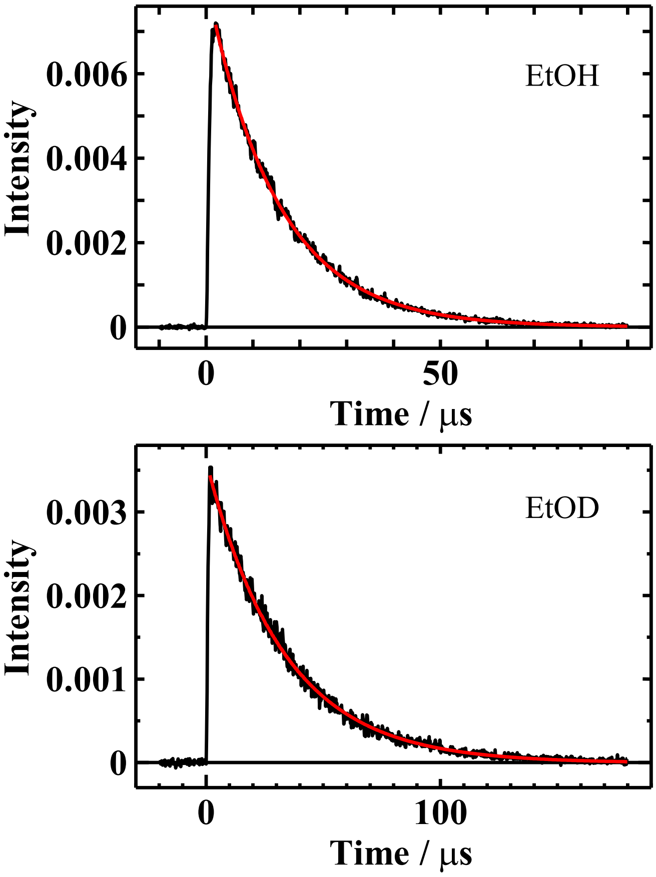

Figure S3-12. Phosphorescence decay curves of $O_2(a^1\Delta_g)$ observed in air-saturated EtOH and EtOD (λ_{exc} = 355 nm) solutions of PtTFPP at 293 K. The experimental curves are well fitted to single exponential functions (red lines).

Chapter 4

Summary

In this thesis, the phosphorescence quenching mechanisms of neutral and cationic Ir(III) complexes by molecular oxygen were investigated, and the formation efficiency and the relaxation properties of singlet oxygen produced by phosphorescence quenching of transition metal complexes were revealed.

In Chapter 2, the phosphorescence quenching of neutral and cationic iridium(III) complexes by molecular oxygen and aromatic electron acceptors (AEAs; 1,4-dinitrobenzene (DNB), nitrobenzene (NB), and 1,4-dicyanobenzen (DCB)) was investigated in CH_3CN. The phosphorescence quenching rate constant (k_q) by AEAs increased with decreasing Gibbs energy change (ΔG_{el}) of electron transfer and gave a diffusion-controlled rate constant (k_d) of 2.0×10^{10} $M^{-1}s^{-1}$. The radical ions produced by electron-transfer reactions between excited triplet Ir(III) complexes and AEAs were confirmed by performing the transient absorption measurement, although the separated ion yields were as low as 0.10−0.17. It was revealed that two competing pathways (noncharge-transfer (nCT) and charge-transfer (CT) channels) are involved in the phosphorescence quenching of iridium(III) complexes by molecular oxygen. For the Ir(III) complex/O_2 systems with $\Delta G_{el} \lesssim -0.8$ eV, the limiting k_q value was over $(4/9)k_d$ ($k_d = 4.1 \times 10^{10}$ $M^{-1}s^{-1}$ for Ir(III) complex/O_2 system) and the efficiencies (f_Δ) of $^1O_2$ production from triplet states quenched by oxygen were larger than 0.25 ($f_\Delta = 0.40$). These results suggested the involvement of $^1O_2$ formation through intersystem crossing between singlet, triplet, and quintet CT complexes.

In Chapter 3, a new integrating sphere instrument equipped with a Xe light source and two spectrally calibrated photonic multichannel analyzers using a back-thinned charge-coupled device (BT-CCD) and InGaAs detectors was developed for the measurements of absolute emission quantum yield from the visible to near-infrared region ($\lambda = 350{-}1650$ nm). Using this instrument and platinum(II) meso-tetra(pentafluorophenyl)porphine (PtTFPP) as a photosensitizer, the absolute quantum yield ($\Phi_{\mathrm{p}}^{^1\Delta}$) of the $a^1\Delta_g$ ($v' = 0$) → $X^3\Sigma_g^-$ ($v'' = 0$) emission from singlet oxygen which has emission peak at about 1270 nm in various solvents was measured. The $\Phi_{\mathrm{p}}^{^1\Delta}$ values in CCl_4 and CS_2 under infinite dilution of PtTFPP were evaluated to be 2.2×10^{-2} and 6.4×10^{-2}, respectively. In addition, the relative quantum yields in the other solvents were determined using the absolute $\Phi_{\mathrm{p}}^{^1\Delta}$ value in CCl_4. From the $\Phi_{\mathrm{p}}^{^1\Delta}$ values and lifetimes of $O_2(a^1\Delta_g)$, the radiative and nonradiative rate constants ($k_{\mathrm{r}}^{^1\Delta}$ and $k_{\mathrm{nr}}^{^1\Delta}$) of $O_2(a^1\Delta_g)$ were determined. The obtained $\Phi_{\mathrm{p}}^{^1\Delta}$ and $k_{\mathrm{r}}^{^1\Delta}$ values were compared with the literature values determined by the relative method.

The measurements in Chapters 2 and 3 were performed for homogeneous systems using organic solvents. However, intracellular environments are inhomogeneous and more complex. Therefore, as future works, it is necessary to clarify the interactions of the excited triplet Ir(III) complexes with molecular oxygen and the photophysical properties of singlet oxygen under the conditions analogous to the intracellular environment. For example, $(btp)_2Ir(acac)$ which is one of the Ir(III) complexes used in this study is known to be localized into the membrane of endoplasmic reticulum in cells. Hence, it will be important to measure the k_{q} value of oxygen quenching and the quantum yield of singlet oxygen formation in membrane such as *L*-α-dimyristoylphosphatidylcholine (DMPC). In addition, it is required to examine the interactions between Ir(III) complexes in the excited triplet state and endogenous substances such as riboflavin and ubiquinone-10 in solution and membrane. For the photophysical properties of singlet oxygen, it is desired to reveal the deactivation rate constants in membranes by measuring the emission quantum yield and lifetime. Furthermore, more detailed knowledges for the interactions between the excited triplet Ir(III) complexes and molecular oxygen and the photophysical properties of singlet oxygen will be obtained by performing similar measurements in living cells.